EXPERIMENTAL STUDIES OF PARTICLE ASSEMBLY INTO STREAMWISE BANDS

A Dissertation
Presented to
The Academic Faculty

by

Andrew J. Yee

In Partial Fulfillment
of the Requirements for the Degree
Doctor of Philosophy in the
George W. Woodruff School of Mechanical Engineering

Georgia Institute of Technology
December 2021

EXPERIMENTAL STUDIES OF PARTICLE ASSEMBLY INTO STREAMWISE BANDS

Approved by:

Dr. Minami Yoda
School of Mechanical Engineering
Georgia Institute of Technology

Dr. Sven Behrens
School of Chemical and Biomolecular Engineering
Georgia Institute of Technology

Dr. Alexander Alexeev
School of Mechanical Engineering
Georgia Institute of Technology

Dr. Shaurya Prakash
Department of Mechanical and Aerospace Engineering
The Ohio State University

Dr. Todd Sulchek
School of Mechanical Engineering
Georgia Institute of Technology

Date Approved: August 12, 2021

TABLE OF CONTENTS

ACKNOWLEDGEMENTS ……...……v
LIST OF TABLES ……..……...…….……vii
LIST OF FIGURES ……...…….…….…..…….……viii
LIST OF SYMBOLS AND ABBREVIATIONS ……..……x
SUMMARY …….…….……..…….……xv
CHAPTER 1: INTRODUCTION……..……...……..…….…….……..1
1.1 Introduction to Colloidal Self-Assembly……...…..……...2
1.2 Fundamental Mechanics behind Colloidal Self-Assembly……5
1.3 Bands and Band Formation…..……..6
1.4 Thesis Objectives……...9
1.5 Summary of Thesis Chapters…….……..11

CHAPTER 2: LITERATURE REVIEW AND BACKGROUND INFORMATION 12
2.1 Description of Electric Double Layer…….……13
2.2 Wall-Normal Forces…….……15
2.2.1 Lift Forces in Shear Flow …….……16
2.2.2 Lift Forces in DC Electric Fields……...…..21
2.2.3 Lift Forces in Combined EO and Shear Flow…….…..24
2.3 Buoyancy and Drag Force ……...……25
2.4 DLVO Theory……..……26
2.5 Near-Wall Streamwise Fluid and Particle Velocity……...…..28
2.6 Particle Assemblies……..33
2.7 Mechanisms Behind Particle/Chain Assembly……35

CHAPTER 3: EXPERIMENTAL SETUP AND PROCEDURE..……37
3.1 The Microchannel ……...37
3.2 Experimental Solutions ……...44
3.3 Generating Poiseuille and Electroosmotic Flow ……44
3.4 Visualizing Particles or Bands in Counterflow ……...45
3.5 Experimental Procedures ……...…….…49

CHAPTER 4: IMAGE PROCESSING……..56
4.1 Band Formation Overview……...…56
4.2 Band Detection…….58
4.3 Threshold Electric Field Magnitude …….……...60
4.4 Time for the First Band to Form …….……..…62
4.5 Steady-State Number of Bands……64
4.6 An Alternative Timescale Based Upon the Image Grayscales ……64
4.7 Particle Count in the Accumulation Stage……...…67
4.8 Particle Positions…….…68
4.9 Particle Tracking and Particle Velocities…….71

CHAPTER 5: HOMOGENEOUS PARTICLE SOLUTION RESULTS……73
5.1 Banding Maps……74
5.2 Partial Bands……78
5.3 Timescales for Band Formation……79
5.4 Number of Bands……85

CHAPTER 6: TWO-COLOR EXPERIMENTS……89
6.1 Particle Growth Rate during Accumulation ……91
6.2 Comparison with Lift Force Predictions: Assumptions……99
6.3 Comparison with Lift Force Predictions: Model ……107
6.4 Particle Velocities in the Streamwise (x) Direction……114
6.5 Particle Cross-stream Velocities during Band Formation ……126

CHAPTER 7: CONCLUSIONS AND RECOMMENDATIONS……129
7.1 Thesis Summary……129
7.2 Conclusions……131
7.3 Contributions ……134
7.4 Potential Applications……136
7.5 Recommendations for Future Work……137

APPENDIX A: MISCELLANEOUS EXPERIMENTAL PROCEDURES……140
APPENDIX B: UNCERTAINTY ANALYSIS……148
APPENDIX C: COMPARISON BETWEEN TIMESCALES BASED ON BAND FORMATION OR GRAYSCALE STANDARD DEVIATION ……154
APPENDIX D: ELECTRIC FIELD VS. ELECTRIC FIELD OFFSET ……156
APPENDIX E: HETEROGENEOUS RESULTS ……158
APPENDIX F: PARTICLE COUNTS AT DIFFERENT CHANNEL LOCATIONS…162
APPENDIX G: ESTIMATE OF THE EFFECT OF JOULE HEATING……167
REFERENCES ……169

ACKNOWLEDGEMENTS

I must sincerely thank many people who have supported me during the writing of this thesis, which would not have been possible without their support and guidance. My advisor, Dr. Minami Yoda, has supported my research for many years and my most heartfelt gratitude goes to her for her invaluable guidance, contacts, resources, and advice. I would also like to thank my committee members: Dr. Alexander Alexeev, Dr. Todd Sulchek, Dr. Shaurya Prakash, and Dr. Sven Behrens for their time and effort when reviewing this work and for their advice when improving upon it.

I would also like to thank various collaborators who have helped to further my understanding of band formation. The work by Dr. Shaurya Prakash and Dr. Varun Lochab from The Ohio State University on the band cross-section during banding was enlightening, and our discussions helped to further my understanding of band formation immensely. Dr. Yoshiyuki Tagawa and Dr. Hajime Onuki from the Tokyo University of Agriculture and Technology and our collaboration on alternative banding timescale analysis for the stages of band formation also encouraged me to think about significant band characteristics and what fundamental mechanics may cause them.

I am also grateful to those who have worked alongside me, encouraging me and helping me during my research and the development of this thesis. Necmettin Cevheri was the predecessor to my work on banding and helped me get adjusted to the original experimental system and MATLAB code. Yaofa Li, Tongran Qin, Shekeib Musa, Michael Spadaro, Michael Lanahan, Daniel Lee, and many others have supported me with advice and assistance as well.

Lastly, I would like to thank my family for their emotional support. My parents, Timothy and Lisa Yee, raised me to be inquisitive and to persevere against adversity. My brother and sister, Brandon Yee and Christine Yee, gave me invaluable emotional support as well as my grandpa, grandma, and uncle, Daniel Yee, Elizabeth Yee, and Michael Yee.

LIST OF TABLES

Table 3.1 List of Particle Solutions……42
Table 3.2 List of Excitation Filters ……..……49
Table 5.1 List of Colloidal Particle Suspensions……..……75
Table 6.1 Values of *c* for the Exponential Fit with Constant…….……97
Table 6.2 Values of *c* for the Exponential Fit without Constant……97
Table 6.3 Expected Near-wall Particle Fraction for the Exponential Fit…….111
Table E.1 Vendor Solutions for Heterogeneous Solutions……...158
Table E.2 Experimental Solutions for Heterogeneous Solutions …….158

LIST OF FIGURES

Figure 1.1 Evanescent-wave visualizations of suspended fluorescent polystyrene particles……...…8
Figure 3.1 Microchannel overview ……...……..37
Figure 3.2 Overall tubing setup……..……44
Figure 3.3 Overall illumination setup …….……48
Figure 3.4 Cross-section of the microchannel showing fluorescent particles illuminated by evanescent waves ……..……..48
Figure 4.1 Three grayscale images during band formation…….……57
Figure 4.2 Three typical intensity profiles during band formation ……59
Figure 4.3 Sample banding maps ……..……..61
Figure 4.4 Number of bands over time …….……..63
Figure 4.5 The evolution of the normalized image grayscale average and the normalized image grayscale standard deviation ……..66
Figure 4.6 Signal to noise ratio vs. mean grayscale ……70
Figure 5.1 Banding maps for various parameters ……..……76
Figure 5.2 Banding map for Solution 2 in the *E*-*x* parameter space …….…..78
Figure 5.3 Semi-log plot of band formation time vs offset electric field for different shear rates……80
Figure 5.4 Normalized band formation time vs normalized offset electric field for different shear rates/particle fractions……81
Figure 5.5 Normalized band formation time vs normalized offset electric field for different zeta potential/shear rate..……..……84
Figure 5.6 Normalized band formation time vs normalized offset electric field for different particle radius/shear rate..……..…..…84
Figure 5.7 Alternate banding timescale for different streamwise position …...……..85
Figure 5.8 Band spatial cross-stream period vs normalized offset electric field for different shear rate/volume fraction ……..…86
Figure 5.9 Band spatial cross-stream period vs normalized offset electric field for different shear rate/particle radius ……..……...87
Figure 5.10 Number of bands vs near-wall shear rate for different particle radius/offset electric field ……..……....88
Figure 6.1 Number of near-wall tracer particles vs time for different trials during accumulation ……..……..93
Figure 6.2 Average grayscale as a function of time ……..……..94
Figure 6.3 Near-wall tracer particles vs normalized time for different electric field……...……..95
Figure 6.4 Near-wall tracer particles vs normalized time for different near-wall shear rate……...…96
Figure 6.5 Near-wall tracer particles vs normalized time for different electric field using different threshold grayscale ……99
Figure 6.6 Expected near-wall particle fraction vs time …….……..111
Figure 6.7 Expected flow and particle velocities vs particle-wall distance ……..115

Figure 6.8 Histogram of near-wall particle velocities during the accumulation phase for different electric field ……....118
Figure 6.9 Histogram of near-wall particle velocities during the steady-state phase for different electric field ……..……..120
Figure 6.10 Comparison between histogram of near-wall particle velocities between bands during steady-state and early accumulation for varying electric field ……..122
Figure 6.11 Peak histogram velocities at steady-state within bands vs electric field ……...123
Figure 6.12 Histogram of near-wall particle velocities during the steady-state phase inside bands for different near-wall shear rate……...124
Figure 6.13 Near-wall particle velocities within bands during steady-state vs particle brightness ……....126
Figure 6.14 Histogram of near-wall cross-stream particle velocities around a band shortly before band formation……..127
Figure B.1 Image of the stage micrometer……149
Figure B.2 Combination of individual images into a combined image ……150
Figure B.3 Combined image of channel ……151
Figure B.4 Sketch of channel path dimensions……..151
Figure B.5 Bottom view of TIR spots illuminated at λ = 488 nm ……152
Figure B.6 Side view of reflections ……...152
Figure C.1 T_o vs T_I ……154
Figure D.1 N_s^{-1} vs. E or $E–E_{min}$ for various φ_∞ ……...……...……156
Figure E.1 Heterogeneous results for E_{min} ……159
Figure E.2 Heterogeneous results for T_o……161
Figure F.1 Near-wall particle number concentration over different positions ……..163
Figure F.2 Near-wall particle velocities along the streamwise direction during the steady-state phase……164
Figure F.3 Near-wall particle concentration over different positions at steady-state ……165
Figure F.4 Averaged particle area concentrations divided by penetration depth …..166
Figure G.1 Linear relationship during wall zeta potential measurement ……...168

LIST OF SYMBOLS AND ABBREVIATIONS

SYMBOLS

General symbols

ζ	Zeta potential (generic)
$\forbidden{V}$	Volume
δ	Inter-particle spacing (center to center)
λ	Wavelength
c	Molar concentration (generic)
F	Force
φ	Volume fraction

Coordinate system-related symbols

x	Streamwise direction, 0 at inlet to long, straight section of channel path and increases downstream
y	Cross-stream direction, perpendicular to streamwise and wall-normal directions, 0 at stream central axis and the positive direction follows the right hand rule
z	Wall-normal direction, 0 at bottom channel wall and increases further into the channel

Particle-related symbols

a	Particle radius
ζ_P	Particle zeta potential
ρ_P	Particle density
$\forbidden{V}_p$	Particle volume
N'_T	Number of near-wall tracer particles (single trials)
N_T	Number of near-wall tracer particles (average of single trials)
δ_∞	Average interparticle spacing in the experimental solution (center to center)
δ_w	Average interparticle spacing in the illuminated region (center to center)
δ_b	Average interparticle spacing in the illuminated region within the bands (center to center)
δ_n	Average interparticle spacing in the illuminated region between the bands (center to center)

Particle position/velocity-related symbols:

h	Smallest distance between the particle surface and the closest channel wall
U'_p	Experimental particle streamwise velocity (individual)
U_p	Experimental particle streamwise velocity (list of U'_p over a given time or set of image pairs)

U_p^M	Peak value of U_p when expressed as histogram
U_p^X	Expected particle streamwise velocity in bulk of channel
U_p^{XW}	Expected particle streamwise near-wall velocity
z_C	Boundary in z that is closer to the channel wall for the determination of U_p^{XW}
z_F	Boundary in z that is farther from the channel wall for the determination of U_p^{XW}
U_{po}	Expected streamwise component of Poiseuille flow on flow/particle velocity
U_{eo}	Expected streamwise component of electroosmotic flow on flow/particle velocity
U_{ep}	Expected streamwise component of electrophoresis on particle velocity
G_w	Correction factor to expected near-wall shear flow velocity as described by Goldman (1963)
Z_r	Reduction factor of electrophoretic mobility
U_s	Particle streamwise velocity relative to the fluid
V_y	Particle cross-stream velocity
Ω	Particle angular velocity in the cross-stream direction
D_C	Distance between the particle center and the closest channel wall, often z
D_F	Distance between the particle center and the farthest channel wall

Particle force-related symbols:

F_L	Modeled wall-normal lift force during the accumulation stage based on the results of Choudhary *et al*. (2019; 2021) and Khair and Kabarowski (2020)
D_z	Drag force on particle, specifically in the wall-normal direction

Solution-related symbols

n_2	Index of refraction for water
$\forall_\infty$	Volume of the experimental solution
φ_∞	Particle volume fraction in the experimental solution
φ_w	Particle volume fraction in the illuminated region
μ	Experimental solution dynamic viscosity
ν	Experimental solution kinematic viscosity
ρ_s	Experimental solution density
ε	Experimental solution electric permittivity
ε_r	Experimental solution dielectric constant
ε_0	Vacuum electric permittivity
c_S	Molar concentration of dissolved sodium tetraborate decahydrate in th experimental solution
T	Experimental solution temperature
$\forall_b$	Volume of concentrated 2% φ particle solution required to generate experimental solution
c_{pw}	Specific heat capacity of the solution

Flow field-related symbols

ΔP	Pressure difference between the inlet and outlet of the microchannel
ΔV	Voltage difference between the inlet and outlet of the microchannel
E	Applied streamwise voltage gradient
$\dot{\gamma}_w$	Average shear rate in the illuminated region

Channel-related symbols

H	Depth of channel
W	Average width of channel
L	Length of channel from reservoir to reservoir
L_S	Length of straight portion of channel
W_t	Width of the top of the etched open channel
W_b	Width of the top of bottom of the etched open channel
A_c	Area of channel cross-section
P_c	Perimeter of channel cross-section
D_h	Channel hydraulic diameter
$\forall_\infty$	Volume of solution inside the channel
ζ_w	Channel wall zeta-potential
n_1	Index of refraction for fused silica

Illumination-related symbols

I_L	Illumination intensity as measured from laser head
I	Evanescent wave illumination intensity
I_0	Evanescent wave illumination at the interface
t_P	Duration of illumination pulse
t_S	Time between consecutive, paired pulses (from middle of both pulse durations)
θ_i	Angle of incidence for evanescent wave illumination
z_p	Evanescent wave illumination penetration depth
D_V	Wall-parallel distance between two adjacent TIRF reflections on the "top" surface of the fused silica "lid" of the microchannel
D_H	Wall-normal distance between consecutive reflections of the TIRF reflection on the "top" surface of the microchannel and the "bottom" surface of the microchannel

Image-related symbols

M	Objective magnification
NA	Numerical aperture of objective
B	Pixel grayscale
I_o	Average particle grayscale intensity of an image
I_b	Average background grayscale intensity of an image
σ_o	Standard deviation of the particle grayscale intensity of an image
σ_b	Standard deviation of the background grayscale intensity of an image
A_p	Particle area brightness
A_{p0}	Estimated particle area brightness at the wall, $z = 0$
G	Average image grayscale

σ_G	Image grayscale standard deviation
$\bar{G}$	G normalized by its maximum value
$\bar{\sigma}_G$	σ_G normalized by its maximum value
κ_G	Curvature of $\bar{\sigma}_G$
$\bar{I}(y)$	Row-averaged grayscale intensity

Band-related symbols

E_{min}	Minimum E required for bands to form under constant near-wall shear rate
ΔE	Difference between E and E_{min}
x_c	Value of x where bands begin to form and propagate downstream
T_o	Time for bands for form; end of accumulation stage
T_I	Alternative timescale for the end of accumulation stage
T_{SS}	Timescale for the start of the steady-state stage
N_s	Steady-state number of bands
E_L	Lower E candidate for determining E_{min}
E_H	Higher E candidate for determining E_{min}
N_L	N_s at E_L
N_H	N_s at E_H

Chemical, ion-related symbols

K_D	Disassociation constant
K_σ	Surface conductivity
K_L	Bulk conductivity
Z	Charge number

Constants

k_B	Boltzmann constant
π	Ratio of a circle's circumference to its diameter
e	Euler's number
N_A	Avogadro's number
q_e	elementary charge
g	magnitude of gravitational acceleration
A	Hamaker constant

Dimensionless numbers

Re	Reynolds number
St	Strouhal number
Du	Dukhin number

ABBREVIATIONS

PS	Polystyrene
EOF	Electroosmotic flow
BGE	Background electrolyte
AC	Alternating current
DC	Direct current
MRI	Magnetic resonance imaging
PMMA	Polymethyl Methacrylate
Eq.	Equation
Tbl.	Table
Fig.	Figure
Sec.	Section
et al.	and others
FFF	Field-flow fractionation
DLVO	Derjaguin-Landau-Verwey-Overbeck
IEN	Georgia Tech Institute for Electronics and Nanotechnology
DI	Deionized
TIR	Total internal reflection
TIRF	Total internal reflection fluorescence
SNR	Signal-to-noise ratio
PTV	Particle tracking velocimetry
AOM	Acousto-optic modulator
CW	Continuous-wave
EM-CCD	Electron multiplying charge-coupled device
CMOS	Complementary metal oxide semiconductor
LOWESS	Locally weighted scatterplot smoothing

SUMMARY

Microparticle manipulation and assembly is a growing field with many applications such as novel material synthesis and particle assays. This doctoral thesis focuses on a novel method of microparticle manipulation and assembly called banding. Banding occurs when an aqueous electrolyte solution of nanoparticles suspended within a microchannel is acted on by a combination of a pressure gradient and direct current (DC) electric field acting in the same direction. Under the resulting combination of Poiseuille and electroosmotic flow in opposing directions, the particles assemble into multiple fluid, near-wall, streamwise structures called bands. Band formation occurs over three major stages: 1) the accumulation stage where particles are attracted to the channel wall, 2) the band formation stage where a large number of unstable bands are formed, and 3) the steady-state stage where the bands merge and separate into a smaller number of stable bands. Observed band properties suggest that they have potential for high-throughput near-wall particle manipulation and assembly.

This thesis will explore band properties and how they can be manipulated as well as conjecture the forces that lead to band formation, particularly during the accumulation and steady-state phases, using experimental results. This thesis will determine how to manipulate band formation by experimentally determining the required conditions for band formation. The fundamental forces behind band formation during the accumulation and steady-state stages of banding will also be conjectured through an analysis on band and particle behavior under different flow and particle properties in different locations in the microchannel. As an example, a wall-normal force is conjectured to drive the particles to

the channel wall in the accumulation phase which will be examined using particle counts near the channel wall during the accumulation phase.

To accomplish these objectives, the near-wall particles are illuminated with evanescent wave illumination and a video of the illuminated particles will be recorded. Evanescent wave illumination decays rapidly with particle distance from the channel wall, which causes this illumination method to be ideal for observing near-wall structures. The raw video data will be processed with MATLAB to determine band properties such as the total number of bands and the time required for bands to form. To observe individual particle dynamics, a specialized solution, using particles of similar properties but different fluorophores, will be used where one type will make up the bulk of the solution and the other type will be tracer particles. By selectively observing tracer particles, individual particle dynamics can be analyzed.

CHAPTER 1
INTRODUCTION

Within the last few decades, methods that use external forces to manipulate—*i.e.*, influence the positions or arrangements of suspended colloidal particles have become a popular research topic. Some potential applications include particle-based assays or using the particles as building blocks for the synthesis of complex structures (Dendukuri and Doyle 2009). This thesis investigates a novel method to manipulate suspended colloidal particles flowing through a microchannel using the combination of an external pressure gradient and a steady, or direct current (DC), electric field, or voltage gradient. Depending on the direction of the two gradients, significant cross-stream migration of the colloidal particles occurs, attracting them to the channel wall. Furthermore, if the voltage gradient is over a minimum value, the particles may assemble into flowing, streamwise structures called bands.

To better describe the experiments on bands discussed in this thesis and how bands compare to contemporary research on similar particle structures, this chapter will provide a brief overview of the typical properties of colloidal particles, how other groups have manipulated them, what structures have been formed from them, and what forces are thought to be involved. A more detailed, though specific, overview is discussed in Chapter 2. This chapter will then briefly discuss the main topic of thesis, bands and band formation, before ending in an overview of the rest of the thesis.

Section 1.1: Introduction to Colloidal Self-Assembly

Before the particles are manipulated, colloidal self-assembly begins with colloidal particles suspended in a colloidal solution. Colloidal particles are particles with hydrodynamic diameters of $O(1–10^3\ \text{nm})$ which come in a variety of shapes, such as spheres, ellipsoids, or rods, and a variety of different materials, with polymer (*e.g.* polystyrene, latex) and silica particles being some of the more common materials. Carbon nanotubes are also popular subjects for research. Colloidal solutions refer to colloidal particles suspended in a liquid, such as an aqueous electrolyte solution containing mobile ions, and in many cases, the particles are (nearly) density-matched to the suspending liquid. In such (nearly) density-matched colloidal solutions, the random motion of suspended particles due to thermal fluctuations of the surrounding liquid molecules, known as Brownian motion, is more significant than buoyancy which is significant since particles stay in suspension for a long period of time rather than undergoing sedimentation.

The electrolyte in the solution, also known as the background electrolyte (BGE), is significant since it modifies the electrokinetic forces in the solution which is closely related to a value known as the zeta potential described further in Chapter 2. The zeta potential ζ describes the electric potential around surfaces such as particle surfaces or the channel wall surface. One last note is that many groups will work with colloidal solutions containing one type of particle, where all particles of the same type have the same shape, zeta potential, and dimensions. This type of solution is often called a homogeneous particle solution. Other groups will work with particles of varying properties. These are often called heterogeneous particle solutions.

Colloidal self-assembly describes a broad variety of methods that influence colloidal particle positions or arrange many such particles into structures. Among these, there is a distinction between "direct" methods that use specific interactions, such as a modulated external field between carefully chosen building blocks, or "indirect" methods that use a substrate template or an unmodulated external field (Grelczk *et al.* 2010). For the purposes of this introduction and the literature review in Chapter 2, only colloidal assembly using indirect (*vs.* direct) methods will be described. Even with this restriction, colloidal self-assembly encompasses many different methods within many different environments.

Colloidal structures are assembled in a broad variety of environments and driven by a wide range of indirect stimuli. For example, many colloidal assembly methods apply an external alternating current (AC) or DC electric field between a pair of electrodes within a microchannel or simply within a droplet on top of a substrate containing electrodes. Static, crystalline particle structures then usually form between the electrodes. Other methods use an external pressure gradient to assemble colloidal structures within a microchannel. One interesting aspect of particle assembly using pressure gradients is that the gradient drives a flow of the colloidal solution and the particles typically form into dynamic structures in a liquid (*vs.* crystalline) arrangement. Many of these methods will take place within a microchannel that is defined by its depth since its width will be, comparatively, much larger. The high aspect ratio is advantageous since it minimizes the influence of the side channel walls. The strength of the gradient, positions of the electrodes, and/or dimensions of the channel are significant details for these processes.

There are several different types of structures that have been formed using colloidal self-assembly. Particles, used as building blocks, have been assembled into 1D "pearl chains" or lines of particles a single particle in cross section, chains that are several particles wide, 2D sheets that are many particles across, but have a thickness of at most a few particles, and 3D crystals. As one example, Velev and Bhatt (2006) described using polymer and silica microspheres, 1.4 mm in diameter, within a 100 μm deep microchannel with a much larger, 2–10 mm, width. Upon the application of an AC electric field, the particles formed 1D chains, which describes an arraignment where the particles are aligned into single-file but the overall path not a straight-line, often curving at random intervals. Furthermore, the particles subsequently assembled a 2D crystal, in which the particles are regularly spaced. An appropriate image of these formations can be seen in Fig. 3 of Velev and Bhatt (2006).

As another example, Snoswell *et al*. (2011) described the formation of dynamic particle clusters, whose positions and sizes evolved over time. These formations occurred within a 10 μm thick cell by applying a 65 kVrms/m electric field to a 0.8% volume fraction suspension of particles suspended in an aqueous solution with 2 mM KCl as an electrolyte. Their paper discusses how a disorganized group of particles formed elliptical clusters of particles where the particles in the clusters were found to accelerate from the tip to the center. They also found that these clusters would distort into regularly spaced streams of particles when a pressure gradient is applied on them. An appropriate image of these clusters can be found in Fig. 2 of Snoswell *et al*. (2011).

Section 1.2: Fundamental Mechanics behind Colloidal Self-Assembly

Despite the wide range of colloidal assembly methods reported in literature, there are far fewer papers that model and analyze the forces that cause colloidal assembly. The forces responsible for colloidal assembly can be roughly classified into two major groups based on their spatial range. The first group are short-ranged interparticle forces that act upon particles when they are separated by a particle diameter or less, which are thought to be responsible for the dense and regular arrangements of chains, sheets, or crystals that are typical of colloidal assembly. The other group are longer-ranged forces that act upon individual colloidal particles over distances comparable to the entire extent of the solution. These longer-ranged forces are significant when the particles are evenly dispersed in relatively dilute solutions and can, in some cases, locally concentrate the particles so that they can be manipulated and assembled via shorter-ranged interparticle forces.

Although there appears to be little understanding of the interparticle forces between particles in 2D sheets or 3D crystals, the mechanisms underlying the formation of 1D pearl chains are reasonably well understood. Particles in 1D pearl chains are assumed to form a string of induced dipoles where the positive end of one dipole is aligned with the negative end of an adjacent dipole (Gast and Zukoski 1989). Dipoles can be formed through innate particle polarity or if the particles are made of materials that can be modeled as leaky dielectrics. Other than pearl chains, a few groups have discussed forces between multiple particle chains forming in parallel. There are even fewer groups that discuss the lateral forces between 2D or 3D structures.

The induced dipole interparticle force, however, is very short-ranged. Upon the application of a pressure or voltage gradient within a microchannel, many groups have

observed and modeled a wall-normal "lift" force that manipulates the particles to concentrate at a specific region. For example, the wall-normal forces on particles influenced by a streamwise pressure gradient are known as inertial lift forces. For an electrokinetically driven flow, dielectrophoretic (DEP) and DEP-like forces have been described in literature. Two groups in particular have modeled the lift force on a particle affected by a combination of electrophoresis and inertial migration. Choudhary *et al*. (2019; 2021) studied the inertial lift on an electrokinetic sphere in combined electroosmotic and constant shear flow. Khair and Kabarowski (2020) demonstrated the existence of a lift force that was an electrokinetic analog of the Magnus effect.

Section 1.3: Bands and Band Formation

The band formation discussed on this thesis, which is also called banding, starts with a dilute suspension of fluorescent polystyrene (PS) particles with a particle radius a of about 245 to 500 nm, a particle zeta potential ζ_p of about −40 to −50 V, and a particle volume fraction φ_∞ of $O(0.1\%)$ in a weak aqueous electrolyte solution of about 1 mM sodium tetraborate decahydrate ($Na_2B_4O_7 \cdot 10\ H_2O$). This solution is placed within a microchannel that has a wall zeta potential ζ_w of about −110 mV, a depth H of 34 μm, a width W of about 300 μm, and a total length L of 4.2 cm. A streamwise pressure gradient dP/dx about $O(10^2$ to 10^3 Pa/cm) is applied through the channel and after the flow reaches steady-state, a streamwise voltage gradient $\vec{E}$ is applied where the magnitude of the gradient E is about $O(100$ V/cm). The Poiseuille and electroosmotic (EO) flow resulting from the pressure and voltage gradient respectively occur in opposite directions which is a condition called counterflow. The overall direction of flow, or the downstream direction,

is in the direction of Poiseuille flow. The coordinate x, as described in Chapter 2, is the distance downstream of the inlet of the straight portion of the channel. The coordinate y is in the wall-parallel, stream-perpendicular direction, also called the cross-stream direction.

The fluorescent particles are illuminated with evanescent wave illumination which decays exponentially the farther it penetrates through the channel wall, with a penetration depth z_p of 110 nm where the coordinate z is the distance from the channel wall, so that only particles in the near-wall region, defined as $z < a + 3\ z_p$, can be visualized. In this region, Poiseuille flow can be considered constant shear flow with experimental near-wall shear rates $\dot{\gamma}_w$ of $O(10^2–10^3\ s^{-1})$.

The experiments described in this thesis start with Poiseuille flow (and no electric field) and begin shortly after E is applied, or turned on, at time $t = 0$ s. In counterflow, particles are observed to concentrate near the channel wall. In addition, above a minimum E, the particles, once concentrated near the wall, subsequently form multiple highly elongated structures called “bands” that aligned with the flow, or streamwise, direction. These bands also have periodicity in the wall-normal, stream-perpendicular direction, which is known as the cross-stream direction. A sequence of evanescent-wave visualization images of near-wall particle concentration and band formation is shown in Fig. 1.1.

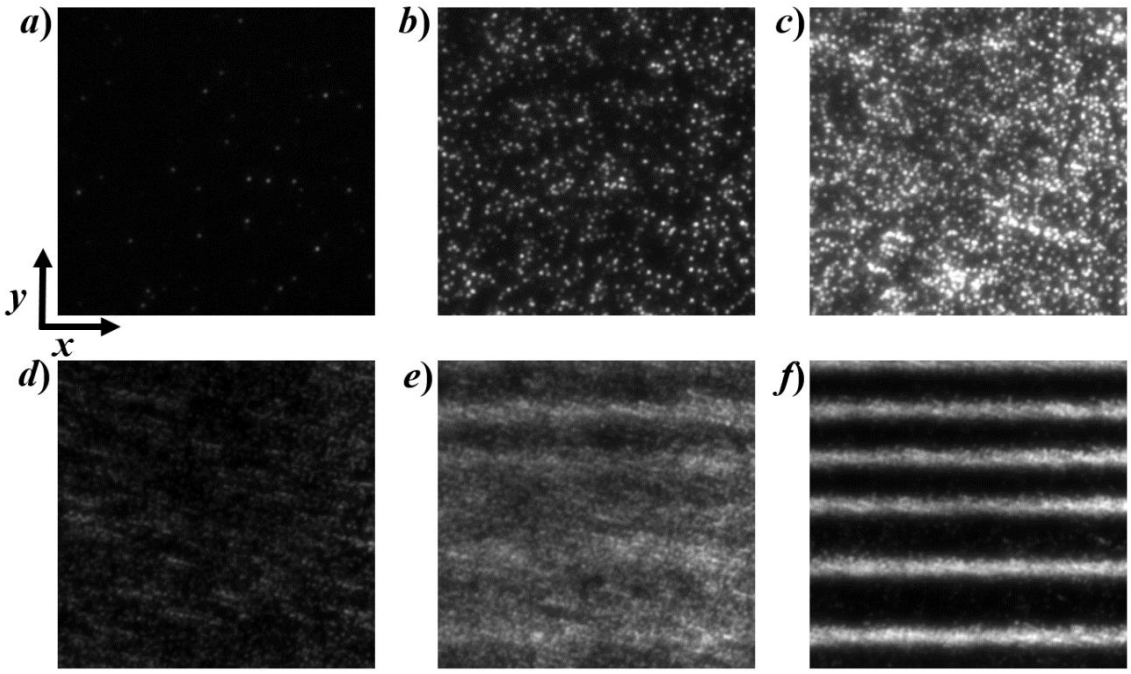

Figure 1.1: Evanescent-wave visualizations of suspended fluorescent PS particles ($\varphi_\infty = 1.7\times10^{-3}$) in combined Poiseuille and EO counterflow ($\dot{\gamma}_w = 1390\ s^{-1}$, $E = 47$ V/cm) at $x = 14.1$ mm for ***a*** $t = 0$ s , ***b*** 5.0 s, ***c*** 10.0 s, ***d*** 20.0 s, ***e*** 30.0 s and ***f*** 40.0 s. All the images have been contrast enhanced to improve their visibility; note that the enhancement of the top row of images is stronger than that for the bottom row.

Based on these observations, banding appears to consist of three stages:

1) ***accumulation***, where the particles are attracted to and become concentrated near the wall;
2) ***band formation***, where the particles assemble into a relatively large number of fairly unstable bands whose average intensity increases over time; and
3) ***steady-state***, where the band characteristics (average intensity, period) of the bands remain fairly consistent over time.

These band structures are distinct from previous colloidal particle structures, including those assembled using pressure gradients and/or electric fields, in several aspects. First, instead of the static structure and solution typical of many other colloidal particle structures, these structures are assembled in a flowing colloidal solution, and the particles

within the bands, which appear to be in a liquid (*vs.* crystalline) state, are convected along the flow direction. Due to this, the banding structure may be able to be formed and output continuously. Second, the bands exist along the entire length of the channel, with cross-section dimensions O(μm) and lengths of O(cm), which are hence at least an order of magnitude longer than the similar structures reported by Snoswell *et al*. (2011) or Serhatliogiu *et al*. (2020). Third, these bands only exist within a few μm of the wall and can be formed from extremely dilute—volume fractions as low as 3×10^{-5}—colloidal solutions.

Section 1.4: Thesis Objectives

The focus of this thesis is to experimentally study banding and the resulting band structures by analyzing visualizations such as those shown in Fig. 1.1. The objectives of this thesis are 1) to develop a consistent method for determining band characteristics, such as how long they take to form and the spacing between them, and to track particle positions and dynamics 2) to determine how band characteristics and particle velocities change under different flow or particle parameters such as E, $\dot{\gamma}_w$ or a, and 3) study the fundamental phenomena that cause banding using four conjectures explained below.

The conjectures that will be examined in thesis are:

1. Band formation is caused by interparticle forces such as induced dipoles that attract the particles into the band structure. If this is the case, the particles must be close enough together for these forces to be significant. Therefore, this conjecture can be tested by determining if the particles start to assemble into bands when the spacing between

particles in the near-wall region decreases below a critical value, or, alternatively, the number concentration of particles in the near-wall region reaches a critical value.

2. The wall-normal force predicted by the results of Choudhary *et al*. (2019; 2021) and Khair and Kabarowski (2020), referred as the modeled wall-normal force, is the major cause for particle migration towards the channel wall during the accumulation stage. As discussed in Secs. 6.2 and 6.3, a model of the particle *z*-positions during the accumulation stage, which incorporates this wall-normal force, predicts that the near-wall particle count grows linearly with time. The timescale for band formation and the expected growth rate of the particles during the accumulation stage will be used to test this conjecture.
3. Band formation is a convective phenomenon since simple observations suggest that the bands are flowing structures. This can be tested in two ways. The first would be to observe individual particle velocities. The second, more indirect method, would be to determine if the timescale for band formation scales with *dP/dx* since, considering the entire velocity profile, Poiseuille flow is more significant than electroosmotic flow or electrophoresis for the experimental parameters used in this thesis. Since $\dot{\gamma}_w$ scales linearly with *dP/dx*, as mentioned in Sec. 2.5, an alternative method would be to test if the timescale for band formation scales with $\dot{\gamma}_w$.
4. Particle velocities are less than the expected velocity due to the combination of Poiseuille flow, Smoluchowski electroosmotic flow and Smoluchowski electrophoresis. One reason for this conjecture is that the presence of even a single near-wall particle may distort the nearby electric potential and flow fields which would alter the particle velocity. In addition, the presence of multiple nearby particles,

especially during band formation and within the bands at steady-state may also reduce the particle velocity.

Section 1.5: Summary of Thesis Chapters

The contents of the doctoral thesis are organized in the following manner. Chapter 2 is a literature review discussing relevant literature of wall-normal lift forces, expected particle velocities, particle assembly techniques and resulting structures. Chapter 3 will discuss the experimental setup and procedures required to record raw videos of band formation or individual tracer particles in the solution. Chapter 4 will discuss how these raw videos are processed in MATLAB version R2019b to determine band properties or particle dynamics. Chapter 5 presents the results of overall band properties. Chapter 6 discusses the results on individual particle dynamics. Lastly, Chapter 7 summarizes the major contributions of this doctoral thesis.

CHAPTER 2
LITERATURE REVIEW AND BACKGROUND INFORMATION

This chapter reviews relevant literature and background information on the forces that may act upon the particles during banding, the expected particle velocity, and compares bands with similar particle structures created by colloidal self-assembly. The order of the topics discussed in this chapter is based on the three stages of band formation. As mentioned in Chapter 1, band assembly consists of the following three stages:

1) particle accumulation

2) band formation

3) steady-state

In the particle accumulation stage, the majority of the particles presumably enter the channel as a dilute solution where the average particle spacing is about 4 μm or $O(17a)$, as described in Sec. 6.2. For such a large interparticle spacing, interparticle interactions should be negligible. Moreover, assuming particles enter the channel at random distances from the channel wall, the average particle z upon entering the channel should be $H/4$. The ratio $H/4a = 17$ suggests that the particle-wall interaction is also negligible. Thus, the attraction of particles to the channel wall in the accumulation stage is due to fluid-particle interactions, and hence the externally applied DC electric field and shear flow. Therefore, a review of previous literature on wall-normal "lift" forces is discussed in Sec. 2.2. To better understand wall-normal "lift" forces and streamwise particle velocities, as well as the interparticle forces and particle-wall forces discussed later in Sec. 2.5, a description of the electric double layer that encompasses the particles and channel wall is given in

Sec. 2.1. Forces that may act on the particles but are not directly caused by an applied pressure or voltage gradient are discussed in Sec. 2.3.

At the beginning of the band formation stage, there are many particles concentrated near the channel wall and the interparticle separation becomes much smaller, about 5.9 μm or $O(2a)$ as described in Chapter 6. As these closely spaced particles begin to assemble into the structures called "bands", interparticle and particle-wall interactions are likely to be significant during this stage. Hence, Sec. 2.4 discusses DLVO theory and Sec. 2.5 reviews the expected flow and particle velocity, including the effects of particle-wall interactions. Note that for spherical particles, instead of particle center to wall distance, described in this thesis as z, many groups describe particle position by the minimum distance between the particle surface the wall $h \equiv z - a$.

In the final steady-state stage of banding, the particles are arranged into flowing, densely packed structures that are a few microns wide and, based on observations, extend over the entire length of the microchannel of 4.2 cm, including the bends. Although a variety of structures can be formed near the channel walls using directed assembly, these bands are distinct to our knowledge in that they are flowing structures that form centimeters from the electrode, as discussed in Sec. 2.6, which reviews the literature of directed assembly. Sec. 2.7 reviews literature on what is known about the forces/mechanisms that may cause the assemblies described in Sec. 2.6 to form.

Section 2.1: Description of Electric Double Layer

Many of the forces and velocities discussed later in this chapter such as Derjaguin-Landau-Verwey-Overbeek (DLVO) theory, electroviscous lift, and dielectrophoretic lift,

are dependent on the cloud of counterions surrounding, and screening, the charged surface of an object in a conducting medium which is called the electric double layer (EDL). When a dielectric surface, such as that of a polystyrene (PS) particle or a glass wall, is exposed to a conducting medium, that surface becomes charged through various mechanisms such as the ionization or dissociation of surface groups, adsorption or binding of ions from the background electrolyte (BGE) solution, and ion exchange between dissimilar surfaces in close proximity (Israelachvili 2011, Chapter 14). Silica surfaces like glass, (Kirby and Hasselbrink 2004a, Behrens and Grier 2001), which are also found as native oxide layers on silicon itself, or polymer surfaces (Kirby & Hasselbrink 2004b), both of which are common in microfluidics applications, are for the most part negatively charged, except in strongly acidic solutions (pH < 2). These charged surfaces then attract the mobile counterions (cations from the BGE for negatively charged surfaces) from the medium to form the EDL.

EDLs of a suspended particle and channel wall in an electrolyte solution of the same sign will repel each other with a force whose magnitude depends on the zeta potential of the charged surface, ζ. The EDL consists of two regions: *i)* the inner Stern layer consisting of counterions immobilized by electrostatic forces; and *ii)* the outer diffuse Chapman-Gouy layer, where the counterions are mobile because of thermal effects. The electrostatic potential at the so-called "slip plane" where the particle velocity is assumed to be 0 is called the ζ(zeta)-potential, which is commonly used to characterize the surface charges of both the particle and the wall. Many of the models discussed in this channel assume that the EDL is thin compared to the size of the particles in solution, also known as the thin EDL approximation. The EDL does not have a definite thickness since the

counterions surrounding a particle surface, for example, simply becomes sparser the further one goes from the particle surface. However, a value called the Debye length κ^{-1} is typically used as an indication of EDL thickness.

The Debye length is defined as

$$\kappa^{-1} = \sqrt{\frac{\varepsilon_r \varepsilon_0 k_B T}{2 N_A q_e^2 I}} = \sqrt{\frac{\varepsilon k_B T}{2 N_A q_e^2 I}} \quad [2.1]$$

where ε_r is the dielectric constant of the solution, ε_0 is the permittivity of a vacuum, k_B is Boltzmann's constant = 1.38×10^{-23} $m^2\cdot kg\cdot s^{-2}\cdot K^{-1}$, T is the temperature of the solution which is measured in the lab to be about 21 °C, N_A is Avogadro's number = 6.022×10^{23} mol^{-1}, q_e is the elementary charge = 1.60×10^{-19} C, and I is the ionic strength of the solution. The solution permittivity $\varepsilon \equiv \varepsilon_r\varepsilon_0$.

The ionic strength is dependent on the BGE and is defined as

$$I = \frac{1}{2}\sum_{i=1}^{n} c_i Z_i^2 \quad [2.2]$$

where c_i is the molar concentration of ion I and Z_i is the ionic strength of the i^{th} ion. As discussed in Sec. 6.2, the Debye length of the particles in the experiments κ^{-1} = 7 nm and ratio $\kappa a = 35 >> 1$ suggests that the thin EDL approximation is appropriate. Note that although the location of the slip plane is intrinsically not the boundary between the Stern and diffuse layers of the EDL, this is assumed to be the case under the thin EDL approximation.

Section 2.2: Wall-Normal Forces

During the accumulation stage, particles are attracted towards the channel wall. This is unexpected since literature on wall-normal lift forces typically describes repulsive

forces such as literature that focuses on particles in constant shear flow, which is often used to discuss Poiseuille flow, or those that focus on particles under a streamwise electric field, either alternating current (AC) or direct current (DC). Moreover, there are often conflicting statements on how these forces scale with the applied external field. At the end of this section, two particular groups are mentioned which discuss an attractive wall-normal lift force under the specific conditions of a DC electric field and a constant shear flow which are conditions that are similar to the experiments in this thesis.

This section is broken up into literature discussing wall-normal lift forces in either constant shear flow or Poiseuille flow, literature discussing wall-normal lift forces under electric fields, and literature discussing a combination of the two. In this chapter, unless otherwise stated, if the model includes the effect of walls, the walls are assumed to extend infinitely and there is no influence of side walls. In addition, unless otherwise stated, shear flow refers to constant or uniform shear flow where the shear, in regions far away from the particle, is constant at all locations.

Section 2.2.1: Lift Forces in Shear Flow

Known literature on lift forces in shear flow describes such forces as mostly repulsive although there are conflicting statements on how this force scales with the applied shear rate. Although Rubinow and Keller (1961) were the first to include the effect of inertia on the lift force for a rotating spherical particle moving in a viscous fluid (*i.e.* Magnus effect) at low *Re*, perhaps the earliest and best-known study of inertial lift forces was that of Saffman (1965). In this study, the inertial lift force on a sphere moving under unbounded shear flow (*i.e.*, in the absence of walls) in a viscous fluid was calculated

using the method of matched asymptotic expansions, defining three distinct Reynolds numbers:

$$Re_{\dot{\gamma}} \ll \frac{\dot{\gamma} a^2}{\nu} \qquad Re_{U} \ll \frac{U_s a}{\nu} \qquad Re_{\Omega} \ll \frac{\Omega a^2}{\nu} \qquad [2.3]$$

where ν is the fluid kinematic viscosity, U_s is the particle streamwise velocity relative to the fluid (*i.e.*, the slip velocity) and Ω is the angular velocity of the particle. For the case where all three Reynolds numbers < 1, the lift force:

$$F_{L,saff} = 6.46 \mu U_s a^2 \left(\frac{\dot{\gamma}}{\nu} \right)^{\frac{1}{2}} \qquad [2.4]$$

However, it should be noted that Eq. 2.4 is valid only in the high shear limit, or when $U_s \ll (\nu \dot{\gamma})^{1/2}$. In the original paper, the constant in Eq. 2.4 was 81.2, but was later corrected to 6.46 (Saffman 1968). Saffman's study revealed several important characteristics regarding the lift forces in Poiseuille flow. First, it showed that the lift due to particle rotation for a freely rotating particle is negligible, which agrees with the results of Rubinow and Keller. Second, the direction of the lift force is determined by the direction of U_S: if the particle is slower than the undisturbed local flow (*i.e.*, lags the flow), the lateral migration is towards the high flow-velocity region, *i.e.*, away from the wall, and vice versa. Third, Eq. 2.4 suggests that there is a lift force only if there is "slip" between the particle and the fluid. This behavior explains earlier observations of lift forces for non-neutrally buoyant particles in vertical channel flows. In these situations, buoyancy effects result in significant particle-fluid slip velocities due to sedimentation as opposed to neutrally buoyant particles, where the only possible source of slip is the weak retardation due to the presence of the wall (Goldman *et al*. 1967a, 1967b).

Saffman's analysis has expanded upon by numerous researchers. Cox and Brenner (1968) included the effect of a nearby wall, assuming that the wall lies within region of the flow disturbance created by the particle in a Poiseuille flow. They concluded that the inertial lift force magnitude scales with $(U/H)^2$ and a^2 although they did not give an explicit expression for the lift force. Ho and Leal (1974) estimated the lift force for a particle in shear flow and 2D Poiseuille flow between two infinite parallel plates when the particle is far from the walls using the method of reflections. Their results reported that the lift force in the bulk of the flow is proportional to a^4 and $\dot{\gamma}^2$, which differs from the scaling predicted by Saffman in Eq. 2.4. Leighton and Acrivos (1985) then analyzed a sphere in shear flow touching the wall and reported that the lift force is always away from the wall with a scaling similar to that found by Ho and Leal for a and $\dot{\gamma}$. McLaughlin extended Saffman's analysis to lower $\dot{\gamma}$ for unbounded shear flows (1991), and later on to shear flows bounded by a single wall (1993). The results of the latter study were experimentally confirmed by Takemura and Magnaudet (2009). Perhaps the most complete study was Cherukat and McLaughlin (1994), who estimated the inertial lift acting on a spherical particle in shear flow bounded by a single wall for a range of z.

Although the theoretical studies discussed so far mostly focused on single-particle interactions, Han *et al.* (1999) used magnetic resonance imaging (MRI) of the flow of neutrally buoyant a = 255 μm polymethyl methacrylate (PMMA) particles to show that there was inertial lift in suspensions at volume fractions φ as great as 0.2, reporting that the equilibrium positions of particles were consistent with the earlier observations of Segre and Silberberg (1962a).

All of these shear-induced inertial lift force studies are valid for small particle-scale $Re_p < 1$ in the low-but-finite (channel) *Re* limit of the flow, *i.e.*, $Re = O(1)$. More recent studies have instead considered higher Reynolds numbers $Re = O(10^2–10^3)$ (Asmolov 1999, Matas *et al*. 2004a, Zeng *et al*. 2005, Asmolov *et al*. 2018), but these are beyond the experiments detailed in this thesis.

These forces have also been used for various purposes. Recent papers discuss inertial lift forces at low *Re* which are used for "inertial microfluidics" where particles are manipulated and focused during flow cytometry as reviewed by Di Carlo (2009). Matas *et al*. (2004) described the theory relating the shear-induced inertial lift force on a particle in the presence of a wall to its potential streamwise location by discussing three components of the lift force. The first component is caused by the interaction of the flow disturbance between U_s and the nonuniform velocity field in the far-field, which is usually shear flow. As explained earlier, this force can be an attractive lift force (towards the wall) or a repulsive lift force (away from the wall), depending on the sign of U_s. The second component is caused by the interaction of the flow disturbance between the particle and the wall if the wall lies in the inner region of the flow disturbance. This is always a repulsive lift force. The third component is caused by the curvature of the velocity profile, such as in the parabolic profile typical of Poiseuille flow. In Poiseuille flow, the relative flow velocity in the side of the particle facing the wall will be lower than on the opposite side of the particle, even if there is no slip between the particle and the suspending fluid. The resultant pressure difference between the two sides of the particle leads to a repulsive lift force. The cumulative effect of these three components explains the "tubular-pinch" phenomena, where particles concentrate at certain radial positions.

Finally, shear-induced lift forces have also been reported in field-flow fractionation (FFF) literature which describes particle separation techniques based on different particle properties such as a. Williams *et al.* (1996a; 1996b) reported that the lift force on a = 5–20 μm near-wall PS particles suspended in a fluid with viscosities $\mu < 2$ cP in shear flow were not completely accounted for by inertial lift forces (Cox and Brenner 1968, Ho and Leal 1974). They suspected that there was an additional contribution to the lift force due to the proximity of the wall. They termed this additional force the "hydrodynamic lift" and based upon their results, it scaled with a^3 and $\dot{\gamma}$, which does not agree with the other theories for inertial lift forces. Recently, Ranchon *et al*. (2015) used bright-field microscopy studies, validated by Brownian dynamics simulations, of the dynamics of a = 100 nm–150 nm particles suspended in a solution consisting of 160 mM Tris (hydromethyl) aminomethane hydrochloride or Tris-HCl, 160 mM boric acid, 5 mM ethylenediaminetetraacetic acid or EDTA, and glycerin in Poiseuille flow through 0.9 μm–1.9 μm deep channels. They reported that there were few, if any, particles within 60 nm of the wall which was attributed to the existence of a repulsive lift force of O(0.1 pN) with a magnitude proportional to $\dot{\gamma}$, suggesting that they also observe hydrodynamic lift.

Charged particles suspended in a conducting fluid are also subject to shear-induced lift due to electroviscous effects. This force is called electroviscous, or shear-induced electrokinetic, lift. Alexander and Prieve (1987) first studied electroviscous lift and reported a repulsive lift force on a = 8–18 μm polystyrene (PS) particles suspended in water-glycerol mixtures in shear flow bounded by a wall. Since the force magnitude depended weakly on $\dot{\gamma}$, they conjectured that this force was caused by electroviscous effects because its magnitude appeared to decrease as the ionic strength of the BGE

increased. Electroviscous lift is caused by the polarization of the EDL due to the convection of the mobile counterions within the EDL by the flow which leads to a breakdown in the symmetry of the Maxwell stress tensor near the wall.

In later studies, Prieve and his co-workers developed models of electroviscous lift based on lubrication theory (Bike and Prieve 1990) and later extended this model by relaxing the lubrication approximation (Bike and Prieve 1992), considering only the Maxwell stress tensor. Warszyński *et al*. (1998) as well as Warszyński and van de Ven (2000) analyzed electroviscous lift including hydrodynamic effects as well as the Maxwell stress tensor. Perhaps the most complete analysis of this problem was that by Schnizer and Yariv (2016), who used the generic macroscale model developed by Schnizer *et al.* (2012), which was valid for Péclet numbers of $O(1)$ to model particle-pair sedimentation and shear-induced lift.

Section 2.2.2: Lift Forces in DC Electric Fields

Recent studies have revealed that microparticles near a wall experience a lift force normal to the electric field direction in electroosmotic flow (EOF) (Saiki and Sato 2004). Similar to the lift forces reported for shear flows, lift forces in EOF have been observed to be repulsive with controversy on how this force scales with E. Young and Li (2005) were the first to investigate this force theoretically for a dielectric colloidal particle migrating in an electrokinetically driven flow. They conjectured that when the particle is near the wall, the distortion of the electric field lines in the particle-wall gap results in an electric field gradient perpendicular to the wall, which eventually causes a dielectrophoretic(DEP)-like lift force that repels the particle away from the wall, where the lift is “dielectrophoretic-

like" because it is due to a nonuniform electric field acting on the particle. The magnitude of the lift force was estimated by numerically integrating the Maxwell stress tensor around the particle and was found to scale as E^2 and a^2; for a = 0.5 μm, the DEP-like force potentials were found to be comparable in magnitude to DLVO potentials for h < 1 μm. As expected, the force magnitude decreases as the particle moves away from the wall, presumably because the electric field surrounding the particle becoming more uniform at larger separations. In a well-known analytical study, Yariv (2006) derived an expression for the DEP-like lift force instead by integrating the Maxwell stress tensor around the particle, employing the thin EDL assumption, for the remote particle case where $a \ll a + H$. The lift force scaling was consistent with the results of Young and Li (2005); however, the lift force magnitude was twice that predicted by Yariv for $H/a \geq 1$. In a recent study, Yariv (2016) extended his previous theory to moderately large (particle and wall) zeta-potentials where the thin EDL assumption no longer holds and so the effects of particle surface conduction and the resulting particle polarization are no longer negligible. The study derived a more general expression for the lift force magnitude that includes surface conduction effects for the case of a remote particle. Khair and Balu (2019), who derived the lift force of a translating and rotating rigid sphere under the influence of an electric field, concluded that the magnitude of this force was proportional to a^2 and E.

The first experimental characterization of DEP-like lift forces appears to be that by Liang *et al*. (2010a), who showed that a = 2.5–5 μm PS particles were "focused" in, *i.e.*, concentrated about the centerline of, a 25 μm × 50 μm rectangular cross-section PDMS channel when the flow was driven by a DC electric field. One notable observation of their work is that particle focusing was more intense at downstream locations. Their lift force

estimates showed that the lift force magnitude scaling with E and a was consistent with earlier theoretical studies; however, the experimentally determined lateral migration of the particles was much greater than that predicted by Yariv's study (2006). In a follow-up study, the authors (Liang *et al*. 2010b) extended their previous study to a 25 μm square channel and observed focusing of neutrally buoyant particles along both cross-stream directions.

Evanescent-wave based particle tracking has also been used to verify the existence of such lift forces. Kazoe and Yoda (2011) used multilayer nanoparticle tracking (Li and Yoda 2008) to estimate the lift forces for smaller a = 240–463 nm PS and silica particles in EO flows through 34 μm deep fused-silica microchannels. Although the lift force magnitude was proportional to E^2 and a^2 in agreement with earlier studies, the estimates of these magnitudes were roughly an order of magnitude greater than those predicted by Yariv's theory (2006). It should, however, be noted that only near-wall particles are visualized by evanescent-waves, and so the force measurements were limited to $50 \le H \le 300$ nm, corresponding to $a + H = 545$ nm for $a = 245$ nm particles. These estimates are therefore not for the "remote" particles analyzed by Yariv (2006).

Despite the significant (at least an order of magnitude) discrepancies between theory and observations, these DEP-like lift forces have recently been used to separate and manipulate microparticles in microfluidic devices. Lu *et al*. (2014) separated binary and ternary mixtures of a = 1.5, 2.5 and 10 μm PS particles based on particle size in a T-shaped microchannel. Similarly, Liang *et al*. (2015) used DEP-like lift forces to control the particle-wall separations of a = 7.5–20 μm PS particles by varying the applied DC field and estimated the particle electrophoretic mobilities as a function of particle-wall separation.

Thomas *et al*. (2017) instead separated similarly sized PS particles based on their surface charge density, specifically fluorescently labeled and unlabeled $a \approx 2.5\,\mu\text{m}$ particles in a continuous microchannel flow.

Section 2.2.3: Lift Forces in Combined EO and Shear Flow

Recent observations of suspended particles subject to both shear flow (due to Poiseuille flow) and EO flow (due to a DC electric field), shows that the particles are either strongly repelled from, or attracted to, the wall depending on the relative directions of the Poiseuille and EO flows (Cevheri and Yoda 2014b). While particle repulsion from the wall occurs when both flows are in the same direction ("coflow"), simply reversing the polarity of the electric field ("counterflow") will instead cause particles attraction towards the wall. The magnitude of this lift appears to scale with E in both cases, suggesting that it is electrophoretic (vs. dielectrophoretic), and with $\dot{\gamma}_{\text{w}}^{N}$ for coflow, where $N \approx 0.5$. These results suggest that the (undetermined) mechanisms for the lift forces observed in combined Poiseuille and EO flow are fundamentally different from those observed in Poiseuille flow alone, or EO flow alone.

Despite numerous studies of combined EO and Poiseuille flows in microfluidic devices, there are few studies that consider the dynamics of colloidal particles suspended in such flows. Two known studies are Choudhary *et al*. (2019; 2021) and Khair and Kabarowski (2020) who considered a single particle suspended in a constant shear flow of magnitude $\dot{\gamma}$ and subject to a DC electric field with a flow $Re << 1$. The theoretical wall-normal force, as described in Choudhary *et al*., is attributed to particle-fluid slip whereas

Khair and Kabarowski attribute this force to weak instantaneous inertia. Both models give the same scaling for the magnitude of the wall-normal force, namely:

$$F_{\mathrm{L}} = 1.75\pi \frac{\varepsilon \left|\zeta_{\mathrm{p}}\right| a^3 \dot{\gamma} E}{\nu} \qquad [2.5]$$

where F_{L} is the attractive wall-normal lift force. Although the two original models (Khair and Kabarowski 2020; Choudhary *et al.* 2019) gave different constants of proportionality, a subsequent analysis by Choudhary *et al.* (2021) including higher-order velocity terms found that this constant was 1.75π which agreed with the results from Khair and Kabarowski.

Section 2.3: Buoyancy and Drag Force

Two other forces that could potentially have a significant effect on the particle wall-normal force during accumulation are buoyancy and drag.

The buoyancy force on a spherical particle is:

$$F_{\mathrm{B}} = (\rho_{\mathrm{s}} - \rho_{\mathrm{p}}) \forall_{\mathrm{p}} \, g = \Delta\rho \left(\frac{4}{3} \pi a^3 \right) g \qquad [2.6]$$

where F_{B} is buoyancy, $\forall_{\mathrm{p}}$ is the particle volume, g = 9.81 m/s^2 is the magnitude of the gravitational acceleration, ρ_{s} is the solution density and ρ_{p} is the particle density. Since the particle density is well matched with the solution density for the experiments discussed in this thesis, this force is probably negligible but will be addressed in Chapter 6.

The Stokes drag on a spherical particle is:

$$\vec{D} = -6\pi\mu a \frac{\partial \vec{U}}{\partial t} \qquad [2.7]$$

where $\vec{D}$ is the Stokes drag and $\vec{U}$ is the particle velocity. Since the Stokes drag is scaled to the particle velocity, it causes the particle to have a terminal velocity rather than accelerating infinitely in the solution.

Section 2.4: DLVO Theory

In the absence of flow, the combination of electrostatic interactions and van der Waals forces can describe the equilibrium position of a suspended particle near a channel wall in what is described as classic Derjaguin-Landau-Verwey-Overbeek (DLVO) theory (Derjaguin & Landau 1941, Verwey 1948). Van der Waals forces originate from intermolecular interactions and are generally weak in comparison to chemical electric bonds such as covalent bonds and ionic bonds. The four main types of intermolecular interactions are:

i) repulsive interactions due to the Pauli Exclusion Principle,

ii) attractive interactions between molecules with permanent dipoles (Keesom forces),

iii) attractive interactions due to a permanent and an induced dipole (Debye forces), and

iv) attractive interactions due to two induced dipoles (dispersion or London forces) (Israelachvili 2011).

The total interaction potential between the particle and the wall is then simply the superposition of the van der Waals and electrostatic EDL interaction potentials. This potential can be described as a potential energy profile along the wall-normal direction. An ensemble of particles will then have a nonuniform distribution along the wall-normal direction with the peak of the distribution (*i.e.*, the location with the largest number of

particles) corresponding to the minimum in this potential energy profile (Israelachvili 2011).

Although DLVO theory has been used to study the stability of dilute colloidal suspensions for more than 60 years, this theory begins to fail when the separation between the particle and the wall becomes less than about 10 nm because additional interactions, called the non-DLVO forces (*e.g.* hydrophobic, steric and hydration forces) become significant at these spatial scales (Adler *et al*. 2001; Israelachvili 2011). Although describing these forces remains an active field of research, such small particle-wall separations are not considered in this thesis.

Hamaker (1937) discussed the London-van der Waals force and expressed the potential energy between two spheres of diameters D_1 and D_2 as:

$$E_{\delta p} = -\frac{A}{12}\left(\frac{R_1}{d_1^{\,2} + d_1 R_1 + d_1} + \frac{R_1}{d_1^{\,2} + d_1 R_1 + d_1 + R_1} + 2\ln\left\{ \frac{d_1^{\,2} + d_1 R_1 + d_1}{d_1^{\,2} + d_1 R_1 + d_1 + R_1} \right\} \right) \quad [2.8]$$

where $E_{\delta p}$ is the potential energy, A is the Hamaker constant, $R_1 = \frac{1}{D_1}\left(\delta - \frac{D_1 + D_2}{2} \right)$ where δ is the particle spacing from the centers of the two spheres, and $d_1 = D_2 / D_1$. The particle-wall force can be estimated by considering a sphere with an "infinite" diameter or radius. Using Eq. 2.8, the potential energy between a sphere of radius $R_1 \equiv D_1 / 2$ and a planar wall, where $D_2 \to \infty$, becomes:

$$E_{\delta w} = -\frac{A}{12}\left(\frac{1}{d_3} + \frac{1}{d_3 + 1} + 2\ln\left\{ \frac{d_3}{d_3 + 1} \right\} \right) \quad [2.9]$$

where $E_{\delta w}$ is the potential energy and $d_3 = h / R_1$. The interparticle or particle-wall force can be determined from Eqs. 2.8 and 2.9 respectively through the derivative of the potential energy with respect to the interparticle spacing or particle-wall distance respectively.

Section 2.5: Near-Wall Streamwise Fluid and Particle Velocity

The flow velocity profile in laminar, unidirectional, incompressible, and steady flow can be determined by applying the Navier-Stokes equations and boundary conditions that there is no flow at the walls ($z = 0$ and $z = H$). The result is the well-known parabolic flow profile called Poiseuille flow:

$$U_{po} = \frac{1}{2\mu}\frac{dP}{dx}\left(z^2 - Hz\right) \qquad [2.10]$$

where U_{po} is the flow velocity due to Poiseuille flow, μ is the fluid dynamic viscosity and dP/dx is the magnitude of the pressure gradient. Within a region near the channel wall, U_{po} can expressed as a linearly varying velocity profile with a constant slope, or near-wall shear rate $\dot{\gamma}_w$.

$$U'_{po} = \dot{\gamma}_w z \qquad [2.11]$$

where U'_{po} is the estimate of the Poiseuille flow in the near-wall region. As described in Chapter 3, the near-wall region illuminated during experiments is $z < a + 3\ z_p$ with $\dot{\gamma}_w$ being determined at $z = a + 1.5\ z_p$. Considering H, the maximum difference between U_{po} and U'_{po} is less than 0.6% of U_{po}, implying that U'_{po} is an acceptable expression for the near-wall flow velocity. As for the variation in $\dot{\gamma}$ over the illuminated region, as determined from Eq. 2.10, the difference between any $\dot{\gamma}(z)$ in the illuminated region and

$\dot{\gamma}_w$ is less than 1.5% of $\dot{\gamma}_w$, implying that the near-wall flow can be considered constant shear flow.

When a steady (DC) external electric field of magnitude *E* is applied instead to a microchannel along its axis, the fluid and mobile counterions in the EDL screening the charged wall will flow towards the anode or cathode, depending on their charge, along the electric field direction, which will be the streamwise direction for this thesis. The neutral fluid in the bulk of the channel will then also be set into motion by viscous effects, *i.e.*, the no-slip condition. Hence, the resulting electroosmotic (EO) flow has a uniform velocity profile in the neutral bulk fluid with a velocity that is proportional to the wall zeta-potential ζ_w and a boundary-layer like profile in the charged fluid in the (very) thin EDL. The uniform steady and unidirectional flow velocity is given by the Helmholtz-Smoluchowski equation:

$$U_{eo} = \frac{\varepsilon E \zeta_w}{\mu} \qquad [2.12]$$

where U_{eo} is the flow velocity due to electroosmotic flow and ζ_w is the wall zeta potential.

Under a combination an applied pressure and voltage gradient, several sources describe the flow velocity profile for combined flow as merely the superposition of the flow velocity profiles Poiseuille and EOF. Dutta and Beskok (2001) analytically examined a mixed electroosmotic/pressure driven flow and obtained a flow velocity profile that was the superposition of both flows. Monazami and Manzari (2007) analytically studied a simultaneous application of pressure gradient and electroosmotic pumping mechanisms where the same result is suggested in their data.

Therefore, it is plausible to describe the expected flow velocity in the channel near the wall as the superposition of Eqs. 2.11 and 2.12,

$$U_{\mathrm{f}} = \dot{\gamma}_{\mathrm{w}} z + \frac{\varepsilon E \zeta_{\mathrm{w}}}{\mu} \qquad [2.13]$$

where U_{f} is the expected near-wall flow velocity.

If a particle with a charged surface is suspended in EO flow, the electric field will also drive the particle towards the anode or cathode depending upon the surface charge of the particle, a phenomenon known as particle electrophoresis. The electrophoretic velocity of the particle in the neutral bulk fluid U_{ep} is also given by the Helmholtz-Smoluchowski equation:

$$U_{\mathrm{ep}} = -\frac{\varepsilon E \zeta_{\mathrm{p}}}{\mu} \qquad [2.14]$$

where U_{ep} is the particle velocity relative to flow due to electrophoresis and ζ_{p} is the particle ζ-potential.

While an initial estimate of the expected near-wall particle velocity could be the superposition of U_{f} and U_{ep} as described in Eqs. 2.13 and 2.14 respectively, this expression would not consider wall effects. Several groups have modeled near-wall spherical particle velocities in either a constant shear flow or a DC electric field and reported a comparison between the expected particle velocity and the expressions given in Eqs. 2.11, 2.12 and 2.14.

Goldman *et al.* (1963) modeled a spherical particle suspended in constant shear flow near a wall (in the absence of an electric field) and determined the particle velocity along the flow (x) direction as well as the particle rotation by solving the Stokes equation with the following boundary conditions: 1) no slip at the wall; 2) the velocity far from the

wall is constant shear flow; and 3) no slip at the particle surface. The actual velocity of a particle suspended in shear flow near a wall can then be expressed as $G_w \dot{\gamma}_w z$ where the factor G_w, where $G_w \leq 1$, decreases with z, and $G_w = 1$ when wall effects are negligible. Although G_w is difficult to solve for, Tbl. 2 of Goldman *et al.* is a table of G_w for various values of z / a.

The electrical potential field will also be asymmetric around the particle, and "distorted" in the gap between the particle and the wall. Keh and Chen (1989) considered a particle close to a single surface subject to a uniform applied electric field E. To determine the local electric potential field, the Laplace equation was solved under the boundary conditions that: *a*) the current flux normal to the wall and particle surfaces was zero; and *b*) the potential gradient far from the surfaces is equal to the uniform applied electric field. Keh and Chen obtained a general solution for the local electric potential field that satisfied condition (*b*), then estimated the coefficients of their general solution by applying condition (*a*) and iterated until their solution satisfied (*a*) with negligible error. They then determined the fluid velocity field from the Stokes equation using this potential field ϕ under the conditions that *a*) the fluid velocity "slips" off the surface at a magnitude of $\left(\varepsilon \zeta_w \nabla \phi\right) / \mu$ for the wall and $\left(\varepsilon \zeta_p \nabla \phi\right) / \mu$ for the particle; and *b*) the fluid velocity far from the surfaces is $\left(\varepsilon \zeta_w E\right) / \mu$.

After assuming that the total force and torque exerted on the particle by the fluid was zero and decomposing the particle dynamics into three components: 1) a sphere translating parallel to the wall without rotation, 2) a sphere rotating near the wall without translation, and 3) a sphere translating normal to the wall, also without rotation, they determined the streamwise velocity and rotation of the particle. They then estimated the

ratio of the particle streamwise velocity and that given by the Smoluchowski equation as a function of the particle-wall separation normalized by *a*, and noted that the electrophoretic mobility was enhanced due to the compression of electric field lines and an increase in the viscous drag.

Yariv and Brenner (2003) also considered a single spherical particle subject to a global uniform electric field. Using the same boundary conditions and assumptions as Keh and Chen (1989), they used asymptotic analysis and the reciprocal theorem to solve for the particle electrophoretic mobility considering an inner region where the electric field and velocity gradients are large and an outer region where these changes were assumed to be moderate. Their results matched Keh and Chen's results; in particular Fig. 3 from Yariv and Brenner (2003) provided results that were similar to Tbl. 1 of Keh and Chen (1988).

More recently, Unni *et al.* (2007) modeled a spherical particle between two parallel plates under a streamwise electric field. The particle streamwise velocity and rotation were determined by decomposing the solution into components that addressed the disturbance in the electric field due to the walls, the disturbance due to the particle, and the potential due to a voltage gradient along the streamwise direction. The disturbance due to the wall was represented as a general Fourier integral solution to the Laplace equation in Cartesian coordinates, while that due to the spherical particle was expressed as the solution to the Laplace equation in spherical coordinates. Their results were also expressed, in Fig. 3 of Unni *et al.* (2007), in terms of the ratio of the particle velocity to that given by the Smoluchowski equation as a function of a / D_C and $D_F / (D_F + D_C)$ where *a* is the particle radius, and D_C and D_F are the distances between the particle center and the closest or farthest walls respectively. As discussed in Chapter 6, considering the size of the

illuminated region, $0.4 < a / D_C < 1$, and $D_C / (D_C + D_F) < 0.02$, so the particle electrophoretic velocity should be enhanced by 23% at most based upon Fig. 3 in Unni *et al.* (2007). This has good agreement with Yariv and Brenner (2003) and Keh and Chen (1988).

Section 2.6: Particle Assemblies

Previous literature describes a broad range of directed assembly using external pressure and voltage gradients which are used to form 1D, 2D and 3D structures from micro and nanoparticles.

The majority of research on directed particle assembly uses electric fields instead of pressure gradients to assemble static structures near, or on, the electrodes. Acharya *et al*. (2006) used 80–150 nm long cadmium sulfide (CdS) nanowires with widths of ~2 nm to form temporary nanorod assemblies with a wurtzite crystal structure in various mediums by applying an electric field of 300–800 V/cm. They claimed that these structures, which were thinner than those in previous literature, could be useful for quantum confinement effects. Winkleman *et al*. (2005) used a patterned gold electrode with an electric potential of up to 20 kV (compared to ground) to assemble 100 nm glass spheres into a 2D grid pattern on nearby PS surfaces without the need for a suspending liquid. They were able to transfer their structure by curing it in PDMS and then moving it to another substrate where the structure was released using methanol. Kretschmer and Fritzsche (2004) created pearl chains with the width of tens or even a single particle that connects two electrodes placed up to 15 μm apart using 30 nm gold nanoparticles and an alternating current (AC) electric

fields of 5–40 mV/cm. They thought that this structure could be comparable with DNA and DNA conjugates.

There are far fewer studies that use pressure differences to assemble particle structures. Scirocco *et al*. (2004) used shear rates of about 30 s^{-1} to form long string-like structures in the flow direction from ~3 μm particles suspended in viscoelastic fluids such as polyisobutylene and polybutene.

A few studies have used a combination of pressure gradient and voltage gradient to manipulate and assemble suspended particles into flowing chain or stream structures. Snoswell *et al*. (2011) observed that continuous chains of particle that were several particles in width of particles aligned with the flow direction were formed when a pressure gradient with an average velocity of 1626 μm/s and an AC electric field of 65 kV/m were applied to a suspension of 1 μm particles at 0.8 vol% suspended in a 2 mM KCl aqueous solution. In this study, a minimum pressure gradient had to be applied at a given electric field to transform what were previously particle clusters into particle streamlines. Serhatliogiu *et al*. (2020) used a combination of a pressure gradient (30–50 mbar) and DC electric field (100–500 V/cm) to form particle chains several particles in width using 6 μm diameter particles suspended at a number density of 10^3/mL in various fluids, including deionized (DI) water.

The topic of this thesis, bands, are particle structures that are similar to those discussed by Snoswell or Serhatliogiu. Visualized in Fig. 1.1, bands are similar to chains of particles that are multiple particles wide. These structures were first observed by Cevheri and Yoda (2014a), who studied radius $a < 500$ nm fluorescent polystyrene (PS) tracers at $\varphi_\infty < 0.5\%$ in counterflow using a combination of TIRF (total internal reflection

fluorescence) and particle tracking velocimetry (PTV). In a subsequent study, Cevheri and Yoda (2014b) reported that the particles were attracted to the wall for "counterflow," when the two flows are in opposite directions and that the particles then assembled into "bands" under certain conditions. These bands had properties that stood out from other studies such as being in a flowing solution, rather than in quiescent solution. The bands, while only a few μm wide were also several cm long.

There are also other groups that have studied band formation. Lochab *et al*. (2019) used a = 100–345 nm PS particles using a combination of a pressure gradient, flow rates O(1 μL/min) and a DC electric field, O(10–100 V/cm), in a composite PDMS-glass microchannel. They observed bands using a confocal microscope and, judging from Fig. 4 or Fig. 7 from their paper, the band thicknesses were around 5 μm. Rossi *et al*. (2019) used astigmatism particle tracking velocimetry instead to study a = 245 nm PS particles under a combination of Poiseuille flow at, near-wall shear rates $O(100\ s^{-1})$, and EOF at $E = O$(10 V/cm), and found that bands were about 6 particle diameters thick or 3 μm.

Section 2.7: Mechanisms Behind Particle/Chain Assembly

Although there are many studies which discuss the use of directed assembly using external pressure and voltage gradients, studies which discuss the mechanisms that govern direct assembly are less common. For pairs of particles, Jennings and Stankiewicz (1990) discussed the attractive and repulsive forces between two particles, summarizing the results from Krasny-Ergen (1936) and Bjerknes *et al*. (1933), and suggested a composite equation for the interaction between two spheres under an electric field, either AC or DC. The particles are attracted to each other in the direction of the field while repulsive when

perpendicular to it, tolerating an angle of up to 50° from the direction of the electric field for an overall attractive force. Jennings and Stankiewicz also discussed the behavior of the band-like structures they experimentally observed, discussing the balance between the particles forming bands or pearl chains, with band-like structures occurring more at higher electric fields.

As for pearl chains and more complex structures, Smallenburg *et al.* (2012) experimentally formed 1D pearl chains in a homogenous electric field and also simulated chain lengths. In the simulation, induced dipole interactions were assumed to be the main source of attraction between the particles in the chains. Prieve *et al*. (2010) discusses mechanisms that describe the aggregation of particles into large 2D arrays although this is beyond the topic of this thesis.

CHAPTER 3
EXPERIMENTAL SETUP AND PROCEDURE

This chapter describes the experimental setup that is used to perform the banding experiments. The components of experiment setup will be discussed in detail in the following order.

1) the microchannel and mounting to the stage;
2) the working fluid in the microchannel;
3) the setup to produce Poiseuille and electroosmotic flow; and
4) the optics used to illuminate the channel with evanescent waves.

This chapter will then detail the three main types of experimental procedures.

Section 3.1: The Microchannel

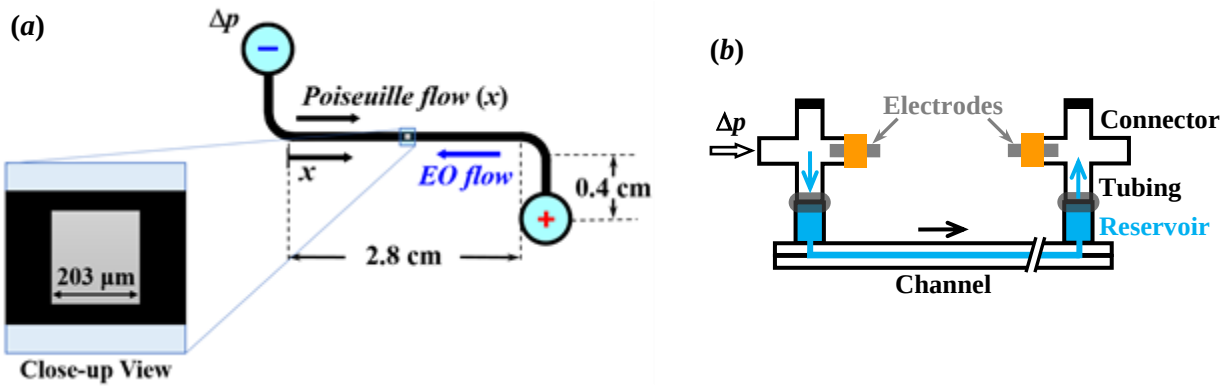

Figure 3.1: Microchannel overview (*a*) Bottom view of the microchannel. The imaged region (gray square) is the center of the straight portion of the channel. The pressure difference ΔP applied from the upstream (left) to downstream (right) reservoirs drives Poiseuille flow to the right, while the electric field applied from the left to the right reservoirs drives the counterions (here, cations) to the left. (*b*) Side view of the channel showing the four-way connectors and channel reservoirs used to apply the pressure gradient and electric field. Black and blue arrows indicate the directions of Poiseuille and EO flows, respectively; the *x*-direction is taken to be that of the Poiseuille flow.

The experimental microchannels consist of an "upside-down" channel trench isotopically wet etched into a 2.3 mm-thick fused silica substrate (Telic Corp) which is sealed at the bottom using a 1 mm thick fused-quartz microscope slide "lid" (Esco Optics R120110). A 1 mm hole drilled through the fused quartz substrate over each end of the channel path leads to a cylindrical Pyrex reservoir with an inner diameter of 3.2 mm, an outer diameter of 6.4 mm, and an axial extent of about 12.7 mm.

The microchannels, with the exception of the Pyrex reservoirs, were fabricated by J. P. Alarie in the research group of J. M. Ramsey at the University of North Carolina at Chapel Hill. The channel trench was patterned into a 101 mm square × 2.3 mm thick fused quartz substrate using a wet-etching technique. The wet-etching technique begins by covering the entire substrate surface with gold, then transferring the channel pattern via an e-beam photomask and UV light, followed by photoresist. The exposed portion of the gold was etched using a potassium iodide/iodine etchant bath (KI/I_2) and the channel pattern was etched into the substrate using a dilute hydrofluoric acid/ammonium fluoride etchant bath (HF/NH_4F) bath at 50 °C. After dicing the patterned substrate into individual open channels, each open channel was then thermally bonded with a 1 mm thick fused silica "lid" at 1100 °C for 5 h. Holes 1 mm in diameter were ultrasonically drilled at both ends of the microchannel through the 2.3 mm-thick fused quartz substrate. After receiving these microchannels from J. P. Alarie, the cylindrical Pyrex reservoirs were attached over each hole with epoxy (Loctite E-60HP) cured for 24 h at 50 °C using the procedure described in Appendix A.3.

The channel path is S-shaped as shown in Fig. 3.1*a*; the total length of the channel and that of its long central straight portion is determined by imaging portions of the channel

using the built-in Bertrand lens of the microscope. As described in Appendix B.2, a total of six images were usually required to cover the entire channel and were combined together to form a composite image of the entire channel. The total length of the channel, defined to be the distance along the channel path from the bottom centers of the inlet and outlet reservoirs, L = 4.2 cm. The length of the central straight section L_S = 2.8 cm.

The coordinate system for the long straight portion of the channel is defined as follows: x is along the Poiseuille flow (*i.e.*, streamwise) direction, measured from the inlet of this portion of the channel; y is the cross-stream direction and parallel to the bottom wall of the channel, measured from the channel centerline; and z is the wall-normal direction and is 0 at the bottom wall. Since all experiments discussed in this thesis take place in the central straight section, $x \leq 2.8$ cm.

Since the wet chemical etch is isotropic, the resulting channel has a roughly trapezoidal cross-section. The dimensions of the etched channel trench were measured using a profilometer; the channel depth (z-dimension) $H \approx 34.1$ μm, the width (y-dimension) at the bottom of the channel ($z = 0$) $W_b \approx 260$ μm, and the width at the top of the channel ($z = H$) $W_t \approx 360$ μm. The hydraulic diameter, D_h, is then estimated to be about 60 μm using the following equation:

$$D_h \equiv \frac{4A}{P} = \frac{4\left(\frac{W_t + W_b}{2}\right)H}{W_t + W_b + 2\sqrt{\left(\frac{W_t - W_b}{2}\right)^2 + H^2}} \qquad [3.1]$$

where A is the cross-sectional area, and P is the perimeter of the cross-section.

The channel zeta-potential ζ_w is also determined using an electroosmotic (EO) flow current monitoring technique (Sze *et al.* 2003). By determining the amount of time

required to replace 1.1 mM sodium tetraborate ($Na_2B_4O_7$) solution with 0.9 mM $Na_2B_4O_7$ solution using EO flow, the electroosmotic mobility, and thus ζ_w, can be determined. These concentrations were chosen because they "bracket" the 1.0 mM $Na_2B_4O_7$ solution used in most of the experiments and the procedure is described in Appendix A.4. Using this technique, $\zeta_w = -110$ mV ± 5 mV.

The channel is mounted on an inverted epifluorescent microscope (Leica DM IRE2) stage and viewed from below through the "lid." The channel is mounted to the microchannel stage using clips attached to the stage that clamp the top of the microchannel substrate. As explained further in Sec. 3.4, the channel is illuminated from underneath with evanescent waves to visualize only the particles in the channel within roughly 0.5 μm from the surface of the "lid". The flow in the long central straight section was imaged over a physical field of view 203 μm square in the center of the channel (*i.e.*, equidistant from the channel side walls) centered at a specified x. The 203 μm square region is called the region of interest. For all experiments, $x \geq 6$ mm so that the imaged region is at least $100D_h$ downstream of the bend to ensure fully developed flow.

Section 3.2: Experimental Solutions

The experimental solutions are dilute suspensions of fluorescent microparticles. They are generated shortly before each experiment by mixing a 1 mM $Na_2B_4O_7$ stock solution with a concentrated particle solution, where concentrated particle solutions are purchased from a vendor.

The stock solution is an aqueous 1 mM $Na_2B_4O_7$ solution (pH~ 9) made by dissolving sodium tetraborate decahydrate salt ($Na_2B_4O_7 \cdot 10H_2O$) (Alfa Aesar 40114, Lot

R24C036), or borax, in UltraPure water. A detailed procedure for generating the 1 mM $Na_2B_4O_7$ solution is described in Appendix A.1. The deionized (DI) UltraPure grade water is obtained from the Marcus Organic Cleanroom at the Georgia Tech Institute for Electronics and Nanotechnology (IEN), and prepared by deionizing water to a resistivity of 18.2 MΩ/cm, passing the deionized water through UV lamps to destroy total organic carbon, degassing the water using membrane filters and adding nitrogen as required to keep the water from reabsorbing any gasses from the surroundings, and finally filtering the water to remove particulates. The pH of the stock solution is measured by a pH meter (Oakton pH11 Economy Meter) after calibration with purchased pH 4, 7, and 11 buffer solutions. After preparation, the stock solution is stored up to a month in a refrigerator.

The fluorescent polystyrene (PS) particles are commercially available as a 2 vol% particle solution. The particle properties specified in these studies are the average particle radius, *a*, particle fluorescence properties such as the emission and excitation maxima, and particle zeta potential, ζ_p. The mean and standard deviation of *a* are given by the manufacturer, while ζ_p must be measured. In all cases, ζ_p is measured for particles suspended at a volume fraction of 0.02% in 1 mM $Na_2B_4O_7$ by dynamic light scattering using a Malvern ZetaSizer ZS available in the Marcus Organic Cleanroom at the IEN.

The particles are nearly density matched to the aqueous solution, where the solution density ρ_s=0.998 g/cm^3 is similar to that of solid PS, ρ_p=1.005 g/cm^3. These particles stay in suspension over experimental run times up to 8 h. Three different spherical PS particles are used for these studies: (1) a = 245 nm carboxylate-modified PS spheres labeled with a green fluorescent dye with excitation and emission peaks at wavelengths λ = 505 nm and 515 nm, respectively (ThermoFisher F8813); (2) a = 250 nm PS spheres labeled with a red

fluorescent dye with excitation and emission peaks at 525 nm and 565 nm, respectively (Polysciences 19507-5); and a = 245 nm carboxylate-modified PS spheres labeled with a red fluorescent dye with excitation and emission peaks at 580 nm and 615 nm, respectively (ThermoFisher F8812). A list of particle solutions and their properties is given below in Tbl. 3.1. Note that after a long period of time, about 1–2 years, the particle zeta potential of fresh ThermoFisher F8813 changed significantly from –42 mV to = –55 mV. A query was sent asking for the reason for this change, but no conclusive answer was found.

Table 3.1: List of Particle Solutions

#	Particles	Background Electrolyte	Maximum Emission /Excitation λ [nm]	a [nm]	ζ_p [mV]
1	ThermoFisher F8813	1 mM Sodium Tetraborate	505/515	245	–42
2	Polysciences 19507-5	1 mM Sodium Tetraborate	525/565	250	–77
3	ThermoFisher F8813	1 mM Sodium Tetraborate	505/515	245	–55
4	ThermoFisher F8812	1 mM Sodium Tetraborate	580/615	245	–60

The particle solutions mentioned in Tbl. 3.1 are either used individually or combined to perform three main types of experiments. An experiment using a homogeneous solution uses only particle solution 1 and is used to study band properties, discussed in Chapter 5. A two-color experiment, which only visualizes tracer particles that are a small fraction of a binary mixture of similar bulk and tracer particles, uses a combination of particle solutions 3 and 4. This experiment is used to study particle counts and dynamics discussed in Chapter 6. Lastly, a heterogeneous experiment, which is meant to observe the behavior of a mixture of two particles with different ζ_p, uses particle solutions 1 and 2. This type of experiment is discussed in Appendix E.

The particle concentration in the experimental solution is specified in terms of its bulk volume particle fraction φ_∞. To prepare an experimental solution with a final volume of $\forall_\infty$ and particle fraction φ_∞, Eq. 3.2 is used to determine the volume of the 2 vol% particle solution that should be added to the aqueous solution, $\forall_b$:

$$\forall_b = \frac{4\pi a^3 c_b \forall_\infty}{3\varphi_\infty} \qquad [3.2]$$

where c_b is the number density of particles in the 2 vol% solution.

The following procedure is used to prepare an experimental particle solution

1. A volume $\forall_b$ of 2 vol% particle solution is dispensed into a glass vial with a pipette
2. An appropriate amount of stock 1 mM $Na_2B_4O_7$ solution is added to the glass vial with a pipette to increase the total volume to $\forall_\infty$
3. The solution is sonicated for 10 min to break up particle aggregates
4. The solution is filtered using a syringe filter (Millex SLAA033SS) with a pore size of 700 nm to remove remaining aggregates and placed into a new glass vial
5. The solution is degassed at 0.93 ± 0.2 bar for 10 min

For two-color experiments with a total particle volume fraction of φ_∞, the ratio of tracer particles to bulk particles is at most 1%; this fraction was the highest concentration of tracer particles that allowed detection of individual tracer particles.

Section 3.3: Generating Poiseuille and Electroosmotic Flow

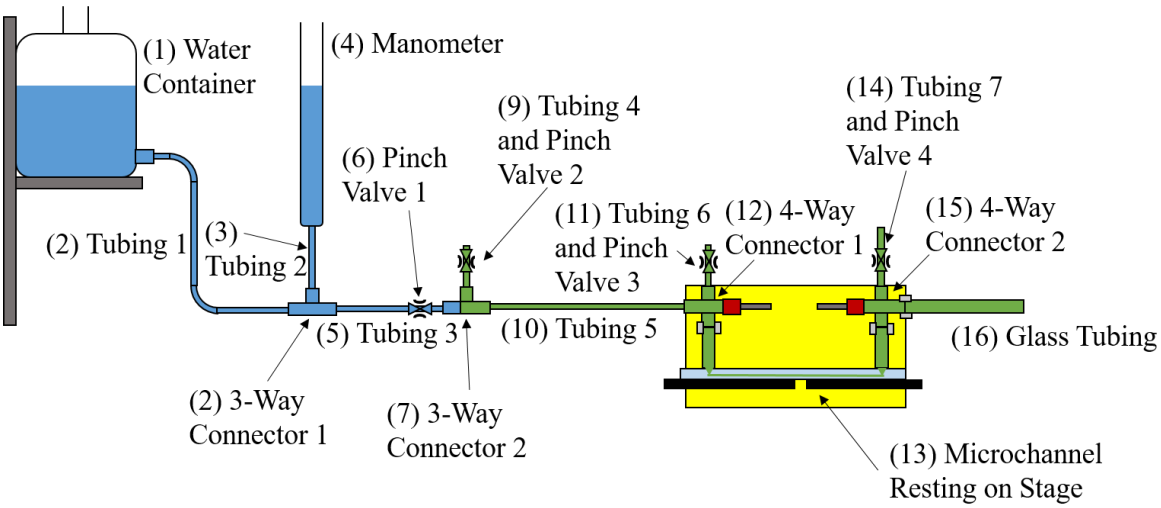

Figure 3.2: Overall tubing setup. The green components are filled with experimental particle solution at the beginning of the experiment while the blue components are filled with DI water.

The particles only assemble into bands in a combination of steady Poiseuille and electroosmotic (EO) counterflow driven by an external pressure gradient and a DC voltage gradient, or electric field, respectively; "counterflow" here denotes that the Poiseuille and EO flows are in opposite directions, or along the $+x$ and $-x$ directions, respectively. The pressure gradient, which is to the left (*i.e.*, along the $-x$ direction), is generated hydrostatically by connecting the upstream four-way connector (component (12) in Fig. 3.2) to a water container at an adjustable height (1) and the downstream connector to a long piece of glass tubing (16) which is open to the surroundings. A manometer is used to measure the applied pressure difference ΔP. The ambient temperature (typically 21 °C) is measured by a thermometer and used to estimate the properties of the fluid, which are assumed to be those of water.

As shown in Fig. 3.2, these components are connected with PVC plastic tubing, three-way connectors, and four-way connectors with an inner diameter of 3.4 mm and an

outer diameter of about 6.4 mm. Although the three-way connectors and four-way connectors are barbed and can interface directly with the plastic tubing, components like the outlet four-way connector and the glass tubing must be connected using flexible Tygon tubing with an inner diameter of 4.8 mm and an outer diameter of 7.9 mm (indicated in grey in Fig. 3.2). Although the inner diameter of this tubing is lower than the outer diameters of the two connected pieces of tubing, it is flexible enough to form a connection without leakage at the pressures used in these experiments.

Since only the near-wall region of the channel is illuminated which will be described in further detail in Sec. 3.4, a near-wall shear rate $\dot{\gamma}_w$ is defined in the illuminated region using the exact solution for laminar Poiseuille flow in Eq. 2.10. Within the region illuminated by the evanescent waves, *i.e.*, $z \leq 0.5$ μm, $\dot{\gamma}$ varies by at most 4% from the value at $z = 0$. In all cases, $\dot{\gamma}_w < 2000\ s^{-1}$.

As seen in Fig. 3.1*b*, the voltage difference ΔV is generated by a DC power supply (Stanford Research Systems PS325; Instek GPR-3510 HD) connected to platinum electrodes inserted through a hole in the end of a rubber sleeve over one of the ports of both four-way connectors. The electric field magnitude $E = \Delta V / L$; in all cases $E < 500$ V/cm. The application of an electric field may heat the solution during experiments in what is known as joule heating. This was found to be negligible and discussed in Appendix G.

Section 3.4: Visualizing Particles or Bands in Counterflow

To visualize the fluorescent particles, the microchannel is illuminated with pulses of light whenever possible to minimize photobleaching the fluorescent particles or heating

of the working fluid. Fig. 3.3 shows a schematic of the illumination setup which is mounted upon, and vibration isolated by, an optical table (TMC 63-553). The illumination source is the wavelength λ = 488 or 514 nm beam from a continuous-wave (CW) argon-ion laser (Innova I305) with an output power of about 2 W. The laser beam is diffracted by the Bragg grating formed by an acousto-optic modulator (AOM) (IntraAction Corp AFM-803A1) driven by a function generator. The AOM is turned "on" by a function generator, which delivers a square wave with an amplitude of 5 V and pulse width of 0.5 ms at a frequency of 10 Hz. When turned "on," the AOM diffracts the laser beam to create 0.5 ms wide pulses at 10 Hz. These pulses are spatially filtered by an iris (6) and elevated by the beam steerer consisting of Mirrors 1 (4) and 2 (5). An optional fused silica flat (7) redirects a small portion of the beam (~8%) onto a laser power meter (Coherent Lasermate Q) (8) as required to monitor the laser power. The focusing lens (9) then focuses the beam to an ellipse with a minimum dimension of about 0.5 mm when it illuminates the microchannel.

The path of the laser beam is then adjusted to undergo total internal reflection at the imaged region. The adjustable Mirror 3 (10) redirects the beam onto Prism 1 (11) which lies on top of, and is coupled to, the microchannel with immersion fluid (Cargille Laboratories 16242) with an index of refraction of 1.5232 (at λ = 486.1 nm). The beam, after being refracted by Prism 1, is guided by the fused-quartz channel, which serves as a waveguide because the angle of incidence of the beam exceeds the critical angle (for a quartz-air interface) of θ_c = 65.6°. The beam finally undergoes total internal reflection (TIR) at the fused quartz-water interface within the microchannel at an angle of incidence $\theta_i \approx 70°$. The TIR at the refractive-index interface between the fused quartz "lid" and the

working fluid generates evanescent waves that illuminate the fluid and hence the flow within the microchannel. The value of θ_i is determined from the distance between two adjacent TIR reflections and the 1 mm thickness of the lid.

The evanescent waves have an intensity that decays exponentially in *z*, and the length scale for this decay, the intensity-based penetration depth z_p, is estimated to be 110 nm based on Eq. 3.3 using where λ is the laser wavelength, the index of refraction for the solution is n_2 and the index of refraction for the fused silica lid is n_1.

$$z_p = \frac{\lambda}{4\pi\sqrt{n_1 \sin\left(\theta_i\right)^2 - n_2^2}} \qquad [3.3]$$

The determination of z_p is also described in Appendix B.3.

The exponential decay of evanescent wave illumination is expressed in Eq. 3.4:

$$I = I_0 \exp\{-z / z_p\} \qquad [3.4]$$

where the evanescent wave intensity is I and I_0 denotes the illumination intensity at the reflected surface.

The beam is then guided by the microchannel until it reaches Prism 2 (14), which is also coupled to the microchannel with immersion fluid, and couples the beam out of the channel and guides it away from the microchannel, preventing further illumination.

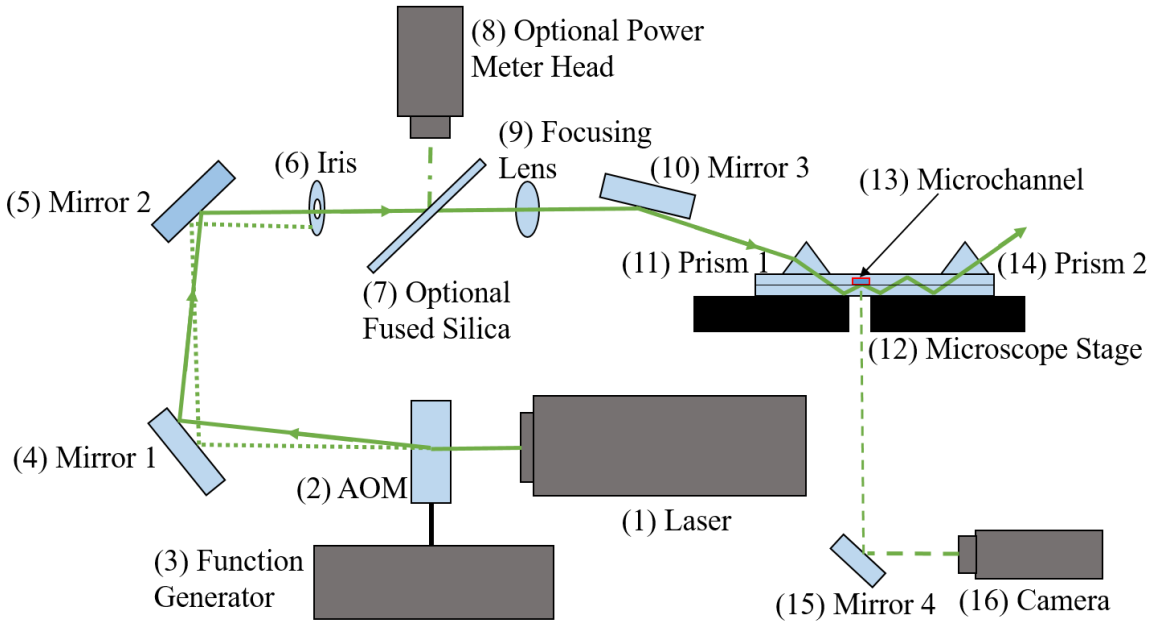

Figure 3.3: Overall illumination setup. The solid green line represents the path of a laser pulse meant to illuminate the microchannel. The dotted green represents the path of the laser for the remaining duration where the path ends on the iris. The dash-dotted line represents the reflected light split from the laser pulse which is measured by the power meter head. The dashed line represents the illumination from the imaged region which is recorded by the camera.

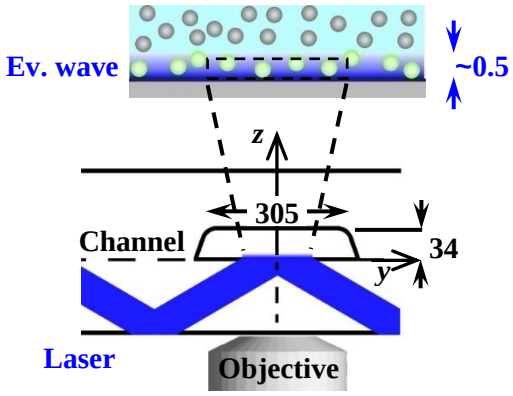

Figure 3.4: Cross-section of the microchannel showing fluorescent particles illuminated by evanescent waves. Evanescent wave illumination occurs at the interface between the fused silica "lid" and the solution flowing through the channel. Dimensions are given in μm.

The fluorescence from the particles is imaged through a microscope objective and excitation filter and recorded by a camera, which are all mounted on the microscope. The objective is a magnification $M = 40$, numerical aperture $NA = 0.55$ objective

(Leica 506059) which images a 203 μm square field of view as described in Appendix B.1. The excitation filter, which depends on the choice of particle (Tbl. 3.2), is chosen to transmit the longer wavelength fluorescence from the particles while blocking the shorter wavelength illumination (*i.e.*, excitation). All the filters were installed in the fluorescence module of the microscope which lies between the microscope stage and the camera.

Table 3.2: List of Bandpass Excitation Filters

#	Transmitted Wavelengths [nm]
1	525±25
2	530±10
3	620±10

Two different digital cameras, an electron multiplying charge-coupled device (EM-CCD) camera (Hamamatsu C9100-13) with very high sensitivity that records images at a slow frame rate, and a complementary metal oxide semiconductor (CMOS) camera (Photron FASTCAM SA4) that records images at a high frame rate, are used in these studies. For the most part, the EM-CCD camera, which records a sequence of 512 × 512 pixels 16-bit images at 10 Hz and is synchronized with the AOM, was used to visualize the particle dynamics and assembly. The CMOS camera, which records a sequence of 640 × 640 pixel 16-bit images at 500 Hz, was used to estimate particle velocities.

Section 3.5: Experimental Procedures

This section details the procedure for the three different types of experiments in this thesis. For every experiment, the setup is prepared and calibrated in the same way to promote consistency. The numbers in procedures refer to those in Fig. 3.2. The protocol for this setup preparation is as follows:

1. The various parts of the setup are cleaned. Tubing components (10)–(12) and (14)–(16) are disassembled, rinsed with DI water, methanol, and DI water in that order, then dried with compressed air. The channel is rinsed instead with a sequence of DI water, methanol, acetone, DI water, 1 mM sodium hydroxide (NaOH), DI water, then working fluid in that order, where 1 mL of each solution is driven through the channel by applying vacuum to the downstream reservoir and filling the upstream reservoir with fluid. Note that tubing components (10)–(16) are disassembled during this step.
2. The experimental solution is prepared as described in Sec. 3.2.
3. The setup is assembled with the exception of the electrodes, and the channel and tubing are filled with the solutions shown in Fig. 3.2 using the following procedure:
    a. Begin with all pinch valves closed.
    b. Fill (1)–(4) with DI water by closing Pinch Valve 1 and filling the Water Container with DI water until the free surface of the DI water in the Water Container is the same height as the free surface in the Manometer.
    c. Fill tubing (5)–(9) with DI water by opening Pinch valves 1 and 2 and placing the open end of Tubing 4 underneath the free surface of the Water Container, which allows DI water to flow out of (9).
    d. Close Pinch Valve 1.
    e. Open Pinch Valves 3 and 4 and connect a syringe filled with the particle solution to (11).
    f. Push the particle solution through Tubing 6 by pressing down on the syringe plunger until (9) is filled.

g. Close Pinch Valve 2.

h. Push the solution through Tubing 6 until by pressing down on the syringe plunger until (14) is filled; the channel must be tilted slightly so that the end of (16) is elevated above the end of (14).

i. Close Pinch Valve 4.

j. Push solution through until about 3 cm of (16) is filled.

k. Using a needle and syringe, draw all air from the two stoppers.

4. Place the electrodes through the sleeve stoppers and clean the surface of the microchannel with methanol and lens paper.
5. Mount the channel onto the stage by placing the clips attached to the stage over the channel. Place immersion fluid on the microchannel and then place the prisms on top of the immersion fluid.
6. Adjust the stage position and angle so the objective is focused on the desired region of interest of the channel and the channel (*x*-)axis is aligned with the camera.
7. Turn on the laser, AOM, and function generator. Adjust the function generator to product 0.5 ms long pulses at 5 V and 10 Hz to drive the AOM. Align Mirror 3 so that the laser beam undergoes TIR at the desired portion of the channel.
8. Switch to the Bertrand lens on the microscope and remove the objective. Record an image of two adjacent TIR positions to determine θ_i.

From this point, the procedure depends on what type of data needs to be collected. The following procedure is for an experiment with a single type of particle to estimate the minimum E required for bands to occur at a given shear rate E_{min}, the time for the first band to form T_o, and the number of observed bands in the region of interest N which are

described further in Chapter 4. The Hamamatsu EM-CCD camera and Filter 1 in Tbl. 3.2 are used for this experiment.

1. Estimate E_{min} for a constant $\dot{\gamma}_w$ for every $\dot{\gamma}_w$ that will be examined during the experiment. The procedure for this is as follows:
    a. Start the Poiseuille flow and wait for 5 min to ensure that $\dot{\gamma}_w$ is constant.
    b. Apply the desired E for another 5 min. At this time, the bands should exhibit steady-state behavior.
    c. Record 1000 frames (over 100 s) with the camera at 10 Hz.
    d. Turn off the electric field.
    e. Process recorded frames as discussed in Sec. 4.2 to determine if bands have formed
    f. Repeat steps a-e for another value of E, varying E in increments of 5 V/cm. Take E_{min} to be the average of the highest E where bands do not form and the lowest E where bands form as described in Sec. 4.3.
2. Record data at accumulation stage and steady-state to estimate T_o and N, respectively. Repeat for every ($\dot{\gamma}_w$, E) of interest for the experiment as follows:
    a. Let the solution settle at a constant $\dot{\gamma}_w$ for 5 min.
    b. To collect particle velocities during the accumulation stage, continue to steps c and d. Otherwise, apply the desired E and skip to step e.

c. Record images for 160 s at 10 Hz. Turn on the electric field and adjust to the desired value of E for 10 s after turning on the electric field. These images will be processed later in MATLAB to determine T_o.

d. To estimate N, continue to steps e and f. Otherwise, skip to step g.

e. Wait until steady-state occurs, which is > 5 min in all cases.

f. Record 1510 frames at 10 Hz. This data will be processed later in MATLAB to determine N.

g. Turn off the electric field.

The following procedure is for a two-color experiment to estimate E_{min}, T_o, and the number of tracer particles during the accumulation stage. The Hamamatsu EM-CCD camera and Filters 1 and 2 in Tbl. 3.2 are used for this experiment.

1. Estimate E_{min} for a constant $\dot{\gamma}_w$ for every $\dot{\gamma}_w$ of interest. The procedure is the same for the homogenous experiment and uses Filter 1.
2. Record data at accumulation stage to estimate T_o. This is done for every ($\dot{\gamma}_w$, E) combination for that experiment. The procedure is the same for the homogenous experiment and uses Filter 1.
3. Record data at accumulation stage to estimate the number of tracer particles. This is done for every ($\dot{\gamma}_w$, E) combination of interest. The procedure is the same for the homogenous experiment except that it uses Filter 2.

The following procedure is for a two-color experiment to estimate E_{min}, T_o, and particle velocities during the accumulation and steady-state stages. The CMOS camera and Filters 1 and 2 in Tbl 3.2 are used for this experiment. The illumination for this

experiment is continuous, *vs.* pulsed, because of the relatively weak signal from the tracer particles.

1. Estimate E_{min} for a constant $\dot{\gamma}_w$ for every $\dot{\gamma}_w$ of interest. The procedure is the same for the homogenous experiment and uses Filter 1.
2. Record data during accumulation stage to estimate T_o. This is done for every ($\dot{\gamma}_w$, E) combination of interest. The procedure is the same for the homogenous experiment and uses Filter 1. Estimate T_o.
3. Record data during the accumulation and steady-state stages to estimate particle velocities at steady-state for every ($\dot{\gamma}_w$, E) combination of interest. The procedure uses Filter 2 and is as follows:
    a. Let the solution settle at a constant $\dot{\gamma}_w$ for 5 min.
    b. Turn on the electric field.
    c. Continue to steps d and e to collect particle velocities during the accumulation stage. Otherwise, skip to step f.
    d. Record images at 500 Hz starting 10 s before, and ending 10 s after, the expected T_o. These data will be later processed in MATLAB to determine particle velocities during the accumulation stage.
    e. To collect particle velocities during the steady-state stage, continue to steps f and g. Otherwise, skip to step h.
    f. Wait until steady-state occurs, at least 5 min in all cases.
    g. Record images at 500 Hz for 20 s. These data will be processed later in MATLAB to determine particle velocities during the steady-state stage.

h. Turn off the electric field.

i. Repeat the procedure for another ($\dot{\gamma}_w$, E) combination.

After each experiment, the tubing and channel are cleaned as follows:

1. The various parts of the setup are cleaned. Tubing components (10)–(12) and (14)–(16) are disassembled, rinsed with DI water, methanol, DI water in that order, then dried with compressed air.
2. Disassemble tubing components (10)–(16), then clean the channel with DI water, methanol, acetone, and DI water in that order, where 1 mL of each solution is driven through the channel by applying vacuum to the downstream reservoir and filling the upstream reservoir with fluid.

CHAPTER 4
IMAGE PROCESSING

This section describes how band characteristics are extracted from the experimental image sequences and motivates the choice of band characteristics. As explained in Chapter 3, all the experimental data in this thesis are comprised of grayscale images of fluorescent particles near the channel wall which are illuminated with evanescent waves. The experiments usually start with Poiseuille flow at a fixed pressure gradient (*i.e.*, no electric field), and band formation is observed after the DC electric field is turned on. In this chapter, an overview of the characteristics of band formation is given, followed by the methods used to determine several characteristics of this process.

Section 4.1: Band Formation Overview

Fig. 4.1 illustrates a typical band formation sequence using 80 μm square images from a single image sequence acquired at an offset electric field ΔE = 4.7 V/cm, where $\Delta E = E - E_{\min}$, $\dot{\gamma}_w = 1390\ s^{-1}$, and $\varphi_\infty = 1.7\times10^{-3}$ at x = 14.1 mm. After the offset electric field is applied (*i.e.*, turned on) at t = 0, the number of near-wall particles increases, with what appears to be a roughly uniform and random distribution over the field of view, and the individual particle images become brighter with time t for t < 10 s. These evanescent-wave visualizations show that the particles are being attracted to, and accumulate near, the bottom channel wall. For t > 10 s, the number of near-wall particles continues to increase, but the particles begin to assemble into faint, but distinct, structures at discrete y-positions—"bands". The contrast between the bands and background increases—*i.e.*, the average intensity of these bands increases over time while that of the area between the

bands decreases as particles are depleted from this region, for 29.3 s < t < 46.1 s. During this time, the y-positions of the bands change and develop a roughly consistent period (y-spacing), and the y-position and width (y-dimension) of the bands becomes relatively stable.

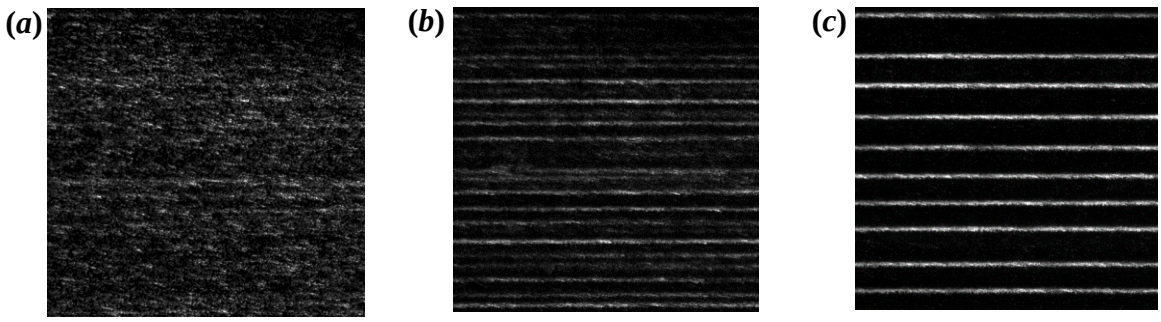

Figure 4.1: Three (contrast enhanced) grayscale images during band formation acquired for a constant near-wall shear rate $\dot{\gamma}_w = 1760\ s^{-1}$ at *a*) times t = 6.15 s; *b*) t = 10.15 s; and *c*) t = 28.15 s after a DC electric field E = 117 V/cm is applied (at t = 0) at x = 14.1 cm. The Poiseuille flow is to the right, while the EO flow is to the left.

Based on these observations, band assembly appears to have three stages:

1) ***accumulation***, where the particles are attracted to and become concentrated near the wall;

2) ***band formation***, where the particles assemble into a relatively large number of fairly unstable bands whose average intensity increases over time; and

3) ***steady-state***, where the band characteristics (average intensity, period) of the bands remain fairly consistent over time.

Section 4.2: Band Detection

To characterize the colloidal structures called bands, these structures have to first be identified, or detected, in these images. This band detection algorithm was developed and implemented in MATLAB (MathWorks ver. R2019b). Since one of the most notable characteristics of a band is the difference in the particle concentration within and between the bands (*i.e.*, the background), bands are identified based on grayscale contrast. The algorithm which detects the number and location of bands is as follows (Fig. 4.2 illustrates this procedure):

1. Since the bands are aligned along the flow (x) direction, the 2D image is reduced to a 1D profile $\bar{I}(y)$ by row-averaging the image by the grayscale value of the pixels which results in a spatially (along x) averaged grayscale profile in y.
2. A global value for the background is estimated through iteration depending upon the type of image as detailed in the next steps. The initial guess for the background is the average of $\bar{I}(y)$, and the iteration continues until the difference between the current guess and any of the previous guesses is less than 1 (in grayscale).
3. For images taken with the Hamamatsu EM-CCD camera, which have significant background noise, each subsequent guess is the average of all values of $\bar{I}(y)$ that exceed a threshold defined to be 1.5 times the previous guess for the background grayscale value.
    a. This threshold was chosen to be 1.5 times the background because for several sample images:

$$1.5\mu_b \approx \mu_b + 2\sigma_b \qquad [4.1]$$

where μ_b and σ_b are the mean and standard deviation of all values of $\bar{I}(y)$ less than the final value of the threshold. Assuming that the background grayscale values follow a Gaussian distribution, this corresponds to the 95% confidence interval.

4. For images taken with the Photron CMOS camera which have very low background noise, however, each subsequent guess is the sum of the average of all values of $\bar{I}(y)$ that exceed the previous guess and a fixed grayscale offset.

5. Adjacent rows (where each row corresponds to a given value of *y*) that are not "background" based on either steps 3 or 4 are defined to comprise a single band. The average *y* value of these rows is then defined to be the (geometric) center of the band.

The output from this algorithm is the total number of bands in the image *N* and the *y*-positions of the geometric centers of these bands.

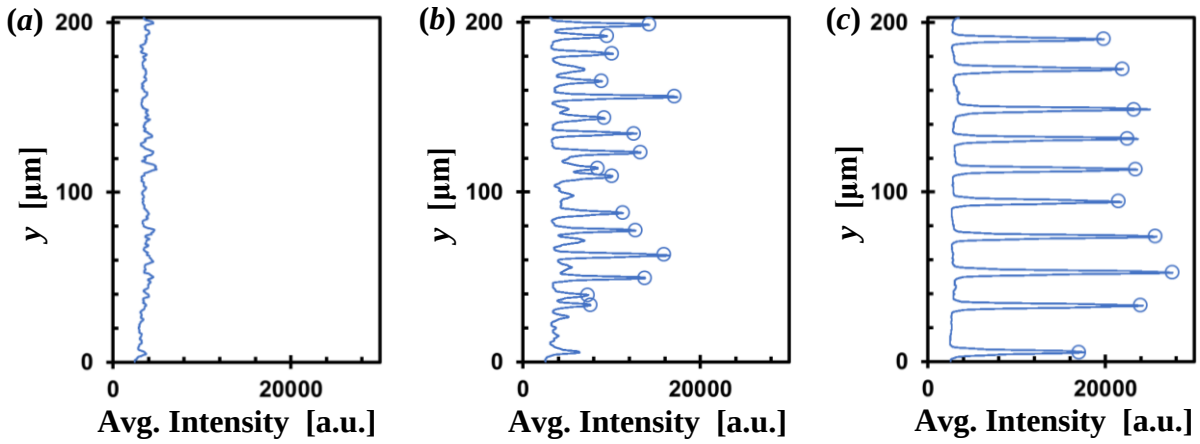

Figure 4.2: Three typical intensity profiles during band formation along the *y*-direction obtained at the same flow conditions and times as those for Fig. 4.1*a*, 4.1*b*, and 4.1*c* at *a*) t = 6.15 s, or T_o – 2 s; *b*) t = 10.15 s, or T_o + 2 s; and *c*) t = 28.15 s, or T_o + 30 s, respectively. The center of each band is denoted by an open circle in *b* and *c*.

A number of useful properties can be drawn from Fig. 4.2. The number of rows that compose each band can be used to estimate the band width. The location of the bands will be used in Chapter 6 to detect particles that are in the bands. The intensity profile can also be used detect regions where there are no bands, which is defined as 6 μm away from the regions designates as bands. This criterion was chosen because the above procedure captures the center of each band but does not cover all rows with increased average intensity over the background. There is a region immediately outside the band locations which is the transition between the bands and the background and the criteria was chosen to avoid this region. The value of 6 μm was chosen since band widths under the conditions $\dot{\gamma}_w$ = 1760 s^{-1}, E = 150 V/cm, φ_∞ = 0.33% were approximately 6 μm.

Section 4.3: Threshold Electric Field Magnitude

Bands are not observed for every case of Poiseuille and EO counterflow. As shown in Fig. 4.3, which is called a "banding map" as described further in Chapter 5, bands are observed to form above a minimum set of flow parameters, namely E and $\dot{\gamma}_w$. Here, E_{min} is defined to be the minimum, or threshold, electric field magnitude where bands form at a given set of (other) parameters (*e.g.* $\dot{\gamma}_w$, φ_∞, x). As shown in Appendix D, E_{min} is perhaps the most important of the band formation parameters because many of the band characteristics scale with the electric field offset, or the magnitude above this threshold $\Delta E \equiv E - E_{min}$, instead of E itself.

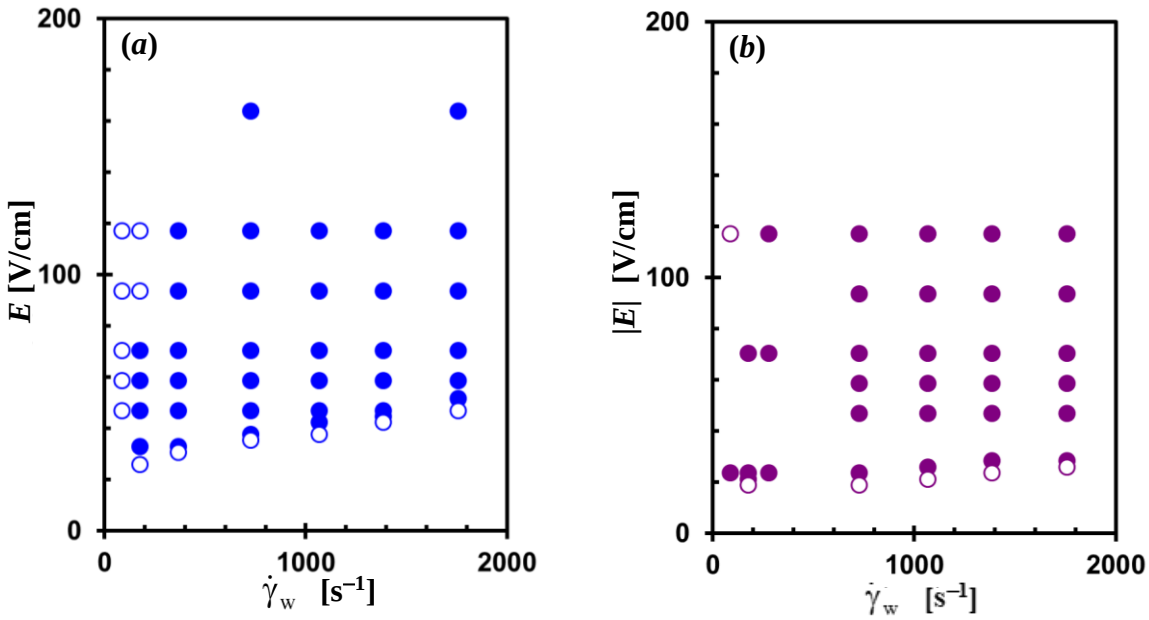

Figure 4.3: Sample banding maps comparing ζ_p = –44 mV and a = 245 nm PS particles in pH 9 $Na_2B_4O_7$ solution at (*a*) φ_∞ = 0.17%; and (*b*) φ_∞ = 0.33%. Bands are observed at the conditions given by the filled symbols; no bands are observed at the conditions where there are open symbols.

To evaluate E_{min}, experimental data are collected to determine the lowest E where bands are detected using the band detection algorithm described in the previous section. To do so, a sequence of images is taken over a range of E values in intervals of 4 V/cm. Since only the steady-state stage is of interest here, a sequence of 1000 frames at 10 Hz are acquired starting at t = 5 min. 1000 frames are collected to ensure that band detection is consistent over time. To ensure that the range of tested E encompasses E_{min}, the range of E should include two cases above an estimated E_{min} where all bands are detected consistently and one case below the same estimated E_{min} where 0–2 bands are detected. Below the estimated E_{min}, 1–2 bands may have formed due to channel surface imperfections such as buildup.

1. To determine E_{min}, bands are detected (or not) using the band detection algorithm for a sequence obtained at a given value of E. If no bands are detected, the

algorithm detects them inconsistently, or if a "band" is suspected to be caused due to channel surface imperfections such as buildup, a new sequence is obtained at the next higher value of E, so at an electric field magnitude incremented by 4 V/cm.

2. This process is repeated until multiple bands are detected at two consecutive values of E, E_L and $E_H > E_L$. The total number of bands over all 1000 images N_L and N_H for the sequences at E_L and E_H, respectively, is then determined.
3. If $N_L \leq N_H - 2$, where the decrease in the number of bands for the lower E is assumed to occur since bands at E_L do not form or are too faint, E_{min} is then taken to be $(E_L + E_H)/2$.
    a. This criterion was chosen because the total number of bands should increase as E decreases, as discussed in Sec. 5.4. At steady-state, the number of bands should fluctuate (due to band migration or merging) by no more than two from the steady-state value. This criterion therefore ensures that there are no issues with the choice of grayscale threshold in the band detection algorithm.

Section 4.4: Time for the First Band to Form

An initial estimate of the time scale for the end of the accumulation stage is useful in analyzing the band characteristics that lead up to that point which in turn may provide valuable clues on what phenomena causes band formation. The time scale T_o is meant to estimate when the bands detected by the algorithm given in Sec. 4.2 begin to form. To determine T_o, a sequence of 1500 images at 10 Hz was acquired starting at $t = 0$ min. Fig. 4.4 shows a typical plot of the number of detected bands N as a function of time during

all three stages of band assembly. Once the algorithm starts to detect bands, N increases rapidly, then decreases somewhat to a "steady-state" value, after which it varies by ± 2 at most. A sigmoid function is curve-fit to $N(t)$ in MATLAB (solid line in Fig. 4.4) using the nlinfit() function in MATLAB, which uses iteration to estimate a combination of parameters that minimizes the sum of the squares of the error between the modeled curve-fit and the data. To ensure that the initial overshoot near T_o does not have a significant effect on the steady-state value, least square regression is performed over a sequence of images over t = [0: T_o + 60 s], or at least 600 frames beyond T_o.

The curve-fit uses the following functional form using three parameters (A_1, A_2, A_3):

$$N(t) = \frac{A_1}{1 + \exp[-A_3(t - A_2)]} \qquad [4.2]$$

The smallest time when N = 1 based on this sigmoid function is then defined to be T_o, so $N(t) = 1$ when $t = T_o$ (denoted by the dashed line in Fig. 4.4).

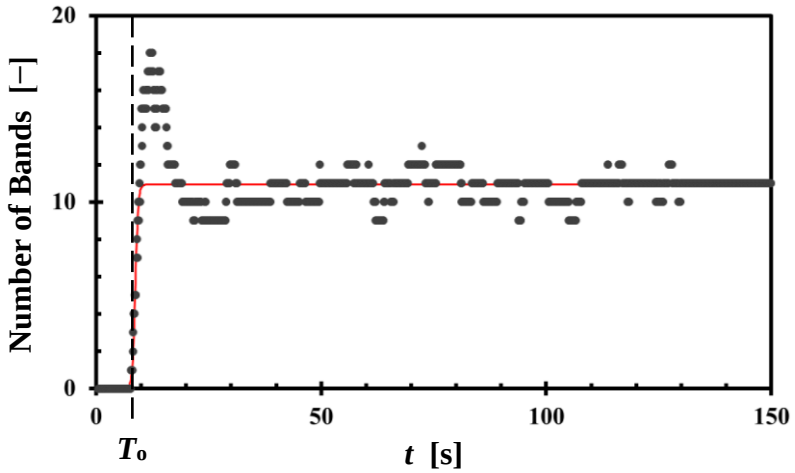

Figure 4.4: Number of bands over time. The red solid line is the sigmoid function curve-fit to these data; the dashed line denotes T_o = 8.15 s, the time when the first band is formed based upon the sigmoid.

Section 4.5: Steady-State Number of Bands

Another band property that is analyzed during this thesis is the steady-state number of bands N_s. While Fig. 4.4 shows that N has a steady-state value with about 1–2 minutes after T_o, which is generally true of the data, and that T_o usually occurs under a minute, the value of N_s is determined using data taken 5 minutes after E is applied. At this time, 1000 images are taken at 10 Hz and N is averaged over these images to determine N_s.

Section 4.6: An Alternative Timescale Based Upon the Image Grayscales

Another time scale for the end of the accumulation stage, T_I, determined directly from the grayscale images, was also considered in this thesis as an alternative to the time scale T_o which was discussed in Sec. 4.4. T_o is determined indirectly using curve-fits with many variables, including those from a sigmoid function fit to the total number of bands which in turn are detected by an algorithm from a sequence of grayscale images based on threshold values. Hence, T_I is a time scale that can be determined more rapidly in a direct fashion.

T_I is determined from the change in the standard deviation in normalized image grayscales, or brightness, $\bar{\sigma}_G$, over time. Fig. 4.1, which shows several images over time during the accumulation stage of banding, suggests that the overall "brightness" of the image, *i.e.*, its spatially averaged grayscale G, increases over time during the accumulation and the band formation stages. The figure also suggests that overall contrast of the image, which can be characterized by the standard deviation of the grayscales in that particular image (over all the pixels in the image), σ_G, increases over time as the particles accumulate near the wall and assemble into bands with grayscales much greater than that

of the background during the particle accumulation and band formation stages, respectively. Spatially averaging the grayscales reduces the effect of image noise and isolated particles, while providing information over a relatively large portion of the channel. Since the illumination intensity varies over the 203 μm square field of view, decreasing near the edges, only the 80 μm square central region of each image was used to determine G and σ_G :

$$G = \frac{1}{N} \sum_{i=1}^{N} B_i \qquad [4.3]$$

$$\sigma_G = \frac{1}{N-1} \sqrt{\sum_{i=1}^{N} (G - B_i)^2} \qquad [4.4]$$

where N is the total number of pixels in the image and B_i is the grayscale of the i^{th} pixel.

The normalized average grayscale $\bar{G}$ was used instead of G to estimate the overall brightness of the image and the smoothed normalized standard deviation $\bar{\sigma}_G$ was used to estimate the overall contrast. Both G and σ_G were normalized by their respective maximum values within each image sequence (*vs.* each image) using the image processing toolbox in MATLAB (ver. R2019b). Using $\bar{G}$ instead of G should minimize the effect of any variations in incident illumination between different trials. The normalized standard deviation was smoothed three times using locally weighted scatterplot smoothing (LOWESS), a local regression smoothing technique, with the lowess smoothing function in MATLAB (https://www.mathworks.com/help/curvefit/lowess-smoothing.html) to obtain the smoothed normalized standard deviation $\bar{\sigma}_G$. Note that all of the results shown here for $\bar{\sigma}_G$ are the original (*i.e.*, unsmoothed) data. An example of the time evolution of $\bar{G}$ and $\bar{\sigma}_G$ is shown below in Fig. 4.5.

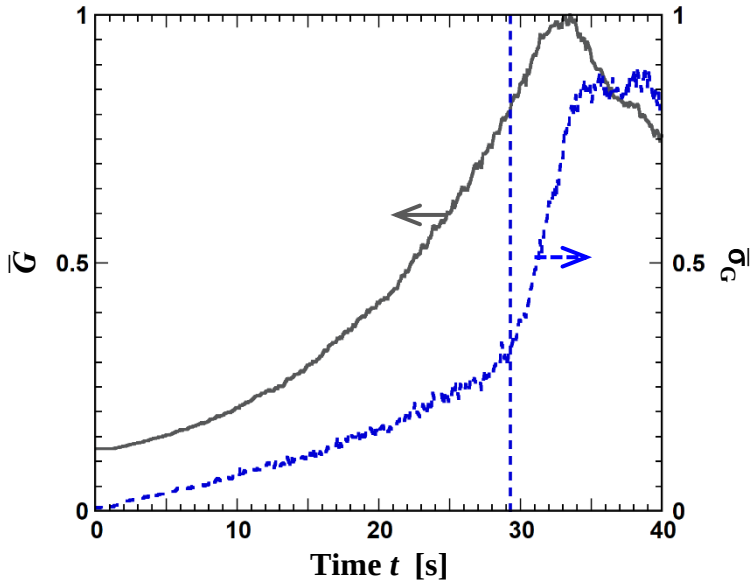

Figure 4.5: The evolution of the normalized image grayscale average $\bar{G}$ (*solid line*) and the normalized image grayscale standard deviation $\bar{\sigma}_G$ (*dashed line*) over time t for the image sequence shown in Fig. 4.1. The vertical line denotes the inflection point in $\bar{\sigma}_G(t)$ at $t = T_I = 29.3$ s.

As expected, both $\bar{G}$ and $\bar{\sigma}_G$ increase with time after the DC electric field is applied at t =0. However, the rate at which $\bar{\sigma}_G$ increases, *i.e.*, $d\bar{\sigma}_G / dt$, has a sharp increase at $t \approx 29.3$ s. The time T_I corresponding to this inflection point in $\bar{\sigma}_G(t)$ is therefore defined to be the timescale that characterizes the end of the accumulation stage. This time also defines the beginning of the band formation stage, when the particles concentrated near the wall with a roughly uniform spatial distribution begin to segregate into distinct structures, namely bands. Thus, the accumulation stage is defined to be over $0 \le t < T_I$, and the band formation stage is assumed to begin at $t = T_I$.

With this observation in mind, T_I is defined as the time at which κ_G ,. The curvature of $\bar{\sigma}_G$:

$$\kappa_G = \frac{\left|\partial^2 \bar{\sigma}_G / \partial t^2\right|}{\left[1+(\partial \bar{\sigma}_G / \partial t)^2\right]^{3/2}} \quad [4.5]$$

is maximum, where the temporal derivatives are calculated by first-order central differencing.

Section 4.7: Particle Count in the Accumulation Stage

The number of near-wall particles is estimated over a sequential set of images taken during the accumulation stage to characterize particle accumulation over time and to determine if a minimum, or threshold, near-wall interparticle spacing is required for the near-wall particles to assemble into bands. To determine how the near-wall number of particles changes over time, a sequence of images, or video, is taken at 10 Hz during the initial stages of banding over the 203 μm square region of interest and processed with MATLAB. This sequence typically starts during "pure" Poiseuille, or constant shear rate, flow a few seconds before the DC electric field is applied. Since the number of particles in the latter part of the accumulation stage for a homogenous particle experiment is too great to distinguish individual particles, particle counts were only determined for two-color experiments. Only the much less concentrated tracer particles are visible in two-color experiments, drastically reducing the number of visible particles in each frame which allows them to be distinguished from one another.

Each individual frame in the video is processed to determine the number of near-wall particles in that frame. This process begins by choosing a threshold grayscale value

to separate the background from the near-wall particles. This threshold value is determined using the signal-to-noise ratio (SNR) which is described in further detail in Sec. 4.8. This threshold value is then subtracted from the grayscale values of all pixels in the image. Groups of adjacent pixels with positive grayscale values are then considered to be a single particle although particles that are determined to be too small (1 pixel) or too large (> 100 pixels) are rejected.

Lastly, an interparticle spacing is estimated from the number of particles N_p. Considering that the maximum possible z-value of the particles ($3z_p \approx 330$ nm) is less than the diameter of an individual particle ($2a = 490$ nm), the visible particles are assumed to consist of at most a single layer. Therefore, the interparticle spacing is taken to be the equivalent diameter D_{eq} where the area of N_p circles of diameter D_{eq} is equal to the area A of the region of interest imaged by the video:

$$D_{eq} = \sqrt{\frac{4A}{\pi N_p}} \qquad [4.6]$$

Section 4.8: Particle Positions

After identifying the particles as described in the previous section, the position of each particle center is determined and later used to determine particle displacements/velocities as described in the next section. The streamwise and cross-stream locations of each particle center (x_p, y_p) is defined to be those of the center of mass or centroid based on pixel brightness (Cheezum *et al.* 2001). In this method, the group of adjacent pixels that compose each particle are determined as described previously, then the

center location is estimated from an average of the particle pixel locations weighted by their grayscale values:

$$x_{\mathrm{p}} = \frac{1}{N}\sum_{i=1}^{N} B_i\, x_i \qquad\qquad y_{\mathrm{p}} = \frac{1}{N}\sum_{i=1}^{N} B_i\, y_i \qquad [4.7]$$

where N is the total number of pixels in the particle image, and B_{i} and (x_i, y_i) are the grayscale value and streamwise and cross-stream location of the i^{th} pixel, respectively.

In addition to locating the particle centers, Cheezum *et al*. expressed a relationship between the sub-pixel accuracy of the center of the particle and a value called the signal-to-noise ratio (SNR):

$$SNR = \frac{I_{\mathrm{o}} - I_{\mathrm{b}}}{\sqrt{(\sigma_{\mathrm{o}})^2 + (\sigma_{\mathrm{b}})^2}} \qquad [4.8]$$

where I_{o} and I_{b} are the average grayscale values of the particle and background, respectively, and σ_{o} and σ_{b} are the standard deviation in grayscale of the particle and background, respectively. This essentially put a limit on the lowest average particle grayscale intensity, or I_{o}, if sub-pixel accuracies of a certain value were desired. A sub-pixel accuracy of around 0.1 was desired for this work which corresponds to a SNR of 8.

To determine an estimate for the SNR, a sample set of images were taken imaging experimental solution but without any particles. This was used to estimate I_{b} and σ_{b} over 1000 images. However, I_{o} and σ_{o} are difficult to determine from particle images since a single particle does not often stay in the illuminated region. Instead, a large fluorescent target was used which was the channel filled with fluorescein. This was acceptable because it is believed that any deviation in the brightness of a particle would not come from the particle intensity, but rather be due to the inconsistency of the incident evanescent wave illumination. One of the fused silica microchannels was filled with a 10 mM disodium

fluorescein solution, illuminated with evanescent waves, and imaged using the same experimental setup as that used in the particle experiments. There was no flow so it is possible that photobleaching became an issue although no noticeable decay was observed during the experiment. The average image grayscale was varied by changing the laser pulse duration and a sequence of 1000 images were taken to estimate I_o and σ_o. Finally, the SNR was evaluated for every I_o and shown in Fig. 4.6.

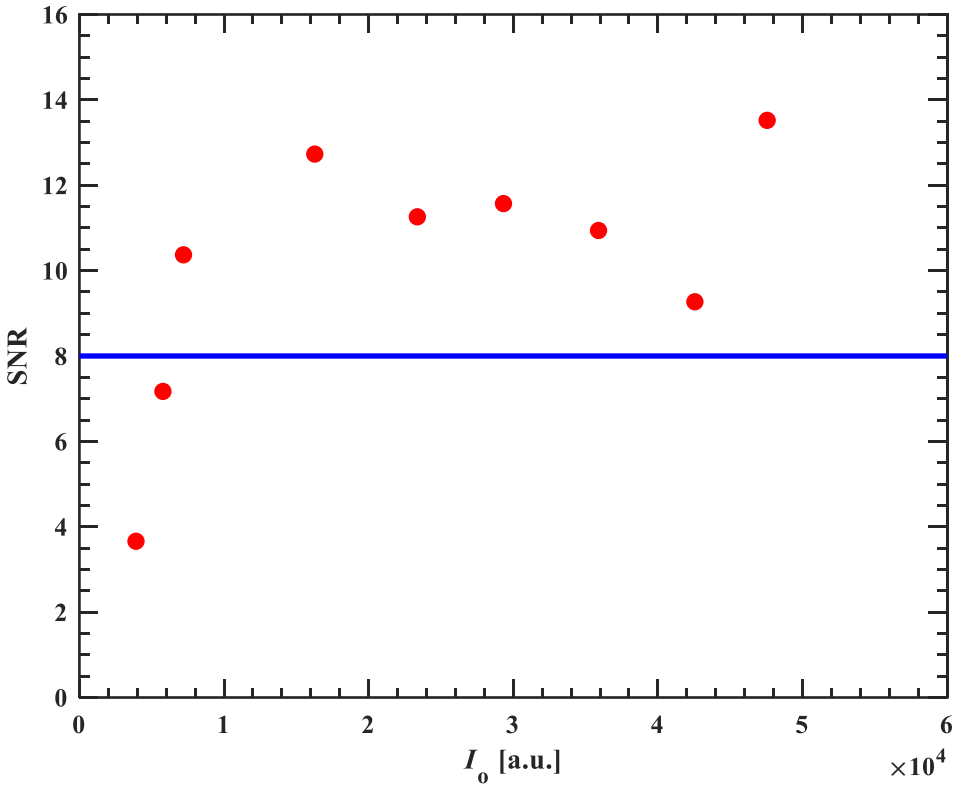

Figure 4.6: *SNR* (Eq. 4.8) *vs.* mean grayscale based on images of a microchannel filled with 10 mM fluorescein solution and illuminated with evanescent waves. The horizontal line denotes the minimum SNR per Cheezum *et al.* (2001) required to determine the location of the particle center with an accuracy of 0.1 pixel.

Fig. 4.6 shows that $SNR > 8$ when $I_o > 6000$ and becomes nearly constant once I_o exceeds 10000. Therefore, $I_o > 6000$ is an appropriate value for the threshold brightness for recognizing particles in Sec. 4.6. However, lower values of threshold brightness may

still be desirable for particle detection, trading particle location accuracy for increased detection at the risk of including more noise. In Fig. 4.6, for $I_o = 4000$, the SNR was about 4. Using Figs. 5*A* and 5*B* from Cheezum *et al*. (2001), which describes a bias and standard deviation respectively in observed particle velocities using the centroid method, a SNR of 4 should have a bias of about 0.2 pixels and a standard deviation of 0.1 pixels. Therefore, the expected sub-pixel accuracy for $I_o = 4000$ is around 0.3 pixels.

The wall-normal position of the particle measured from the channel wall is estimated from the total area brightness of each particle. Since the particles are illuminated by evanescent waves, the total area brightness of the particle A_p:

$$A_p = \sum_{i=1}^{N} B_i \qquad [4.9]$$

where *i* denotes each pixel attributed to that particle. This value should decay exponentially with depth, or *z*-distance from the channel wall:

$$A_p = A_{p0} \exp\{-z / z_p\} \qquad [4.10]$$

where A_{p0} is the area brightness of a particle at the channel wall (*i.e.*, $z = a$) and z_p is the intensity-based penetration depth of the evanescent-wave illumination. Only particles with $z \leq 3z_p$ are considered to minimize the effects of background noise.

Section 4.9: Particle Tracking and Particle Velocities

The particles were tracked to determine their velocities and investigate whether the particles follow the flow assuming that this creeping flow is simply the superposition of simple shear and electroosmotic flows. To determine the displacement of a particle between two successive images, the particles are first identified in both images and their centers are located using the procedure described in the previous sections. The particle

displacement is then simply the difference in the particle center positions within this image pair divided by the time interval between the images. Particles are "matched" between two consecutive images by matching the particle in the second image that is closest, based on a weighted "distance," to the particle in the first image. Since most of the particle motion in this flow is along the streamwise (x) direction, this distance D_h, is weighted along the x-direction, so a particle at (x_1, y_1) is considered to be matched to a particle in the second frame with position (x_2, y_2) when the weighted distance between the two particles:

$$D_h = (x_2 - x_1) - 5(y_2 - y_1)^2 \qquad [4.11]$$

is minimized when comparing the location of any particle in the first images with all particles in the second image. The streamwise particle velocity for a particle, U_p', whose x-position in the first image of the pair at time t_1 is x_1 and whose x-position in the second image of the pair at time t_2 is x_2 is then:

$$U_p' = \frac{\Delta x}{\Delta t} = \frac{x_2 - x_1}{t_2 - t_1} \qquad [4.12]$$

U_p will be denoted as the list of all U_p' over a given time frame or set of image pairs. Given that the uncertainty in individual particle positions is 0.1 pixels as discussed in Sec. 4.8, or about 0.4 μm, and that the time for each image has an uncertainty of 10 μs, the uncertainty of the particle streamwise velocity is 0.011 mm/s.

CHAPTER 5
HOMOGENEOUS PARTICLE SOLUTION RESULTS

The results from several experiments using homogenous particle solutions, as well as the setup and procedure mentioned in Chapters 3 and 4 respectively, are used to study band characteristics, particularly the timescale for the end of the accumulation stage, represented by T_o, and the number of steady-state bands in the region of interest, N_s. These two parameters were determined over a range of electric field E, near-wall shear rate $\dot{\gamma}_w$, particle volume fraction φ_∞, streamwise location x, and particle radius a. The results are also used to test the conjectures discussed in Sec. 1.4. The conjectures addressed in this chapter are:

1. Band formation is caused by interparticle forces between induced dipoles that attract the particles into the band structure. If this is the case, the particles must be close enough together for these forces to be significant. This can be tested by determining if parameter changes that would increase in the number of near-wall particles causes bands to form more often over a set range of E and $\dot{\gamma}_w$ or more quickly which is determined through comparisons of T_o.
2. The wall-normal force predicted by the results of Choudhary *et al.* (2019; 2021) and Khair and Kabarowski (2020) is the major cause for particle migration towards the channel wall during the accumulation stage. Since this force, described in Sec. 2.2.3 and Eq. 2.5, increases as E or $\dot{\gamma}_w$ increases, it should also lead to faster band formation. This force should also increase with more negative ζ_p, also leading to faster band formation.

3. Band formation is convective which will be tested by determining if T_o scales with *dP/dx* or alternatively, with $\dot{\gamma}_w$.

Much of the data described in this chapter is the average of 3–4 separate trials and it was found that there was better agreement between multiple trials if the data was plotted against $\Delta E = E - E_{min}$ =rather than E. This is described in further detail in Appendix D.

Section 5.1: Banding Maps

The assembly of suspended particles into bands in Poiseuille and EO counterflow inside a microchannel depends on numerous parameters, including flow parameters such as E and $\dot{\gamma}_w$, solution properties such as a, φ_∞ and ζ_p and the streamwise location measured from the entrance of the straight portion of the microchannel x. In this section, the different combinations of (E, $\dot{\gamma}_w$) where bands are observed are presented in a "banding map" to visualize and discuss how each of these factors contributes to band formation. The influence of x is discussed in the following section.

A banding map is a 2D plot, in the E- $\dot{\gamma}_w$ parameter space, that shows where bands form for different combinations of these two parameters. Combinations of Poiseuille and EO counterflow (E, $\dot{\gamma}_w$) where bands form are shown as points denoted by closed symbols in this parameter space, while combinations where bands are not observed are shown as points denoted by open symbols. Each point shown is based on three independent observations. Since band formation also relies on other parameters such as φ_∞ and x, each banding map is valid at a given a, φ_∞, ζ_p and x.

Banding maps are presented in the E-$\dot{\gamma}_w$ parameter space because those parameters can be easily varied during a given experiment and so a large number of (E, $\dot{\gamma}_w$) can be tested within a single experiment. Tbl. 5.1 summarizes the particle suspensions tested; Fig. 5.1 shows the banding maps for solutions 1, 2, 3, and 5 in this table.

Table 5.1: List of colloidal particle suspensions studied in these experiments; the values for a and ζ_p are given in terms of the average value ± standard deviation.

#	a [nm]	Electrolytes(s) / pH	ζ_p [mV]	φ_∞ [% (v/v)]
1	245 ± 8	Sodium Tetraborate / 9	–44 ± 9	0.08
2	245 ± 8	Sodium Tetraborate / 9	–44 ± 9	0.17
3	245 ± 8	Sodium Tetraborate / 9	–44 ± 9	0.33
4	245 ± 8	Sodium Tetraborate + Boric Acid / 7	–53 ± 7	0.33
5	355 ± 12	Sodium Tetraborate + Boric Acid / 7	–55 ± 7	0.33

Fig. 5.1 suggests that banding occurs for a minimum E, referred to as E_{min}, and, in most cases, a minimum $\dot{\gamma}_w$. A minimum $\dot{\gamma}_w$ is suspected to exist for all cases since banding, or even the initial accumulation stage, does not occur when $\dot{\gamma}_w = 0$, *i.e.*, "pure" EO flow. However, a minimum $\dot{\gamma}_w$ was not observed for all cases, probably because the experimental setup cannot reproducibly and accurately achieve low shear rates ($\dot{\gamma}_w < 90\ s^{-1}$), and the minimum $\dot{\gamma}_w$ may lie below 90 s^{-1}.

Individual banding maps also suggest that E_{min} increases with $\dot{\gamma}_w$. This can be seen in Figs. 5.1*a* and 5.1*b* as E_{min} changes from ~50 V/cm to ~78 V/cm as $\dot{\gamma}_w$ increases from 730 s^{-1} to 1760 s^{-1} in Fig. 5.1*a* or alternatively as E_{min} changes from ~22 V/cm to ~42 V/cm as $\dot{\gamma}_w$ increases from 200 s^{-1} to 1760 s^{-1} in Fig. 5.1*b*. However, the trend in

Fig. 5.1*c* is much smaller as E_{min} changes from ~19 V/cm to ~22 V/cm as $\dot{\gamma}_w$ increases from 730 s^{-1} to 1760 s^{-1}. A trend, if any exists, was not observable for Fig. 5.1*d*.

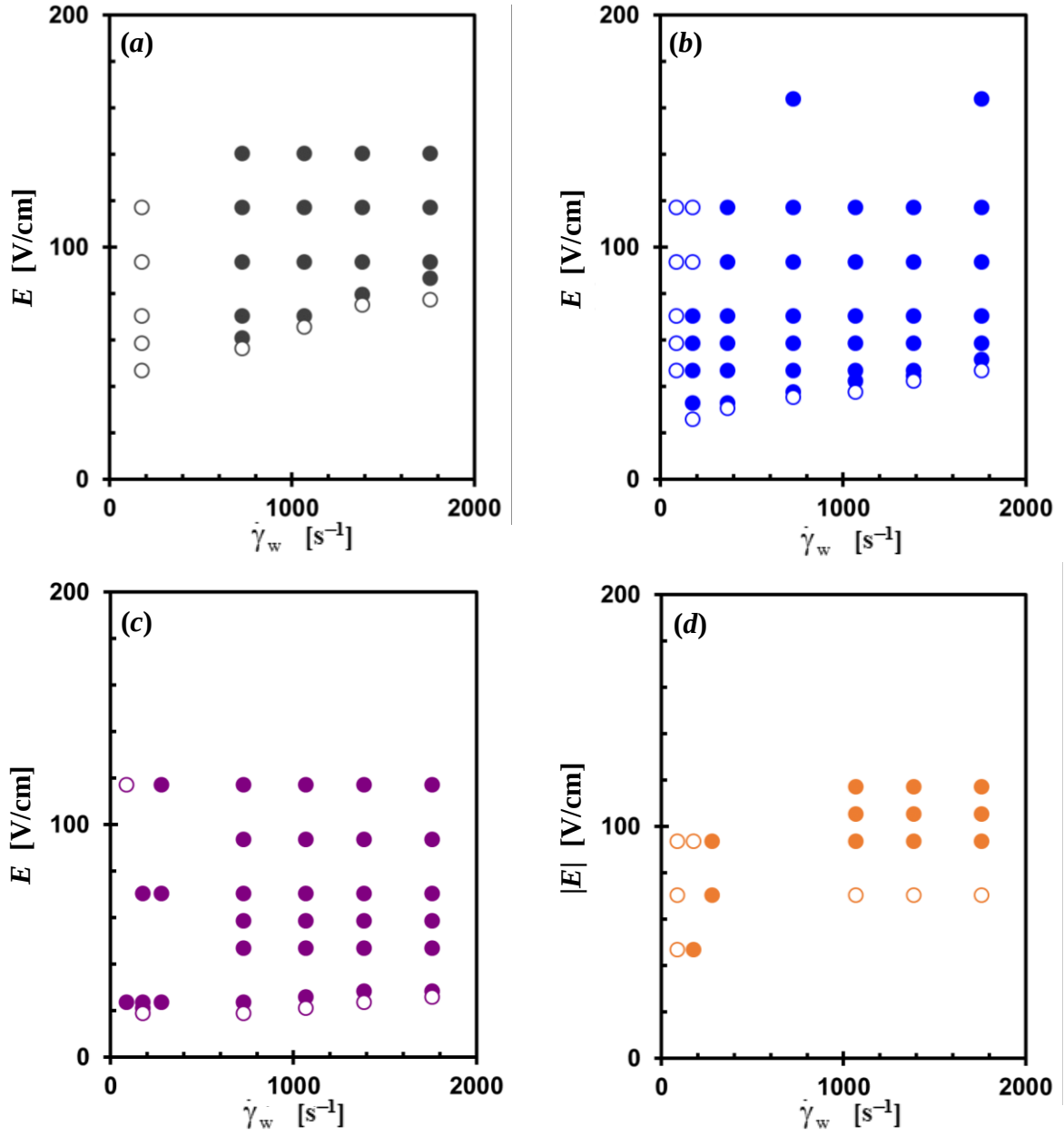

Figure 5.1: Banding maps for Solutions 1–3 and 5 (*cf.* Tbl. 5.1) in the $E - \dot{\gamma}_w$ parameter space, comparing ζ_p = –44 mV and a = 245 nm PS particles in pH 9 $Na_2B_4O_7$ solution at (*a*) φ_∞ = 0.08%; (*b*) φ_∞ = 0.17%; and (*c*) φ_∞ = 0.33%; and (*d*) ζ_p = –55 ± 7 mV and a = 355 nm particles in pH7 $Na_2B_4O_7$–H_3BO_3 solution at φ_∞ = 0.33%. All banding maps are taken in the center of the channel where x = 1.4 cm.

Banding maps at different φ_∞ support the conjecture that decreasing the interparticle spacing in the near-wall region δ_w beyond a critical value is required for band formation. Figs. 5.1*a* to 5.1*c* show that as φ_∞ increases, bands occur over a larger portion of the parameter space. A comparison of this data shows that as φ_∞ changes from 0.08% to 0.33%, E_{min} decreases from about 76 V/cm to 25 V/cm. As the particles gather toward the wall during the accumulation stage, it is logical to assume that under otherwise similar conditions, the near-wall particle fraction increases more rapidly for higher φ_∞. As more particles gather in the near-wall region, the interparticle spacing continues to decrease until it reaches decreases below a critical value, which causes the formation of bands.

Banding maps for different *a* but similar φ_∞ also support the conjecture that the δ_w must fall below a critical value to begin band formation rather than having to exceed a threshold near-wall particle fraction φ_w. Figs. 5.1*c* and 5.1*d* show that as *a* increases, bands form over less of the parameter space, with E_{min} increasing from 39 V/cm to 105 V/cm. Since φ_∞ is kept constant, δ_w drops as *a* increases. This supports the conjecture since it may not be possible for the larger particles to decrease below a threshold interparticle spacing under conditions where the smaller particles could do so.

On the other hand, since the bulk φ_∞ was constant for both banding maps, φ_w may have also been similar under the same conditions. If a threshold near-wall particle fraction, as opposed to a threshold near-wall particle number concentration, needs to be exceeded for bands to occur, then an increase in *a* should have caused bands to occur over a wider parameter space rather than a smaller one.

Section 5.2: Partial Bands

Band formation is also dependent on channel position x and it is possible for bands to only form partially within the channel which leads to a phenomenon called partial banding. Fig. 5.2 shows the presence of bands at different x for various E at steady-state. As E increases, bands form further upstream and bands are seen to occur downstream of a given critical position x_o.

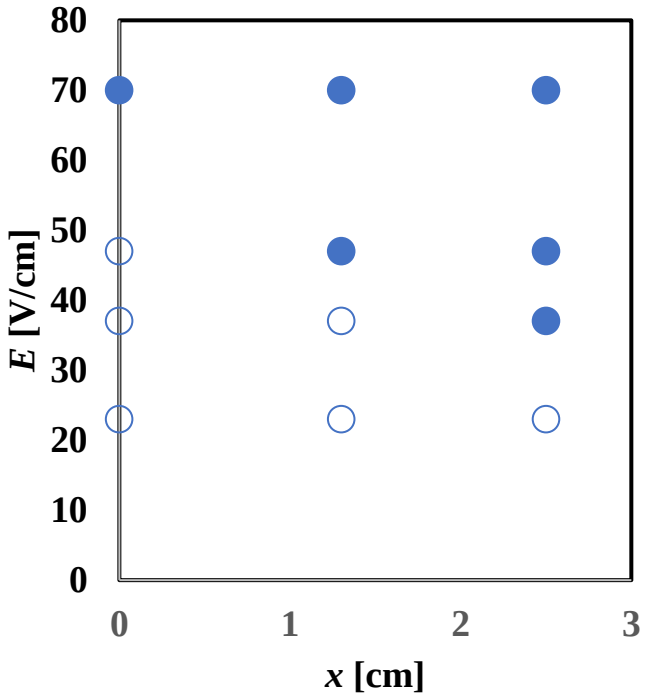

Figure 5.2: Banding map for Solution 2 (*cf.* Tbl. 5.1) in the $E - x$ parameter space, showing $\zeta_p = -44$ mV and $a = 245$ nm PS particles in pH 9 $Na_2B_4O_7$ solution at $\varphi_\infty = 0.17\%$. All data shown was taken under the same $\dot{\gamma}_w = 1390\ s^{-1}$.

The existence of x_o does, in some part, support the conjecture that the bands are convective. One possible explanation is that the band structure first occurs at x_o and then is convected downstream to all other locations.

Section 5.3: Timescales for Band Formation

The time that denotes the end of the accumulation phase when bands begin to form is of particular interest. One reason is that such a timescale may be useful for normalizing t, which could potentially be able to collapse observations under different flow or particle conditions. This would make it easier to determine common characteristics under different conditions. In addition, this time will be essential for closely observing individual particle dynamics at the start of band formation. Particle observations, described in Chapter 6, should ideally occur at high frequencies O(100 Hz) but this causes the amount of data collected to be larger which limits the practical recording duration. Knowledge of the timescale for the end of the accumulation stage would be useful for collecting particle data during this time.

In this work, two algorithms are used to estimate the timescale for band formation. These algorithms are described in Secs. 4.4 and 4.6 and result in timescales T_o and T_I respectively. A comparison between T_o and T_I is discussed in Appendix C.

The dependence of T_o on flow and particle parameters such as E and $\dot{\gamma}_w$ supports the conjecture that the modeled wall-lift force is the causes particle accumulation. Fig. 5.3 shows the influence of two different parameters, ΔE and φ_∞, on T_o for φ_∞ = 0.08%, 0.17%, 0.33%. In almost all cases, as ΔE increases, T_o decreases which is true of all cases except for the lowest φ_∞ = 0.08% where the value for T_o appears to decrease, then reach a minimum value, then increase as ΔE increases. This suggests that the fundamental behavior when φ_∞ = 0.08% may be different than that at higher φ_∞ = 0.17%, 0.33%. Furthermore, upon viewing the data on a semilog plot like in Fig. 5.3, it becomes obvious that T_o decays exponentially with ΔE.

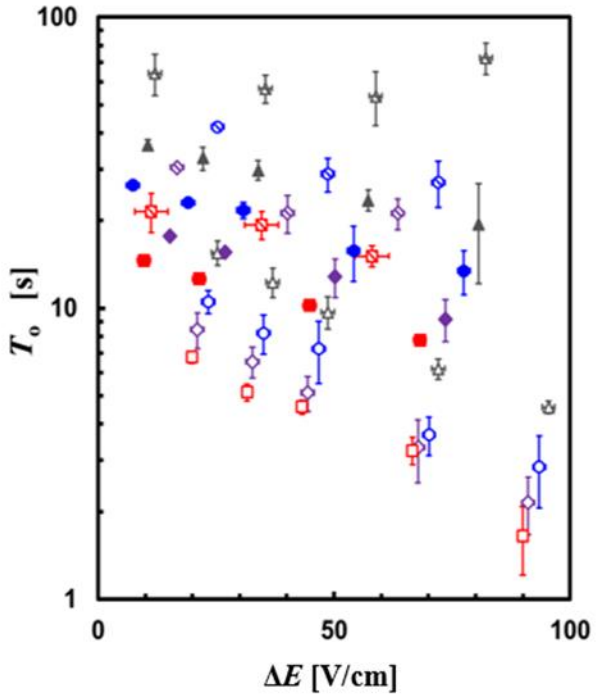

Figure 5.3: Semi-log plot of T_o as a function of ΔE for (*a*) φ_∞ = 0.08% (*hatched*); 0.17% (*filled*) and 0.33% (*open symbols*) at $\dot{\gamma}_w$ = 730 s^{-1} (△), 1070 s^{-1} (○), 1390 s^{-1} (◇), and 1760 s^{-1} (□) for *a* = 245 nm and ζ_p = –44 mV. The error bars denote the standard deviation in these data over three independent realizations.

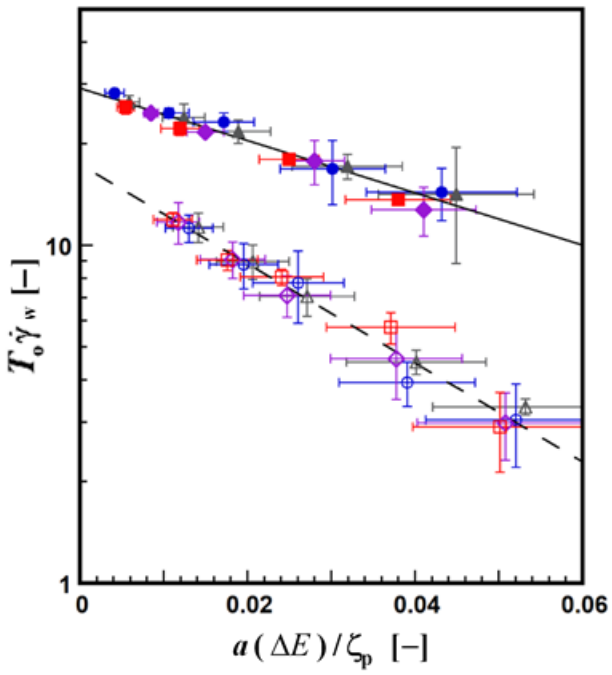

Figure 5.4: Semi-log plot of $T_o\dot{\gamma}_w$ (note the vertical axis labels are scaled by 10^3) *vs.* $a(\Delta E)/\zeta_p$ showing the same data as the previous figure for φ_∞ = 0.17% (*filled*) and 0.33% (*open symbols*) at $\dot{\gamma}_w$ = 730 s^{-1} (△), 1070 s^{-1} (○), 1390 s^{-1} (◇), and 1760 s^{-1} (□). The dashed and solid lines are curve-fits to the data (R^2 = 0.96 and 0.98 for φ_∞ = 0.17% and 0.33%, respectively). The error bars represent the uncertainty in the data.

On the other hand, an analysis on the influence of φ_∞ on T_o supports the conjecture that particles start to assemble into bands when the spacing between particles in the near-wall region decreases below a critical value. In Fig. 5.3 as φ_∞ increases, T_o is shown to decrease. Assuming that banding occurs when the spacing between particles in the near-wall region decreases below a critical value, this can be explained since this critical value could be reached much faster if φ_∞ increases. Thus, T_o should, and does, decrease as a result.

Dimensional analysis was used to simplify these data and determine potential relationships between variables. A fundamental assumption of this analysis is that T_o is a function of the flow, particle and channel parameters ($\dot{\gamma}_w$, ΔE, a, ζ_p, φ_∞, H, ζ_w U, ν),

where U is the maximum (centerline) flow velocity in the channel including the EO flow as well as assuming two-dimensional Poiseuille flow and ν is the fluid kinematic viscosity. The electrical permittivity of the fluid was not considered because it is essentially constant for these experiments. Note that there may be an exception for the value of the electrical permittivity very close to the channel wall due to the presence of the EDL. Le and Zhang (2011) discuss at length how the electrical permittivity should change with proximity to an EDL, but since the Debye length, which characterizes the thickness of the EDL, is 7 nm as mentioned in Sec. 6.2 and the illuminated region is around 300 nm, this effect should be negligible. With ten parameters involving four primary dimensions, namely mass M, length L, time T and current I, there are six independent dimensionless groups based on the Buckingham Pi theorem. The two dimensionless groups involving the independent variables are $T_o\dot{\gamma}_w$ and N_s. For the five dimensionless groups involving dependent variables, the standard channel- and particle-based Reynolds numbers are used: $Re = UH/\nu$ and $Re_p = a^2\dot{\gamma}_w/\nu$, respectively. The other dimensionless groups are φ_∞, $\Pi_4 \equiv a(\Delta E)/\zeta_p$, and $\Pi_5 \equiv a(\Delta E)/\zeta_w$. Here, Re = 0.16–0.56, $Re_p = 4.4\times10^{-5} - 2.5\times10^{-4}$, $\varphi_\infty = 8.0\times10^{-4} - 3.3\times10^{-3}$, $\Pi_4 = 9.5\times10^{-4} - 0.17$, and $\Pi_5 = 4.8\times10^{-4} - 6.9\times10^{-2}$. An alternative Reynolds number based on the bands, which uses the thickness of the band, assumed to be about 5 μm given the results from Lochab *et al*. (2019) and Rossi *et al.* (2019), and the fluid streamwise velocity 5 μm from the channel, was also considered, but this band-based Re, $Re_b = O(10^{-14}$ to $10^{-15})$. This result makes sense given the reduced length scale and velocity close to the channel wall, suggesting that laminar flow dominates the near-wall region.

The application of this dimensional analysis on the data in Fig. 5.3 supports the conjecture that band formation is a convective phenomenon through the relationship between T_o and $\dot{\gamma}_w$. Fig. 5.4 shows a modified version of Fig. 5.3 after normalization using $T_o\dot{\gamma}_w$ and $\Pi_4 \equiv a(\Delta E)/\zeta_p$ while examining data at φ_∞ = 0.17%, 0.33%. The application of these dimensionless groups collapses the data regardless of the value of φ_∞. This suggests that T_o depends upon the inverse of $\dot{\gamma}_w$ and that band formation is a convective phenomenon, at least for a = 245 nm and ζ_p = –44 mV. The decay constants are 5.6×10^{-2} and 3.0×10^{-2} for $T_o\dot{\gamma}_w$, which are based on a curve-fit over all the data at a given φ_∞ (*lines*) for φ_∞ = 0.17% and 0.33%, respectively. The uncertainty in $T_o\dot{\gamma}_w$ and Π_4 are determined using standard error-propagation methods.

A similar analysis was done to compare the results of different a and ζ_p and provides further support for conjecture that band formation is a convective phenomenon. Fig. 5.5 shows the relationship between $T_o\dot{\gamma}_w$ and $\Pi_4 \equiv a(E - E_{min})/\zeta_p$ for ζ_p = –53 and –44 mV. Fig. 5.6 shows the relationship between $T_o\dot{\gamma}_w$ and Π_4 for a = 245 and 355 nm. In both cases, the data once again collapse though it is not clear if this decay is exponential. However, the increase in T_o for more negative ζ_p is unexpected since the modeled wall-normal force from Choudhary *et al.* (2019; 2021) and Khair and Kabarowski (2020) would have suggested an increase in wall attractive force, leading to a lower T_o.

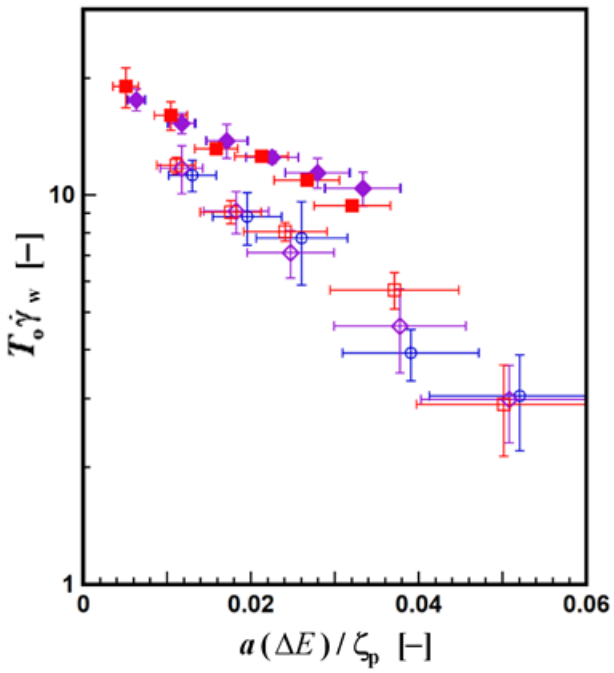

Figure 5.5: Semi-log plot of $T_o\dot{\gamma}_w$ (again scaled by 10^3) as a function of $a(\Delta E)/\zeta_p$ for ζ_p = –53 mV (*filled*) and –44 mV (*open symbols*) at $\dot{\gamma}_w$ = 730 s^{-1} (△), 1070 s^{-1} (○), 1390 s^{-1} (◇), and 1760 s^{-1} (□). The error bars denote the uncertainty in the data.

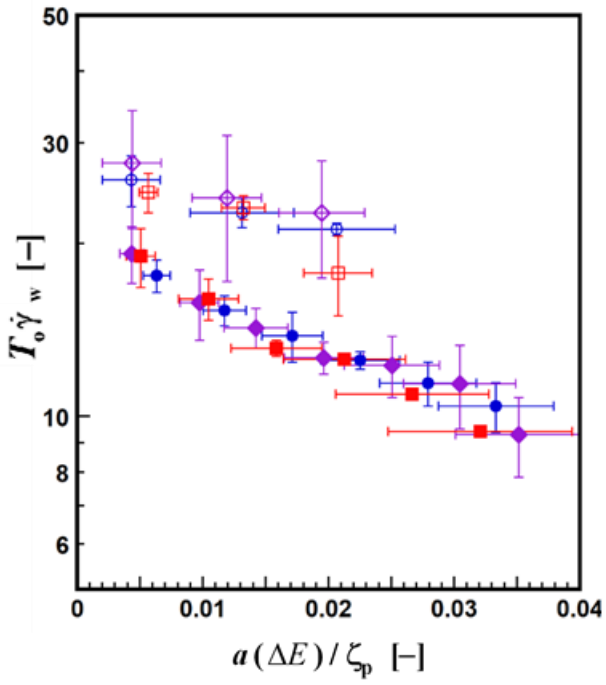

Figure 5.6: Similar to the previous figure, but for a = 245 nm (*filled*) and 355 nm (*open symbols*) particles. Unless stated otherwise, the error bars in all the plots denote the uncertainty.

Lastly, Fig. 5.7 summarizes how the timescale for band formation depends upon x -position, this time represented by T_I. A comparison between T_o and T_I is described in Appendix C. T_I is shown to increase weakly as x increases. Although this trend is consistent across multiple experiments, the increase is too small to be conclusive.

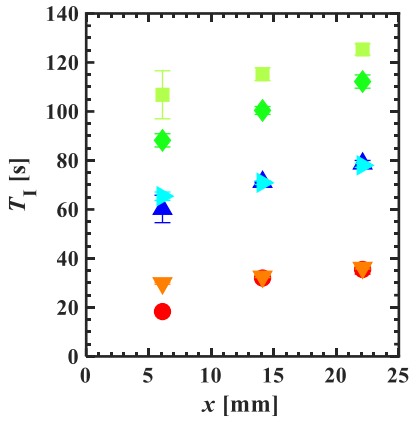

Figure 5.7: Graph of T_I *vs.* x at (ΔE , $\dot{\gamma}_w$, φ_∞) = (63 V/cm, 1390 s^{-1}, 0.17%) (●), (4.7 V/cm, 1390 s^{-1}, 0.17%) (▼), (63 V/cm, 730 s^{-1}, 0.17%) (▲), (4.7 V/cm, 730 s^{-1}, 0.17%) (▶), (29 V/cm, 730 s^{-1}, 0.08%) (♦), and (4.7 V/cm, 730 s^{-1}, 0.08%) (■). Each datapoint is the average over 2–3 independent realizations. The error bars denote the standard deviation in these data; when not shown, the error bars are smaller than the symbols.

Section 5.4: Number of Bands

Given that N_s is defined to be the average number of bands in steady-state over the fixed 203 μm vertical dimension of the images, its inverse N_s^{-1} is proportional to the spatial period, or frequency, of the bands. Fig. 5.8 plots N_s^{-1} as a function of ΔE for (*a*) φ_∞ = 0.08%, 0.17% and 0.33%, then splits the data for (*b*) φ_∞ = 0.08% and (*c*) φ_∞ = 0.17% and 0.33%, again at a = 245 nm and ζ_p = –44 mV. Fig. 5.8*a* suggests that there is no clear relation between N_s^{-1} and φ_∞, while Figs. 5.8*b* and 5.8*c* show that N_s^{-1} increases linearly with ΔE ; the lines are linear curve-fits with $R^2 > 0.96$.

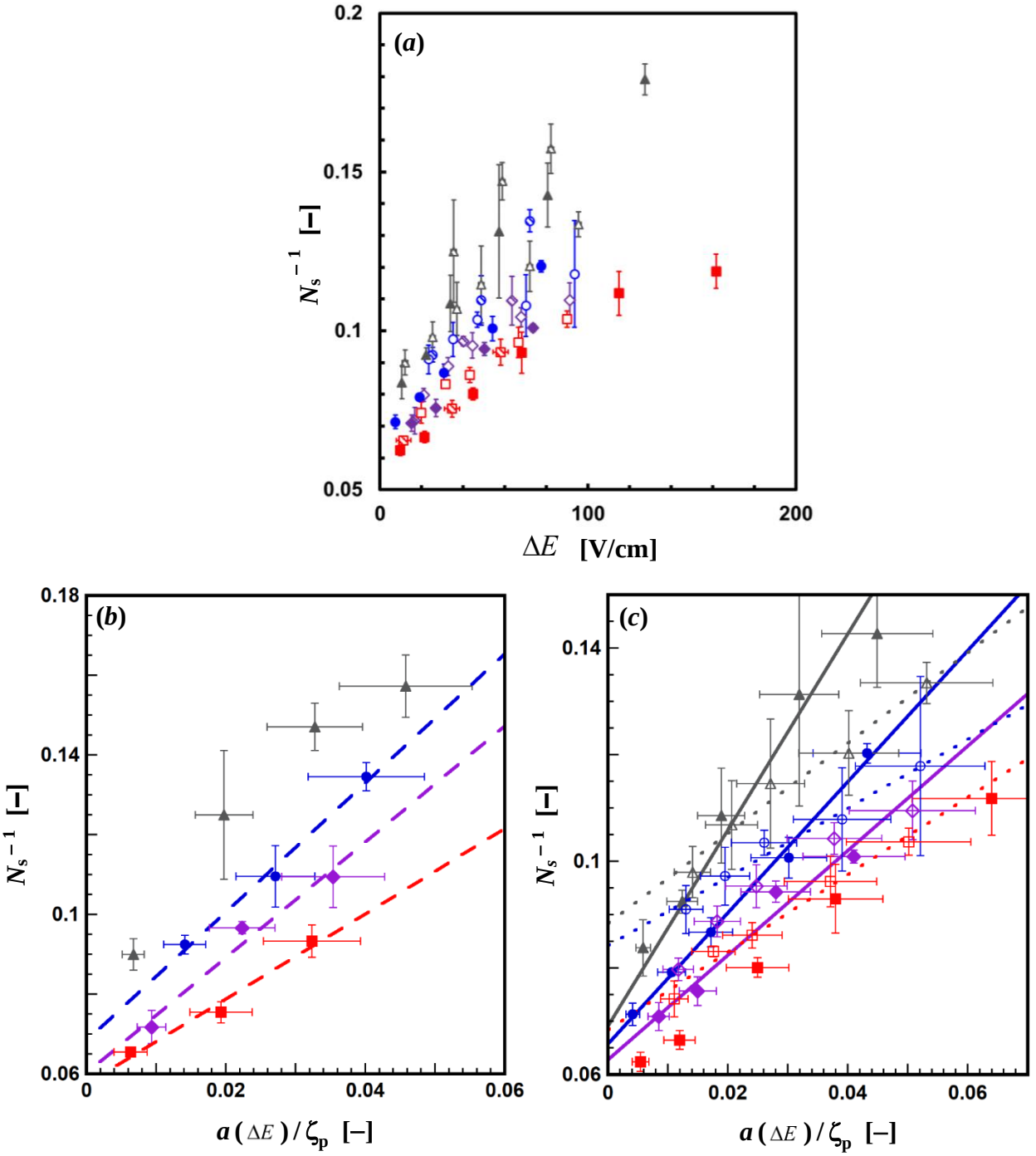

Figure 5.8: Graphs of N_s^{-1} *vs.* $a(\Delta E)/\zeta_p$ for (*a*) φ_∞ = 0.08% (*hatched*), 0.17% (*filled*) and 0.33% (*open symbols*); (*b*) of N^{-1} *vs.* $a(\Delta E)/\zeta_p$ for φ_∞ = 0.08% with linear curve-fits (*dashed lines*); and (*c*) of N_s^{-1} *vs.* $a(\Delta E)/\zeta_p$ for φ_∞ = 0.17% (*filled*) and 0.33% (*open symbols*) with linear curve-fits (*solid* and *dotted lines*, respectively) at $\dot{\gamma}_w$ = 730 s^{-1} (△), 1070 s^{-1} (○), 1390 s^{-1} (◇), and 1760 s^{-1} (□). Only curve-fits with $R^2 > 0.96$ are shown. The error bars denote the uncertainties. Note that (*c*) shows a subset of the data to improve clarity.

As for the other parameters, N_s^{-1} increases with a (Fig. 5.9) and the rate at which N_s^{-1} increases with $a(\Delta E)/\zeta_p$ also increases with a. Finally, a plot of N_s over the 203 μm square field of view (*vs.* N_s^{-1}) as a function of near-wall shear rate $\dot{\gamma}_w$ for a = 245 nm and a = 355 nm particles at ζ_p = –53 mV and –55 mV, respectively, and φ_∞ = 0.33% (Fig. 5.10) shows that N_s increases linearly with $\dot{\gamma}_w$, although the standard deviations in N_s for the a = 355 nm results (*open symbols*) are much greater than those for the smaller particles.

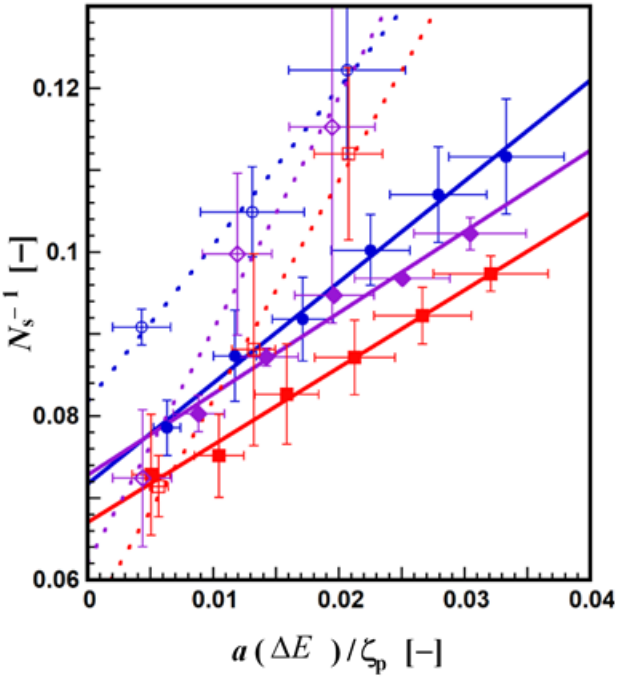

Figure 5.9: Plot of N_s^{-1} as a function of $a(\Delta E)/\zeta_p$ for a = 245 nm (*filled*) and 355 nm (*open symbols*) at $\dot{\gamma}_w$ = 730 s^{-1} (△), 1070 s^{-1} (○), 1390 s^{-1} (◇), and 1760 s^{-1} (□) and linear curve-fits (*solid* and *dotted lines*, respectively) with $R^2 > 0.97$. The error bars denote the uncertainty in the data.

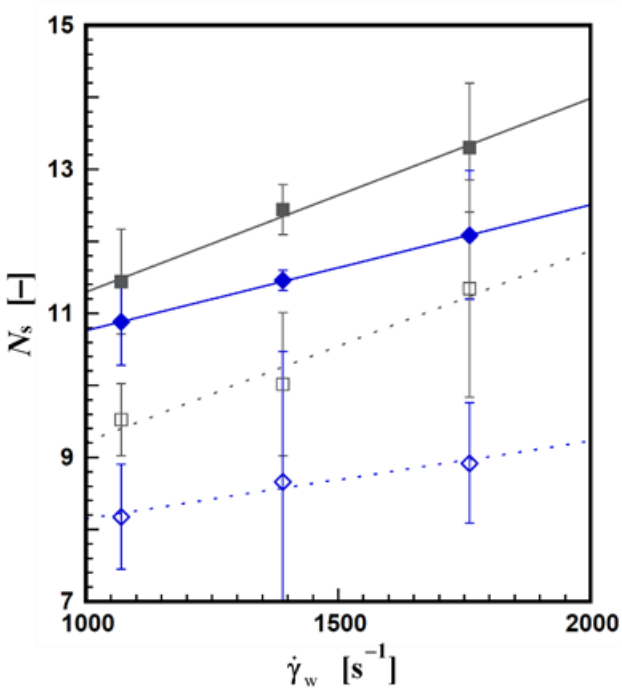

Figure 5.10: Graph of N_s *vs.* $\dot{\gamma}_w$ for a = 245 nm at ΔE = 22±3 V/cm (■) and 34±3 V/cm (◆) and a = 355 nm (*open symbols*) at ΔE = 20± V/cm (□) and 31±1 V/cm (◇). The linear curve-fits (*solid* and *dotted lines*, respectively) have $R^2 > 0.99$ and $R^2 > 0.95$, respectively.

CHAPTER 6
TWO-COLOR EXPERIMENTS

The previous chapter focused on the mechanisms that could influence near-wall particle dynamics and drive band formation. Those experimental visualizations of bands were, however, unable to distinguish the dynamics of individual particles. In a "homogeneous experiment" where all the suspended particles are labeled with the same fluorophore, the particle concentration is too great to distinguish individual particles near the end of the accumulation stage, as well as within the bands. The "two-color experiments" detailed in this chapter use instead a mixture of two particles with similar physical and chemical properties. A small fraction (usually 1%) of the total particles, called tracer particles, are labeled with a different fluorophore from the majority of the particles, called bulk particles. The tracer, or bulk, particles can then be selectively visualized using different emission filters that transmit and/or block the emissions from the two fluorophore labels. The results discussed in this chapter have the conditions $\varphi_\infty = 0.33\%$, with 1% tracer particles at $x = 14.1$ mm unless otherwise stated.

By observing individual particle dynamics, these experiments can estimate near-wall particle velocities, insight into the forces that attract particles to the channel wall, and which (*e.g.* near-wall, bulk) particles assemble into bands. These tracer particle visualizations are used to estimate the number of near-wall particles over time during the accumulation stage and particle velocities during the accumulation and steady-state stages, while bulk particle visualizations are used to determine band characteristics, such as the time scale for band formation, T_o. As a reminder, a significant limitation of the tracer particle visualizations is that quantitative estimates of the particle-wall distance in these

two-color experiments are not feasible since the particle image intensity no longer varies exponentially with wall-normal distance due to significant scattering from neighboring particles, although the particle image intensity should still decrease as the wall-normal distance increases. Therefore, the results in this chapter will not estimate particle-wall distances.

The conjectures that will be addressed in this chapter are:

1. Band formation is caused by interparticle forces between induced dipoles that attract the particles into the band structure. This can be tested by determining if the particles start to assemble into bands when the spacing between particles in the near-wall region decreases below a critical value, or, alternatively, the number concentration of particles in the near-wall region reaches a critical value.
2. The wall-normal force predicted by the results of Choudhary *et al.* (2019; 2021) and Khair and Kabarowski (2020) is the major cause for particle migration towards the channel wall during the accumulation stage. To test this, a model is developed which incorporates this wall-normal force and predicts the timescale for band formation as well as the function that describes how the number of near-wall particles changes over time. This will then be compared to experimental results for validation.
3. The particle velocities lag behind an expected velocity that is the combination of Poiseuille flow, Smoluchowski electroosmotic flow and Smoluchowski electrophoresis. The expression for the expected velocity is developed in this

chapter and will be compared to experimental tracer particle velocities within < 1 μm from the channel wall.

In addition to these conjectures, the results of Rossi *et al.* (2019) and Lochab *et al.* (2020) suggest that the bands have a cross-sectional (*i.e.*, along the *y*- and *z*-directions) dimension of 5–6 μm. Since the *z*-extent of the region that can be observed with evanescent-wave illumination is far less than this cross-sectional dimension, this can be tested by observing how particle counts increase at larger penetration depths and observing if a limit is reached. This is done in Appendix F.

Section 6.1: Particle Growth Rate during Accumulation

The evolution of the number, or concentration, of near-wall particles during the accumulation stage of banding can be used to estimate the wall-normal force that attracts particles to the wall. During band formation, when the particles are concentrated near the wall, individual particles are likely subject to inter-particle forces, particle-wall forces, and the lift force that originally attracted the particles to the channel wall. During the accumulation phase, however, inter-particle distances should be great enough that inter-particle forces are negligible. Based on DLVO theory, particle-wall forces are also negligible (specifically, <10% of the estimated lift force) for particles with centers at $z/a > 7.1$. Since the two-color experiments visualize the number of near-wall tracer particles during the accumulation phase, the evolution of the number of near-wall particles can be used to analyze the wall-normal lift force assuming that this is the dominant force driving particle accumulation.

Fig. 6.1 shows typical examples of the growth in the number of near-wall tracer particles for a single trial N'_T as a function of normalized time $\tau \equiv t / T_o$ over four trials in the same experimental run. The behavior of $N'_T(\tau)$ is fairly consistent over the trials, starting with N'_T = $O(1–10)$ at t < 1 s, then increasing to a maximum value N'_T = $O(10^2–10^3)$, corresponding to a roughly 150-fold increase in particle concentration. The number of near-wall particles then decreases to a roughly steady-state value $N'_T = O(10^2)$. The average standard deviation between multiple trials in $N'_T(\tau)$ over the range $0.1 < \tau < 1.1$ is less than 12% of the average over the same time interval. Given this consistency over individual realizations, the rest of this paper shows $N_T(\tau)$, or $N'_T(\tau)$ averaged over three or four realizations.

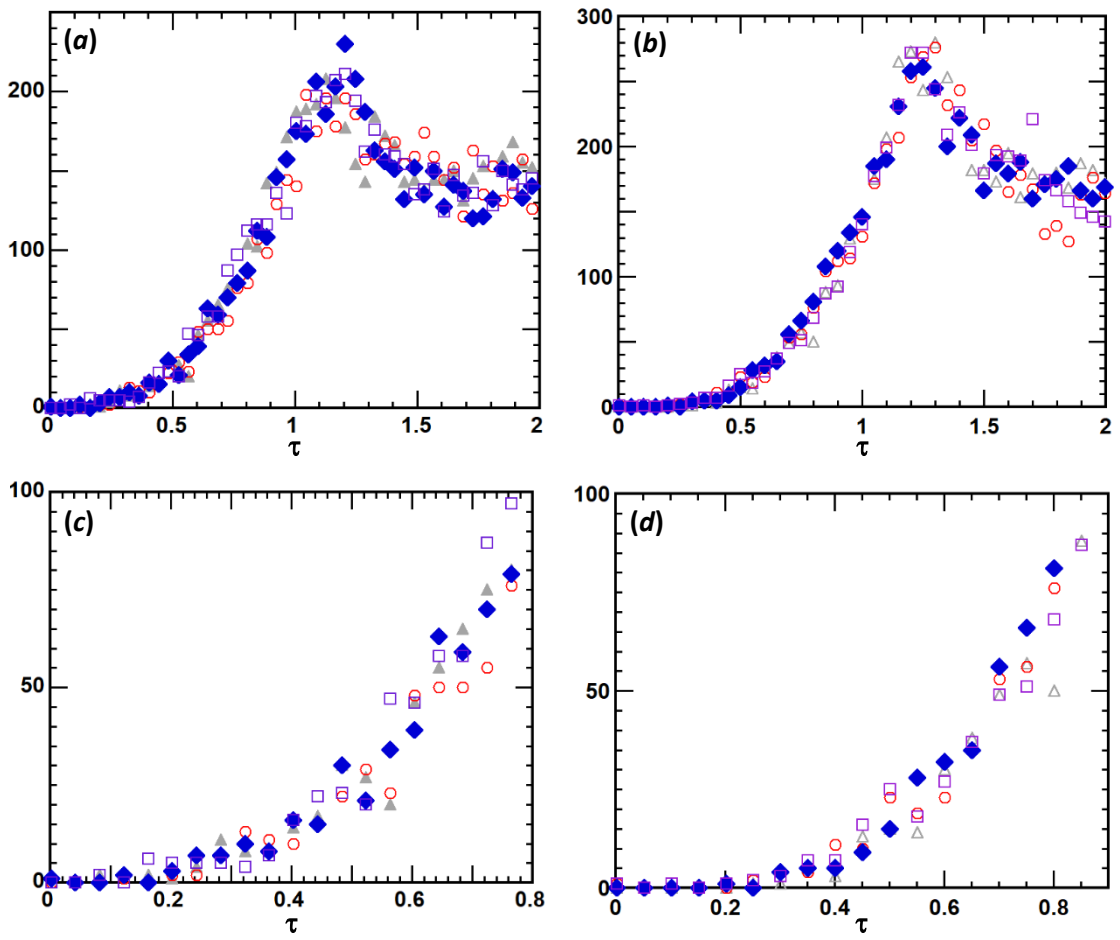

Figure 6.1: Graphs of the number of near-wall tracer particles N'_T as a function of the normalized time $\tau = t/T_o$ at a near-wall shear rate $\dot{\gamma}_w = 1760\ s^{-1}$ and $E = 126$ V/cm (*a*, *c*) or 150 V/cm (*b*, *d*). Different symbols represent results for four independent different realizations (▲,○,◆,□); the temporal resolution of these data is 1 s. The graphs in the bottom row show N'_T over a smaller range of τ.

One feature of Fig. 6.1 that is of particular interest is the initial increase of N'_T from $t = 0$ to its maximum value at a later time during the accumulation phase, typially at a time $\tau \equiv t / T_o$ which varies from 1 to 1.4 over all six cases described in Tbl. 6.1. In Fig. 6.1, the time interval that is used to estimate the start of the banding phase and the end of the accumulation phase, T_o, typically occurs during this initial increase, usually just before or at the peak in the particle count. Thus this initial rise in N'_T can be considered to represent the accumulation phase of banding.

The evolution of the mean grayscale over time $\bar{G}(t)$, shown in Fig. 6.2 is qualitatively similar to the particle count, with an initial increase that roughly corresponds to the accumulation stage. The maximum mean grayscale occurs at a (physical) time, t = 61 s, similar to that for the maximum N_T', both being around 61 s; $\bar{G}$ then decreases to a roughly constant steady-state value, again at a time, t = 94 s, when N_T' also decreases to its steady-state value.

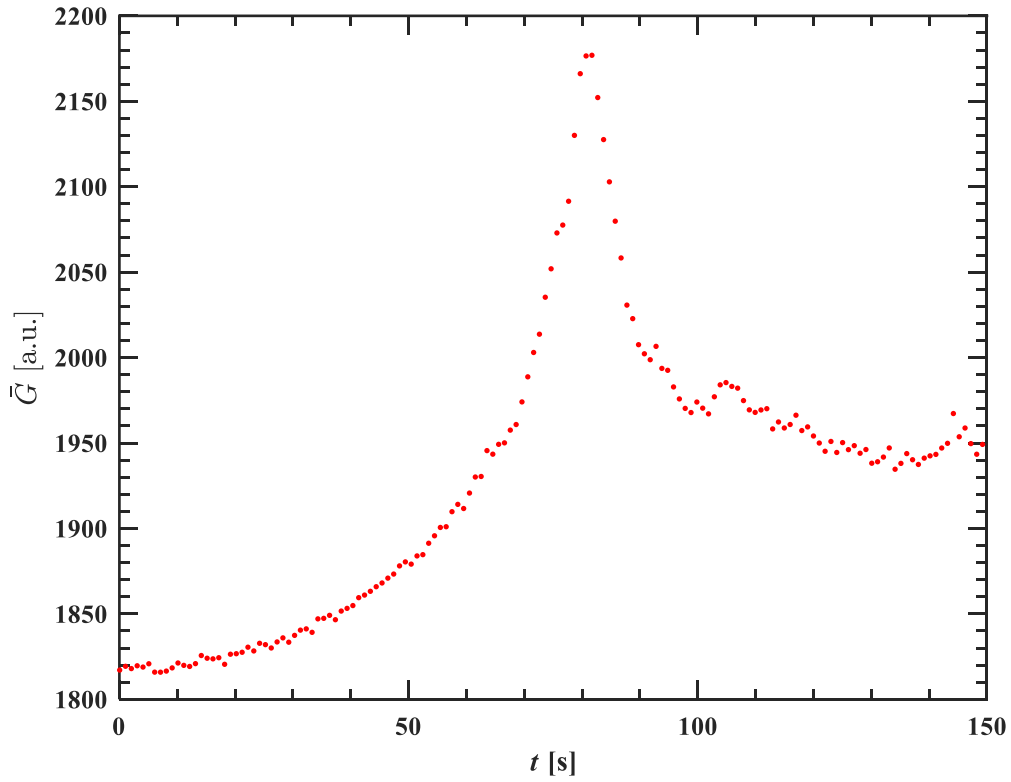

Figure 6.2: The average grayscale $\bar{G}$ (shown as dots) as a function of time t at $\dot{\gamma}_w$ = 730 s^{-1} and E = 108 V/cm. The temporal resolution of these data is 1 s.

Fig. 6.3 shows $N_T(\tau)$ for E = 126 V/cm and 150 V/cm at $\dot{\gamma}_w$ = 730 s^{-1} (*a*) and 1760 s^{-1} (*b*). Although T_o decreases as E increases, it appears that N_T at a given τ increases as E decreases during the accumulation stage. Fig. 6.4, which compares $N_T(\tau)$

at the two near-wall shear rates $\dot{\gamma}_w$ = 730 s^{-1} and 1760 s^{-1} at $E \approx 128$ V/cm, shows that N_T at a given τ increases as $\dot{\gamma}_w$ decreases. The initial growth in the number of near-wall tracer particles for different E or $\dot{\gamma}_w$ is qualitatively similar, suggesting that it may be possible to describe $N_T(\tau)$ by a single function over a range of flow parameters. Moreover, it also suggests that, for data at the same $\dot{\gamma}_w$ but different E, there is a common critical particle number concentration for bands to form.

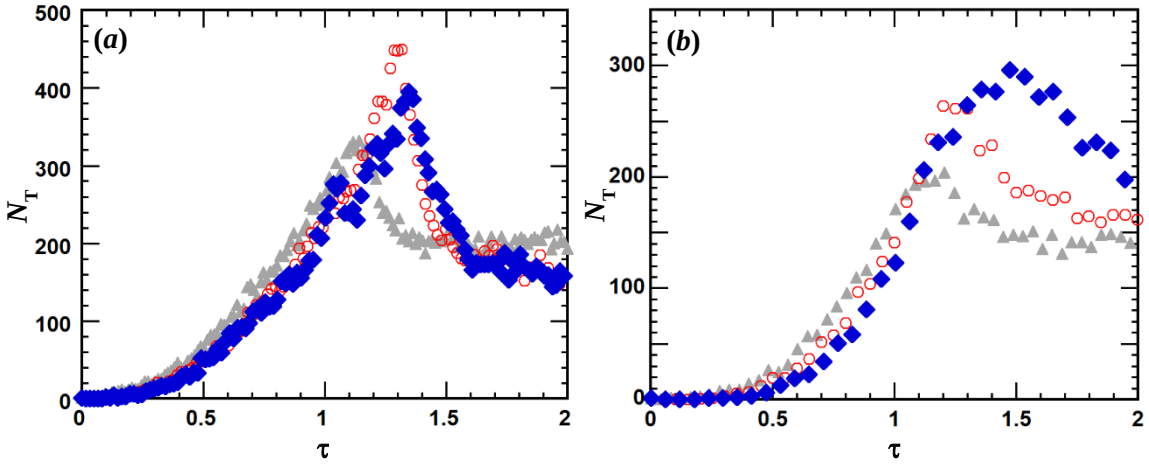

Figure 6.3: Average number of near-wall tracer particles N_T as a function of the normalized time τ at (*a*) $\dot{\gamma}_w$ = 730 s^{-1} and E = 84 (▲, T_o = 74.1 s), 108 (○, T_o = 62 s), and 131 V/cm (◆, T_o = 61.4 s) and (b) $\dot{\gamma}_w$ = 1760 s^{-1} and E = 126 (▲, T_o = 25.1 s), 150 (○, T_o = 20.2 s), and 173 V/cm (◆, T_o = 17.1 s). These data represent the average over three or four independent different realizations for a threshold grayscale of 6000.

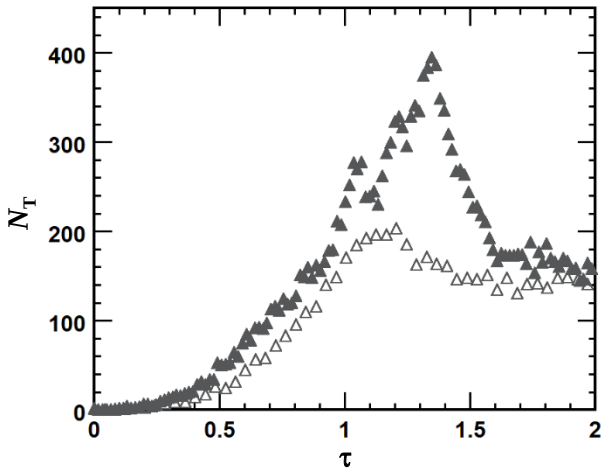

Figure 6.4: Average number of near-wall tracer particles N_T *vs.* normalized time τ at E = 128±3 V/cm for $\dot{\gamma}_w$ = 730 s^{-1} (▲, T_o = 61.4 s) and 1760 s^{-1} (△, T_o = 25.1 s).

Attempts were therefore made to approximate the evolution of $N_T(\tau)$ using several functions to obtain a curve-fit, along with $N_T(\tau)$ itself, that could be compared to a theoretical model. Given the positive curvature of $N_T(\tau)$, results for the average number of near-wall particles over six different experimental cases, described in Tbl. 6., were curve-fit over the time interval $0.4 < \tau < 1.1$ to: 1) an exponential function of the form $N_T(\tau) = d\exp\{c\tau\} + f$, where *c*, *d* and *f* are constants determined from the data; and 2) a power-law function of the form $N_T(\tau) = a\tau^P + b$, where *a* and *b* are constants determined from the data and *P* is an integer exponent tested between 1 to 5. This time interval was chosen to start when there are at least a few tracer particles near the wall and to end before significant particle aggregation or assembly was observed. The power-law exponent of 2 or 3 was chosen based on an initial curve-fit of the data to a power-law function with an arbitrary positive exponent. In all but one of the six cases, the exponential curve-fit has a lower root-mean-square error (RMSE) than either power law fit, with an average RMSE normalized by the average number of particles over all six cases of 5.6%, *vs.* 7.6% and

8.4% for the power-law curve-fit for $P = 3$ and 2, respectively. Note that the variable c for the exponential curve-fit (Tbl. 6.1) increases with E at a given shear rate for all six cases, suggesting a more rapid growth in N_T as the electric field magnitude increases, even after accounting for the length of the accumulation stage.

Table 6.1: Values of c for the Exponential Fit with Constant $N_T(\tau) = d\exp\{c\tau\} + f$ over all six experimental cases.

$\dot{\gamma}_w$ = 730 s^{-1}		$\dot{\gamma}_w$ = 1760 s^{-1}	
E **[V/cm]**	***c*** **[–]**	***E*** **[V/cm]**	***c*** **[–]**
84	0.98	126	1.70
108	1.26	150	2.87
131	1.96	173	3.38

In addition, to the fit $N_T(\tau) = d\exp\{c\tau\} + f$, an alternative fit was made of the form $N_T(\tau) = d\exp\{c\tau\}$ was also tested. The values of c for that fit, shown in Tbl. 6.2, still increase with E, but appear to only increase slightly with E. The average RMSE over all six cases also increases from 5.6% to 8.8%, making it likely that the constant f has a significant effect upon the curve-fit.

Table 6.2: Values of c for the Exponential Fit without Constant $N_T(\tau) = d\exp\{c\tau\}$ over all six experimental cases.

$\dot{\gamma}_w$ = 730 s^{-1}		$\dot{\gamma}_w$ = 1760 s^{-1}	
E **[V/cm]**	***c*** **[–]**	***E*** **[V/cm]**	***c*** **[–]**
84	2.41	126	3.10
108	2.62	150	3.84
131	2.84	173	4.35

One note about the experimental values of the number of "detected" tracer particles N_T' (and N_T) are that they depend upon the threshold grayscale value used to differentiate

particles from the background. In these experiments, the default grayscale value is 4000, or about twice the average background grayscale value estimated from images at times before $t = 0$. Using a higher grayscale threshold would eliminate noise that is mistaken for particles, but also the particle images that relatively dim. Fig. 6.5 shows $N_T(\tau)$ for the same images analyzed in Fig. 6.3, but with a higher threshold grayscale value of 6000, *vs.* 4000.

The number of particles detected in Fig. 6.5 is significantly less than that in Fig. 6.3 under otherwise identical conditions. For example, at $t \approx T_o$, $N_T \approx 100–300$ (depending on E and $\dot{\gamma}_w$) in Fig. 6.3, while $N_T \approx 50–200$, in Fig. 6.5. Changing the threshold grayscale appears, however, to have little, if any effect upon variations between trials; the standard deviation in N'_T between trials is in all cases less than 14% of the average for a threshold grayscale of 6000, *vs.* 14% at a given t for a threshold of 4000, over $0.1 < \tau < 1.1$. Based on these results, the default threshold grayscale value used in the rest of this chapter was taken to be 4000.

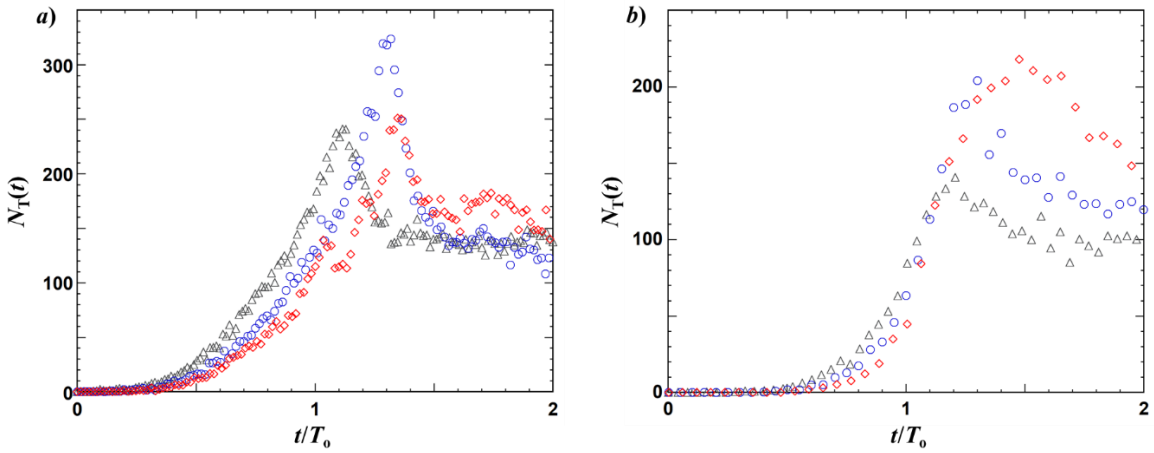

Figure 6.5: Average number of near-wall tracer particles N_T over time as a ratio of the time at which band form t/T_o at (*a*) $\dot{\gamma}_w$ = 730 s^{-1} and E = 84 (△, T_o = 74.1 s), 108 (○, T_o = 62 s), and 131 V/cm (◇, T_o = 61.4 s) and (b) $\dot{\gamma}_w$ = 1760 s^{-1} and E = 126 (△, T_o = 25.1 s), 150 (○, T_o = 20.2 s), and 173 V/cm (◇, T_o = 17.1 s). These data represent the average over four independent different realizations for a threshold grayscale of 4000.

Section 6.2: Comparison with Lift Force Predictions: Assumptions

Two recent studies, Choudhary *et al*. (2019; 2021) and Khair and Kabarowski (2020), have modeled the theoretical wall-normal lift force on colloidal particles subject to a combination of shear flow and a DC electric field. Due to similarities to the experiments discussed in Sec. 6.1, it is conjectured that the theoretical wall-normal lift force, which would be attractive for those experiments, and the opposing Stokes drag are the major forces governing particle wall-normal dynamics during the accumulation phase. Only the accumulation stage of banding is considered because it is assumed that other forces such as interparticle or particle-wall interactions are too significant near the end of the accumulation stage and the later stages of banding to isolate the effect of attractive wall-normal lift force. To test this conjecture, a general comparison of potential major forces on the particles in the bulk of the channel is described in Sec. 6.2. After hypothesizing that the theoretical wall-normal lift force and Stokes drag are the major forces on the particles

during accumulation, Sec. 6.3 describes the comparison between a simulation incorporating these two forces and the results presented in Sec. 6.1 to determine if the simulation supports the hypotheses that the theoretical wall-normal lift force is a major force on the experimental particles during accumulation.

As discussed in Sec. 2.2.3, both Choudhary *et al*. (2019; 2021) and Khair and Kabarowski (2020) modeled a spherical particle in a combination of a constant streamwise shear flow and constant streamwise electric field and reported a wall-normal force shown in Eq. 2.5, but expressed again for clarity in Eq. 6.1:

$$F_{\mathrm{L}} = 1.75\pi \frac{\varepsilon \left|\zeta_{\mathrm{p}}\right| a^3 \dot{\gamma} E}{\nu} \qquad [6.1]$$

The magnitude of the wall-normal lift force magnitude $F_{\mathrm{L}} = O(10^{-2}\ \mathrm{fN})$ in these experiments, based on Eq. 6.1 and average experimental conditions from Tbl. 6.1. These estimates are based on E = 84–131 V/cm or E = 126–173 V/cm and $\dot{\gamma}$ of 365 s^{-1} or 880 s^{-1}, respectively, corresponding to one-half the near-wall shear rates $\dot{\gamma}_{\mathrm{w}}$ = 730 s^{-1} or 1760 s^{-1}.

Other forces along the z-direction include buoyancy forces due to particle-fluid density mismatch, interparticle forces and particle-wall forces. These forces should be negligible during most of the accumulation phase, as detailed next. The particle buoyancy should be negligible because the density mismatch $\Delta\rho$ between polystyrene and water is small—about 7 $\mathrm{kg/m}^3$—based on the density of DI water of 998 $\mathrm{kg/m}^3$ at 21 °C and the density of the polystyrene beads, specified by the manufacturer, Invitrogen, of 1005 $\mathrm{kg/m}^3$. The buoyancy force on a particle, using Eq. 2.6, is $O(10^{-3}\ \mathrm{fN})$. The particle buoyancy force, which is an order of magnitude less than the average value of F_{L}, is therefore considered to be negligible.

The magnitude of interparticle and particle-wall forces depend on their separation. Therefore, estimating these forces requires estimates of the interparticle and particle wall spacing during the accumulation stage which can be done with the results from Sec. 6.1. In general, both should decrease over time during the accumulation phase as more particles are attracted to the channel wall. At the start of the accumulation phase, N particles can be assumed to lie within a volume $\forall$, where the particle volume fraction $\varphi_\infty = N(4\pi a^3/3)/\forall$. The average interparticle spacing, can then be estimated as twice the radius of a sphere with the average volume occupied by a single particle $\forall / N$:

$$\delta_\infty = 2\left(\frac{3\forall}{4\pi N}\right)^{1/3} \qquad [6.2]$$

where δ_∞ is the average interparticle spacing, also known as twice the Wigner-Seitz radius. At the beginning of the accumulation stage, the particle volume fraction is the bulk value, or $\varphi_\infty = 1.7\times10^{-3}$. So $\delta_\infty = 4.1$ μm $= 16.8a$, where $a = 0.245$ μm.

At the end of the accumulation phase, visualizations indicate that there are 200 near-wall tracer particles, where the tracer particles are 1% of all the particles, over a 203 μm square field of view. Assuming that only a single layer of particles is visualized by evanescent-wave illumination, the average interparticle spacing can be estimated as twice the radius of a circle with the average area occupied by a single particle:

$$\delta_w = 2\sqrt{\frac{A}{\pi N}} \qquad [6.3]$$

where A is the area of the field of view. For $N = 200$ and area $A = (203\ \mu m)^2$, $\delta_w = 1.6$ μm $= 6.6a$ for $a = 0.245$ μm.

In addition, by isolating the number of particles within the bands at steady-state and comparing the number to the area of the bands as discussed in Sec. 4.2, an estimate of the interparticle spacing within the bands and between the bands can be made. For a data sample at $\dot{\gamma}_w$ = 1760 s^{-1}, E = 150 V/cm, φ_∞ = 0.33%, the interparticle spacing within bands $\delta_b \sim 2a$ and the interparticle spacing between the bands $\delta_n \sim 50a$. Note that these estimates of δ assume that the particles are uniformly distributed over the region of interest.

These estimates of δ can then be used to estimate the interparticle force. The potential energy between two spheres of diameters D_1 and D_2, $E_{\delta p}$, is described by Hamaker (1937) in Eq. 2.8 and the repulsive London-van der Waals force is $\partial E_{\delta p} / \partial \delta$. The magnitude of the force was estimated by a forward difference method with $\Delta\delta$ = 1 pm which is at least 6 orders of magnitude smaller than δ. The repulsive London-van der Waals force increases from about 2.8×10^{-6} fN at the beginning of the accumulation stage (for δ_s = 4.1 μm) to about 1.9×10^{-5} fN at the end of the accumulation stage (for δ_w = 1.6 μm) assuming that $A = 0.95\times10^{-20}$ J (Leite *et al.* 2012). These force magnitudes are about two orders of magnitudes lower than F_L, suggesting that the London-van der Waals force is also negligible.

Lastly, the particle-wall force can be estimated using Eq. 2.9, which expresses the potential energy between a spherical particle and an infinite wall due to the London-van der Waals or $E_{\delta w}$. The repulsive particle-wall force can be estimated by $\partial E_{\delta w} / \partial z$ determined using the same method as the interparticle force which is a forward difference method with $\Delta\delta$ = 1 pm. Given that $F_L = O(10^{-2}$ fN), the particle-wall force magnitude would have to be at least $O(10^{-4}$ fN) to be non-negligible compared with F_L. Based on

Eq. 2.9, the particle-wall force exceeds 10^{-3} fN when $z < 1.8$ μm $= 7.1a$. Given that this corresponds to $z < 0.05H$, where the channel depth $H = 34.1$ μm, the particle-wall force is also assumed to be negligible compared with the predicted wall-normal lift force during the accumulation phase where particles in the bulk of the lower half of the channel (*i.e.*, $z \leq 0.5H$) are attracted to the channel wall.

The last force considered is Stokes drag which is discussed in Sec. 2.3 and expressed in Eq. 2.7. To determine the component of the Stokes drag in the wall normal-direction, an estimate of the wall-normal velocity during accumulation must be made. Given that the typical T_o for the particles to reach the channel wall is 43 s for the six cases mentioned in Tbl. 6.1 and the typical particle distance traveled during this time during the accumulation phase is estimated as $H/4$ assuming that the particles are evenly dispersed in the channel before the voltage gradient is on, an estimate of the typical particle velocity in the wall-normal direction is 0.14 μm/s. Using Eq. 2.7, the typical Stokes drag magnitude is $D_z = O(10^{-1}$ fN), or comparable to the magnitude of the wall-normal lift force F_L.

These estimates suggest that F_L and D_z are the dominant forces during the accumulation phase. It is also important to consider whether the assumptions made by Khair and Kabarowski (2020) and Choudhary *et al*. (2019; 2021) apply to these experiments. Both models considered the case where the particle is suspended in a shear flow at a constant $\dot{\gamma}$, while the particles in the experiments are subject to a shear rate that increases linearly from the channel centerline, and hence effectively a time-varying shear rate as they migrate towards the wall. It can be argued, however, that these unsteady effects in the experiments are negligible based on scaling arguments. The usual dimensionless group that characterizes the relative importance of unsteady, *vs.* inertial, effects is the

Strouhal number *St*. Here, $St = HT_o / U$ based upon a length scale of the channel hydraulic diameter, essentially *H* for a high aspect ratio cross section, a time scale of T_o, the length of the accumulation stage, and a velocity scale of *U* taken to be the minimum average velocity along the streamwise direction in the experiments, specifically when *E* = 131 V/cm and $\dot{\gamma}_w = 730\ s^{-1}$. For the maximum values of *H* = 34 μm and T_o = 60 s, and the minimum value of *U* of 0.03 m/s, the maximum $St = O(10^{-2})$, suggesting that the variations in shear rate over time are negligible in the experiments. Given that D_z is proportional to the velocity of the particle along the wall-normal direction, or $\partial z / \partial t$, this value of *St* also suggests that the variations in $\partial z / \partial t$ over time are also negligible.

The models also assume that the particle-fluid lag is constant and given by the Helmholtz-Smoluchowski equation for the electrophoretic velocity. This equation is derived under the assumptions that the (particle or wall) electric double layers (EDLs) are thin, and the contribution of bulk conductivity is larger than that of surface conduction for the particle. The thickness of the EDL is characterized by the Debye length κ^{-1}, and for the thin EDL assumption to be valid, $\kappa a >> 1$. The relative importance of bulk conductivity and surface conduction is characterized by the dimensionless Dukhin number *Du*.

To determine κ^{-1} and *Du*, the electrolyte composition of the electrolyte solution must first be determined. The pH of the 1 mM sodium tetraborate ($Na_2B_4O_7$) aqueous solution was measured to be ~9.2. Since the dissociation constant for water $K_D \equiv [H^+][OH^-] = 10^{-14}$, this gives H^+ and OH^- concentrations of $[H^+] = 6.3\times10^{-10}$ M and $[OH^-] = 1.6\times10^{-5}$ M, respectively. These values are then used to estimate the

concentration of the other chemical species in solution (Na^+, NaOH, $B(OH)_4^-$, and $B(OH)_3$) based on the dissociation of the decahydrate salt of the sodium tetraborate. Note that $[Na^+]$ = 2 mM, since almost all of the sodium atoms added to the solution will remain Na^+ at pH 9.2, since the (logarithm of the) base dissociation constant $pK_b = 0.2$ for the reaction $NaOH \rightarrow Na^+ + OH^-$. The various borate species, on the other hand, provide a weak buffering capability at this pH via the reaction

$$B(OH)_3 + H_2O \leftrightarrow B(OH)_4^- + H^+$$

with equilibrium constant $pK = \log_{10}\left\{[B(OH)_4^-][H^+]/[B(OH)_3]\right\} = 9.1$. For a total borate concentration of 4×10^{-3} M, this gives $[B(OH)_3] = 1.9\times10^{-3}$ M and $[B(OH)_4^-] = 2.1\times10^{-3}$ M. The concentrations of these two borate species are comparable, suggesting that this is an effective buffer at this pH. In summary, this solution can be approximated as a monovalent (and symmetric) electrolyte solution with a molar concentration of 2×10^{-3} M.

This electrolyte composition can now be used to estimate the Debye length κ^{-1} which is discussed in Sec. 2.1 and expressed in Eq. 2.1. For the ion composition described in the previous paragraph (note that $z_i = \pm 1$ for this monovalent solution), $\kappa^{-1} \approx 7$ nm at T = 295 K. So $\kappa a = O(10^{-2})$, and the thin EDL assumption is valid for these experiments.

Next, the Dukhin number, which characterizes the relative importance of surface to bulk conductivity,

$$Du = \frac{K_\sigma}{K_L L_a} \qquad [6.4]$$

where K_σ and K_L are the surface and bulk conductivities, respectively, and L_a is a length scale that characterizes the surface curvature. To estimate *Du* for the particles, L_a is taken to be *a*.

The surface conductivity has two components, namely the contribution of the two "layers" of counterions in the EDL: the diffuse and stagnant layers. The contribution of the diffuse layer $K_{\sigma d}$ is determined by applying the Bikerman equation to an electrolyte solution containing *N* cation species and *M* anion species:

$$K_{\sigma d} = \frac{2e^2 N_A}{kT\kappa}\left[\begin{array}{l}\displaystyle\sum_{i=1}^{N} z_i^2 c_i D_i \left(\exp\left\{-\frac{z_i e\zeta}{2kT}\right\}-1\right)\left(1+\frac{3m_i}{z_i^2}\right) \\ \qquad\displaystyle+\sum_{j=1}^{M} z_j^2 c_j D_j \left(\exp\left\{\frac{z_j e\zeta}{2kT}\right\}-1\right)\left(1+\frac{3m_j}{z_j^2}\right)\end{array}\right] \qquad [6.5]$$

where *c* is the electrolyte concentration in mol/m^3, $N_A = 6.02\times10^{23}$ is Avogadro's number, and D_i and m_i (or D_j and m_j) are the ionic diffusion coefficient and the dimensionless mobility, respectively of the i^{th} cation (and j^{th} anion) species. Here, the mobility

$$m = \frac{2}{3}\left(\frac{kT}{e}\right)^2 \frac{\varepsilon}{\mu D} \qquad [6.6]$$

The diffusion coefficient of a boric acid solution with a molar concentration of 0.94 mM is 1.06×10^{-9} m^2/s (Park and Lee 1994), while that for Na^+ in an aqueous solution is 1.485×10^{-9} m^2/s (Vitagliano 1956), or of a similar order of magnitude. In a review paper, Delgado *et al.* (2007) estimates *Du* for a symmetrical electrolyte with a valence (magnitude) of *z* and identical anion and cation diffusion coefficients to be:

$$Du = \frac{2}{\kappa a}\left(1+\frac{3m}{z^2}\right)\left[\cosh\left(\frac{ze\zeta_p}{2kT}\right)-1\right]\left(1+\frac{K_{\sigma i}}{K_{\sigma d}}\right) \qquad [6.7]$$

where $K_{\sigma i}$ is the contribution of the stagnant layer.

Many studies (Carrique *et al.* 2007, Lyklema 2000) mention that it is commonly considered for the contribution of the stagnant layer to be negligible compared to the diffuse layer, *i.e.* $K_{\sigma i} \ll K_{\sigma d}$. Jiménez *et al.* (2005) gives an expression for the contribution of the stagnant layer assuming that no liquid motion can take place in the inner part of the ionic atmosphere and that only counterions can participate in charge transport:

$$K_{\sigma i} = \frac{eD_{SL}\sigma_{SL}}{k_B T} \qquad [6.8]$$

where D_{SL} is the diffusion coefficient of counterions absorbed at the stagnant layer and σ_{SL} is the Stern potential, or the charge at the outer edge of the stagnant layer. Since D_{SL} and σ_{SL} are unknown for the fluorescently labeled particles used in these experiments, this analysis will, like most models, also assume that the contribution of the stagnant layer is negligible, *i.e.*, $K_{\sigma i} / K_{\sigma d} \ll 1$.

For $K_{\sigma i} / K_{\sigma d} \ll 1$, $Du \approx 0.022$, a value that suggests that the bulk conductivity has a much greater contribution than surface conduction. In summary, it appears that the Helmholtz-Smoluchowski equation for the electrophoretic velocity is valid since the thickness of the EDL, characterized by κ and ζ_p, gives a Dukhin number below unity.

Section 6.3: Comparison with Lift Force Predictions: Model

The particle dynamics along the wall-normal, or *z*, direction were simulated over the lower half of the channel to determine if the experimental observations of the number of near-wall particles over time were consistent with the wall-normal lift force described

by Choudhary *et al.* (2019; 2021) and Khair and Kabarowski (2020). These simulations consider the major forces on the particles along the z-direction during the accumulation phase as the particles in the bulk of the channel approach the channel wall. These forces are then used to determine the particles' wall-normal position as a function of time, or $z(t)$.

Only particles in the lower half of the channel were considered since it was assumed that the vast majority of the particles attracted to the lower wall started in this region. A simulation implemented in MATLAB "tracks" an array of evenly dispersed particles at $t = 0$ over time, and determines when these particles are in the near-wall region, defined to be z farther than a specified distance from the channel centerline R. This simulation uses the results to estimate how the number of near-wall particles increases over time. Recall that $0 \leq z \leq 0.5H$ for particles in the lower half of the channel, where $z = 0$ at the channel centerline and $z = 0.5H$ at the wall.

The model considers two external forces on the particle along the wall-normal direction. The first is the wall-normal lift force (*cf.* Eq. 6.1); as noted earlier, $F_\mathrm{L} = O(10^{-2}\ \mathrm{fN})$ based on average experimental values. The other significant force on the particle is the z-component of Stokes drag (*cf.* Eq. 2.7); again, as noted earlier, $D_z = O(10^{-1}\ \mathrm{fN})$.

The z-position of the particle center is then given by Newton's Second Law:

$$m\frac{\partial^2 z}{\partial t^2} = F_\mathrm{L} + D_z \qquad [6.9]$$

or

$$\rho_p \frac{4\pi}{3} a^3 \frac{\partial^2 z}{\partial t^2} = 1.75\pi \frac{\varepsilon |\zeta_p| a^3 \dot{\gamma} E \rho}{\mu} - 6\pi\mu a \frac{\partial z}{\partial t}$$
$$= 1.75\pi \frac{\varepsilon |\zeta_p| a^3 E \rho}{\mu} \frac{1}{\mu} \frac{\partial p}{\partial x} z - 6\pi\mu a \frac{\partial z}{\partial t} \qquad [6.10]$$

where $m = \rho_p (4\pi a^3 / 3)$ is the particle mass and the shear rate $\dot{\gamma} = \frac{1}{\mu} \frac{\partial p}{\partial x} z$, based on the velocity profile for Poiseuille flow between two parallel plates.

Eq. 6.10 can be rewritten as follows:

$$\frac{\partial^2 z}{\partial t^2} = -\frac{9\mu}{2\rho_p a^2} \frac{\partial z}{\partial t} + \frac{21}{16} \frac{\varepsilon |\zeta_p| E \rho}{\mu^2 \rho_p} \frac{\partial p}{\partial x} z \qquad [6.11]$$

Since the fluid properties (ε, ρ_s, μ), the particle properties (a, ρ_p, ζ_p) and the flow parameters E and $\partial p / \partial x$ are constant during the experiments, Eq. 6.11 can be expressed as:

$$\frac{\partial^2 z}{\partial t^2} + \frac{9\mu}{2\rho_p a^2} \frac{\partial z}{\partial t} - \frac{21}{16} \frac{\varepsilon |\zeta_p| E \rho}{\mu^2 \rho_p} \frac{\partial p}{\partial x} z = \frac{\partial^2 z}{\partial t^2} + A \frac{\partial z}{\partial t} + Bz = 0 \qquad [6.12]$$

where the constants $A = \frac{9\mu}{2\rho_p a^2}$ and $B = -\frac{21}{16} \frac{\varepsilon |\zeta_p| E \rho}{\mu^2 \rho_p} \frac{\partial p}{\partial x}$. This second-order differential equation can then be solved for the initial conditions $z(0) = z_o$ (*i.e.*, an initial position of z_o) and $\partial z / \partial t = 0$ at $t = 0$ (*i.e.*, the particle has no initial velocity along the z-direction)) to give:

$$z(t) = z_o \left[\frac{(-A+\beta)}{2\beta} \exp\left\{ -\left(\frac{A+\beta}{2} \right) t \right\} + \frac{(A+\beta)}{2\beta} \exp\left\{ \left(\frac{-A+\beta}{2} \right) t \right\} \right] \qquad [6.13]$$

where $\beta \equiv \sqrt{A^2 - 4B}$. Eq. 6.13 can then be used to determine the time required for a particle to reach the region near the channel wall, *i.e.*, $z(t) \geq R \equiv 0.5H - 3z_p - a$ based on the extent of the region visualized by evanescent-wave illumination. Again, z is the position of the particle center.

Particle simulations in MATLAB were used to estimate the number of near-wall particles over time during the accumulation stage. The simulation starts with a group of 1000 particles evenly distributed along the wall-normal positions $0 \leq z_o \leq R$, *i.e.*, from the centerline to the edge of the near-wall region. Each of the particles represents a group of particles around the same initial wall-normal position which altogether represent all particles in the lower half of the channel. No particles had initial positions within the near-wall region ($z_o > R$) because very few particles were observed in this region in the experiments at t = 0. This lack of near-wall particles is likely due to the wall-normal "hydrodynamic lift" force that drives particles away from the wall in Poiseuille flow (Ranchon *et al*. 2015, Cherukat and McLaughlin 1994). Eq. 6.13 is used to "track" the z-position of these particles over time to determine the time when each particle enters the near-wall region at $z_o > R$ for a given set of flow parameters, namely E and $\partial p / \partial x$, and determine the total number of near-wall particles over time t. Typical simulation results for the fraction of near-wall particles as a function of time $n_w(t)$, namely this number of near wall particles normalized by all the particles in the lower half of the channel based on φ_∞, are shown in Fig. 6.6 for E = 131 V/cm and $\partial p / \partial x$ = 42 kPa/m, corresponding to a near-wall shear rate $\dot{\gamma}_w$ = 730 s^{-1}.

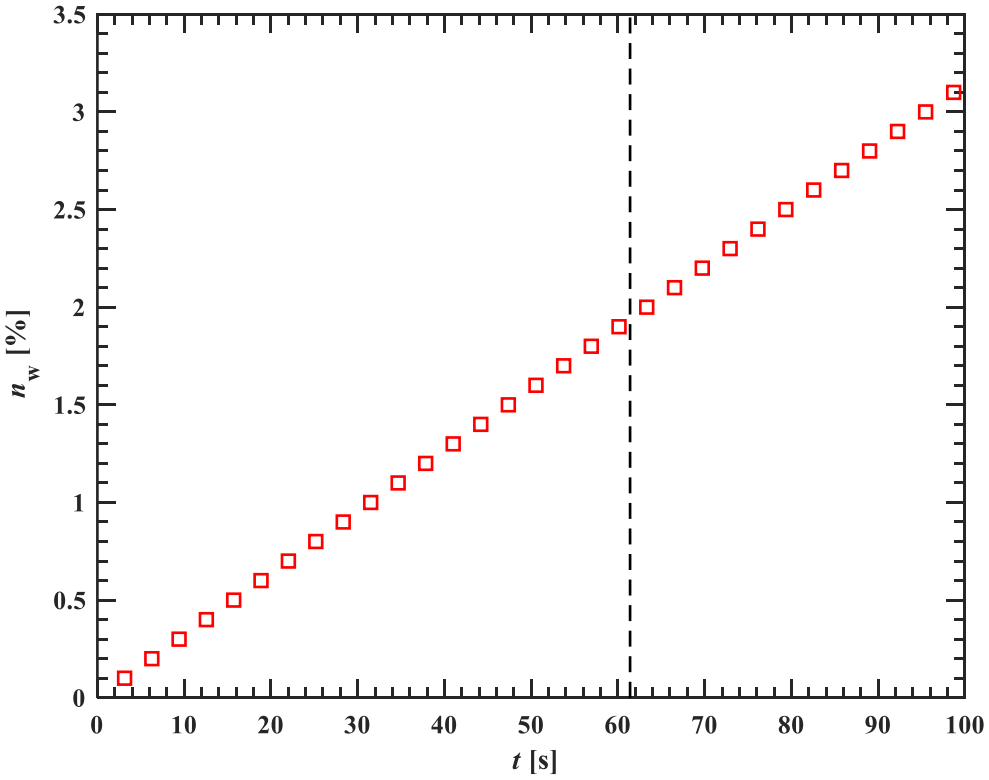

Figure 6.6: Expected fraction of near-wall particles $n_w(t)$ (□) at E = 131 V/cm and $\partial p / \partial x$ = 42 kPa/m (corresponding to $\dot{\gamma}_w$ = 730 s^{-1}). The dashed vertical line denotes the average value of T_o; here, $n_w(T_o)$ = 2.0%.

Table 6.3: $n_w(T_o)$ predicted by the simulations for all six experimental cases where T_o is determined from the average of three or four experimental trials.

$\dot{\gamma}_w$ = 730 s^{-1}		$\dot{\gamma}_w$ = 1760 s^{-1}	
E [V/cm]	$n_w(T_o)$ [%]	E [V/cm]	$n_w(T_o)$ [%]
84	1.5	126	1.9
108	1.6	150	1.8
131	2.0	173	1.7

Since n_w in the illuminated region at T_o has the same order of magnitude for both the simulation and the expected amount from experimental results, this suggests the experimental observations are consistent with a wall-normal lift force of the same order of

magnitude as that given by Eq. 6.1. Assume that the thickness (*z*-extent) of the region of concentrated particles during the accumulation stage is ~6 μm, based upon confocal microscopy images visualizing a cross-section of the channel during the steady-state phase (Lochab *et al.* 2019). Since the thickness (*z*-dimension) of the region illuminated by the evanescent waves is about $3z_p = 0.3$ μm, this suggests that about 5% of the particles concentrated near the wall that assemble into bands are visualized in these experiments. Furthermore, the number of near-wall particles observed at $t = T_o$ in the experiments, or N'_T at $\tau = 1$, is about half the maximum value as shown in Fig. 6.1. The number of near-wall particles observed at T_o should then correspond to $n_w(T_o) \approx 2.5\%$, a value slightly greater than that predicted by the simulations (Tbl. 6.2), indicating that the experimental observations during the accumulation stage are consistent with a wall-normal lift force of $O(10^{-2}$ fN), or the same order of magnitude as that given by the models of Choudhary *et al.* (2019; 2021) and Khair and Kabarowski (2020).

Fig. 6.6 shows that the number of near-wall particles grows linearly over time; a linear curve-fit to the data shown in the figure has $R^2 > 0.99$. The experimental data instead suggests that the growth rate is exponential (*cf.* Sec. 6.1). The linear growth rate predicted by the simulations can be explained by scaling Eq. 6.13, which gives $z(t)$. Let the dimensionless *z*-position of the particle center $z' \equiv z / H$, where H is the depth of the channel, and dimensionless time $t' \equiv t / T_o$ where T_o is the time scale describing the accumulation stage. Then Eq. 6.13 becomes

$$\frac{\partial^2 z'}{\partial t'^2} + \frac{9\mu T_o}{2\rho_p a^2}\frac{\partial z'}{\partial t'} - \frac{21}{16}\frac{\varepsilon\left|\zeta_p\right| E \rho_s T_o^2}{\mu^2 \rho_p}\frac{\partial p}{\partial x} z' = \frac{\partial^2 z'}{\partial t'^2} + A'\frac{\partial z'}{\partial t'} + B' z' \qquad [6.14]$$

For the parameters of Fig. 6.6, namely E = 131 V/cm and $\partial p / \partial x$ = 42 kPa/m, $A' = O(10^9)$ and $B' = O(10^7)$. Given that the coefficients in this scaled equation represent the order of magnitude of each of the terms in this equation, this suggests that the acceleration term, with its coefficient of unity, is negligible over most of the accumulation phase.

This is confirmed by the simulations, which compared the dimensional acceleration with the other two terms in the (dimensional) Eq. 6.14 over $0 < t < 100$ s with a time step of 0.1 s, and found that the acceleration term is at least 12 orders of magnitude less than the other two terms for $t \geq 0.1$ s. Thus, the particle dynamics are quasi-steady during the accumulation stage except at very small times when the particles accelerate from rest. For negligible acceleration, Eq. 6.14 gives:

$$z' = \exp\left\{-\frac{B'}{A'}t\right\} \approx 1 - \frac{B'}{A'}t \qquad [6.15]$$

for $B'/A' \ll 1$, which is the case here. Since the z-position of the particle increases linearly with time, the z-component of the particle velocity is constant, and so the number of particles reaching the near-wall region will grow linearly with time for an ensemble of particles evenly distributed along the z-direction.

The discrepancy between the exponential (*vs.* linear) growth rate observed in the experiments at a given x location may be due to wall (*i.e.*, hindrance) effects. First, the experiments only visualize particles with centers within $3z_p$, or 330 nm, of the wall, or at $z > 0.5H - 330$ nm, while wall-normal lift force models considers a single particle suspended in a flow with constant shear rate. The lift force given by Eq. 6.1 may therefore not be valid for particles within a few radii of the channel wall. Second, the lift force models assume that $Re << 1$, *i.e.*, fluid inertia is negligible. In these experiments, $Re \leq 1$.

Moreover, the simulation assumes that the particles, once they reach the near-wall region remain within this region, which may not be the case due, for example, to Brownian diffusion. A particle of radius a = 245 nm will have a rms displacement based upon the Stokes-Einstein equation of $3z_p$ = 330 nm, or the thickness of the region illuminated by the evanescent wave, over a time interval of 60 ms. Although the Stokes-Einstein equation ignores wall effects and overestimates anisotropic near-wall Brownian diffusion, particles have a greater probability to diffuse away from, *vs*. towards, the wall, and hence to leave the near-wall region. Finally, the simulation assumes that the particles, once they accumulate near the wall, are uniformly distributed over z, which is unlikely given repulsive particle-wall EDL interactions and van der Waals effects.

Section 6.4: Particle Velocities in the Streamwise (x) Direction

In the previous section, the positions of individual tracer particles were determined from a sequence of particle images over time. The two particle velocity components in the x-y plane, *i.e.*, the plane parallel to the wall, can then be estimated from the change in a particle's position over subsequent images. In this section, the near-wall particle velocity component along the streamwise (x) direction, U_p, estimated from the experiments will be compared with the expected near-wall particle velocity U_p^{XW}.

The flow velocity near the channel wall U_f for this low-*Re* flow is expected to be the superposition of the Poiseuille flow velocity U_{po} and electroosmotic (EO) flow velocity U_{eo} which is discussed in Sec. 2.5 and expressed in Eq. 2.13. The Poiseuille flow is defined to be along the positive x-direction, so U_{Po} is positive, while U_{eo} is negative because $\zeta_w <$ 0 in these experiments. For the parameters in Tbl. 6.2, U_f is negative for small z, then

becomes positive farther from the wall, as shown by the red dotted line in Fig. 6.7. Since the Debye length is ~7 nm, Eq. 2.13 should be valid for $z > 10$ nm.

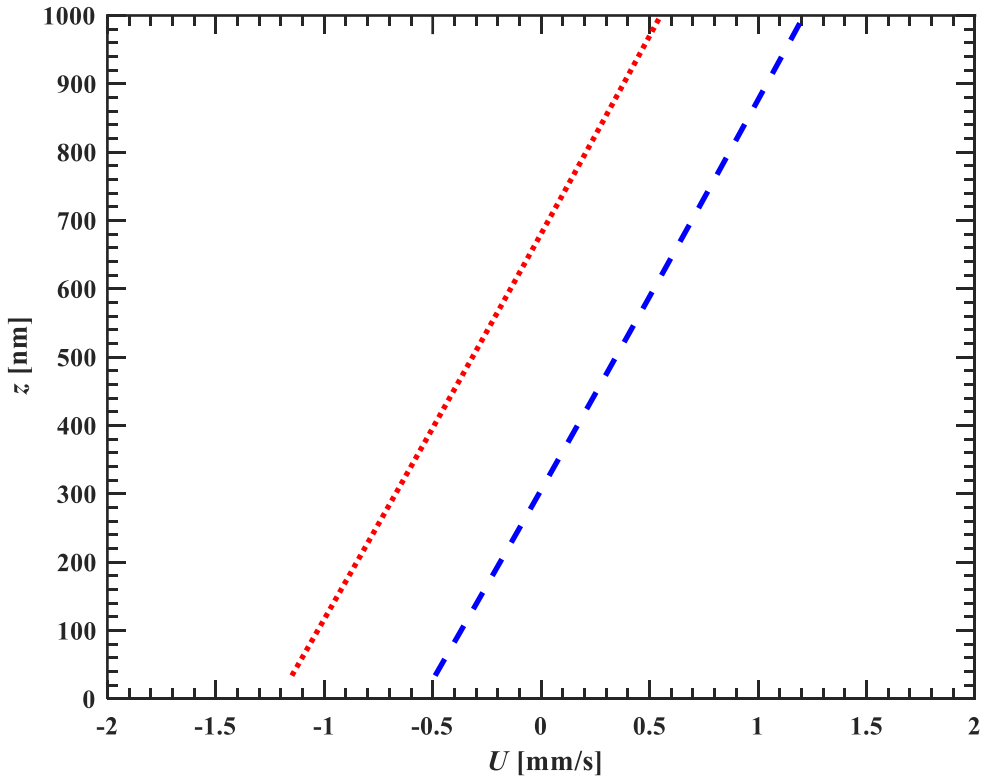

Figure 6.7: Expected flow (*red dotted line*) and particle (*blue dashed line*) velocities as a function of z from Eq. 2.13 and 2.15 respectively for E = 150 V/cm, dP/dx = 102 kPa/m (corresponding to $\dot{\gamma}_w$ = 1760 s^{-1}), ζ_w= −110 mV and ζ_p = −60 mV.

As discussed in Sec. 2.5, the expected particle velocity U_p^X should then be simply the superposition of U_f and the electrophoretic velocity of the particle U_{ep}:

$$U_p^X = U_{po} + U_{eo} - U_{ep} \approx \dot{\gamma} z + \frac{\varepsilon E \zeta_w}{\mu} - \frac{\varepsilon E \zeta_p}{\mu} \qquad [6.16]$$

Since $\zeta_p < 0$ in these experiments, $U_p^X > U_f$, as shown by the blue dashed line in Fig. 6.7.

However, Eq. 6.16 does not consider wall effects. Specifically, the velocity of a particle in a flow with a constant and nonzero shear rate near a planar wall will be reduced

because the particle will experience a hydrodynamic torque, and hence some of its kinetic energy will go into rotation, *vs.* translation. As discussed in Sec. 2.5, Goldman *et al.* (1963) modeled a spherical particle suspended in constant shear flow near a wall (in the absence of an electric field) and determined the particle velocity along the flow (x) direction as $G_w \dot{\gamma}_w z$ where $G_w \leq 1$, decreases with z, and $G_w = 1$ when wall effects are negligible. Tbl. 2 of Goldman *et al.* (1963) lists G_w for various values of z/a and will be used in Eq. 6.25 to estimate values for G_w in the illuminated region using linear interpolation.

The electrical potential field will also be asymmetric around the particle, and "distorted" in the gap between the particle and the wall. As discussed in Sec. 2.5, Keh and Chen (1989) and Yariv and Brenner (2003) modeled a spherical particle under a DC electric field near a wall and both expected an increase in particle electrophoretic mobility by ~23% for a particle nearly touching the channel wall, specifically when the ratio of the to the particle-wall "gap" to the particle radius, or h/a, was 0.995. On the other hand, a more recent model by Unni *et al.* (2007) modeled a spherical particle bounded by two parallel walls. Fig. 3 of Unni *et al.* (2007) show the ratio of the modeled particle velocity to that given by the Smoluchowski equation as a function of a/D_C and $D_F/(D_F + D_C)$ and predicts up to a ~40% increase. However, in the illuminated region, $0.4 < a/D_C < 1$, and $D_C/(D_C + D_F) < 0.02$, thus the expected increase in particle electrophoretic mobility using that table is ~23% which has good agreement with Keh and Chen (1989) and Yariv and Brenner (2003).

Although the wall has an effect on both near-wall shear flow and electrophoresis, wall effects on electrophoresis are significant over a much smaller (shorter) range than those due to shear flow. Indeed, wall effects are negligible, defined as having less than a

1% effect on the particle electrophoretic velocity, for $z > 310$ nm, while wall effects on the particle velocity due to shear flow have less than a 1% effect only for $z > 630$ nm. Given that the experiments consider particles with centers at 255 nm $< z <$ 575 nm, the near-wall effect on particle electrokinetics was considered negligible here.

Finally, interparticle forces could also affect U_p^X, but they should be negligible during most of the accumulation stage (except shortly before the end of this stage), based on the interparticle spacing estimates discussed in Sec. 6.2. The expected near-wall particle velocity U_p^{XW}, including wall effects, during most of accumulation is therefore

$$U_p^{XW} \approx G_w \dot{\gamma}_w z + \frac{\varepsilon E(\zeta_w - \zeta_p)}{\mu} \qquad [6.17]$$

As noted earlier, the scattering of the red-shifted fluorescence (excited by the evanescent-wave illumination), especially in the latter stages of accumulation and beyond when near-wall particle concentrations exceed 0.1, makes it unlikely that the brightness of the particle image will, like the evanescent-wave illumination, decay exponentially with z / z_p (*cf.* Eq. 3.4). No attempt was therefore made to estimate the *z*-position of the particle velocities, although the brightness of the particle images should still decrease with increasing wall-normal distance *z*. Instead, a histogram of the particle velocities estimated in these experiments U_p are compared with the range of expected particle velocities U_p^{XW} based on Eq. 6.17 (for $a + 10 \text{ nm} < z < a + 3z_p$). For these histograms, the U_p values obtained over a 1 s interval were separated into 100 velocity bins, each with a width of 0.02 mm/s, ranging from a velocity of –1 mm/s to 1 mm/s, and the number of velocity samples in each bin is normalized by the total number of velocity samples.

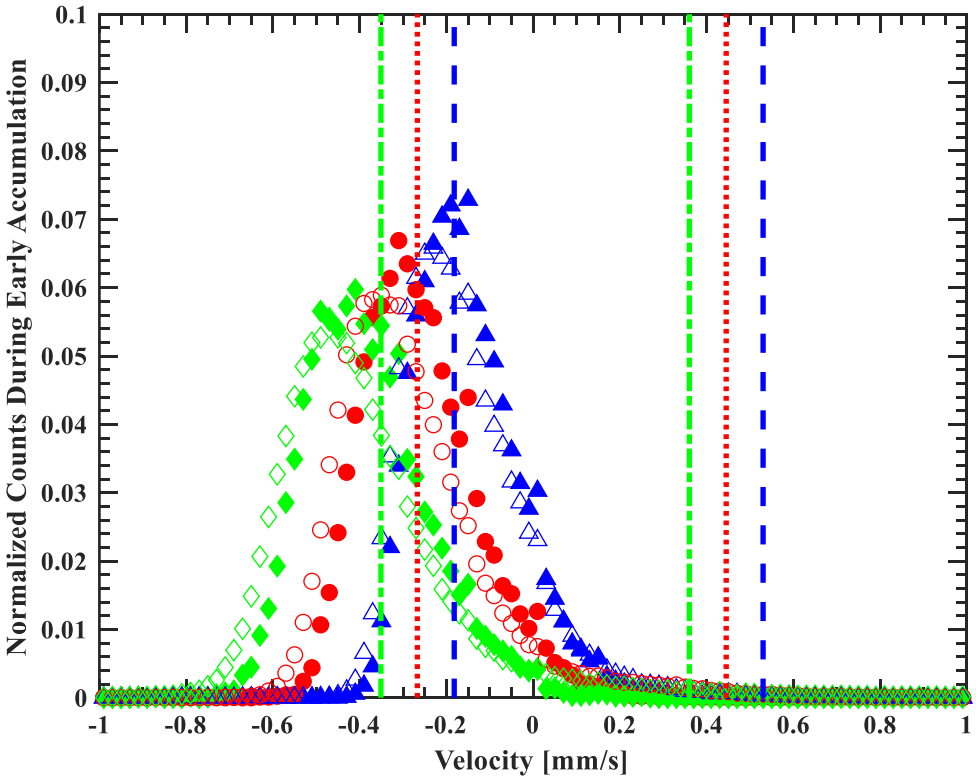

Figure 6.8: Histogram of near-wall particle velocities along the streamwise direction U_p during the accumulation phase for t = 5–6 s (*closed symbols*) and t = 15–16 s (*open symbols*) at $\dot{\gamma}_w$ = 1760 s^{-1} for E = 126 V/cm (▲), 150 V/cm (●) and 173 V/cm (■). The vertical lines represent the range of expected particle velocities U_p^{XW} for E = 126 V/cm (*dashed lines*), 150 V/cm (*dotted lines*) and 173 V/cm (*dashed-dotted lines*).

Fig. 6.8, which shows a histogram of particle velocities both near the beginning (t = 5–6 s after applying the electric field) and near the end (t = 15–16 s) of the accumulation stage (t < 25 s), shows that U_p is significantly less (*i.e.*, more negative) than U_p^{XW}. Interparticle effects should be negligible for these data, since the average interparticle spacing is 82a for t = 5–6 s, and 26a for t = 15–16 s.

One possible explanation for the discrepancy between U_p and U_p^{XW} is that the particle electrophoretic velocity is less than the value given by the Smoluchowki equation, *i.e.*, near-wall particle electrophoresis is suppressed. If so, however, this reduction is the

opposite of the enhancement predicted by the models of Keh and Chen (1989), Yariv and Brenner (2003), and Unni *et al.* (2007).

The amount of near-wall electrophoretic suppression can be estimated by comparing the particle velocity U_p^M at the peak of the histogram with the average expected particle velocity based on Eq. 6.25. This average expected particle velocity:

$$\overline{U}_p^{XW} = \underbrace{\frac{\dot{\gamma}_w}{2}\left[G_{min}(a+10\text{ nm}) + G_{max}(a+3z_p)\right] + \frac{\varepsilon E}{\mu}\zeta_w}_{\text{flow velocity}} - \frac{\varepsilon E}{\mu}\zeta_p \qquad [6.18]$$

where G_{min} and G_{max} are the factor G_w (from Goldman *et al.* 1963) at $z = a + 10$ nm and $z = a + 3z_p$, respectively. Assuming that U_p^M and $\overline{U}_p^X$ have the same flow velocity, this near-wall electrophoretic suppression can be expressed as the ratio of the electrophoretic mobility estimated from U_p^M to that predicted by the Smoluchowski equation as:

$$Z_r = \frac{\mu}{\varepsilon E \zeta_p}(U_p^M - \overline{U}_p^{XW}) \qquad [6.19]$$

Using Eq. 6.19 for the three histograms during the early accumulation stage (t = 5–6 s) shown in Fig. 6.8, Z_r = 0.31–0.59.

The particle velocity U_p also appears to decrease slightly, *i.e.*, the histogram shifts to more negative velocities, over time during the accumulation phase for all cases in Tbl. 6.1. Since the expected particle velocity is a function of z and becomes more negative closer to the channel wall, the average z-position of the particles may decrease slightly during the accumulation stage as more particles are attracted to the wall and assemble into bands.

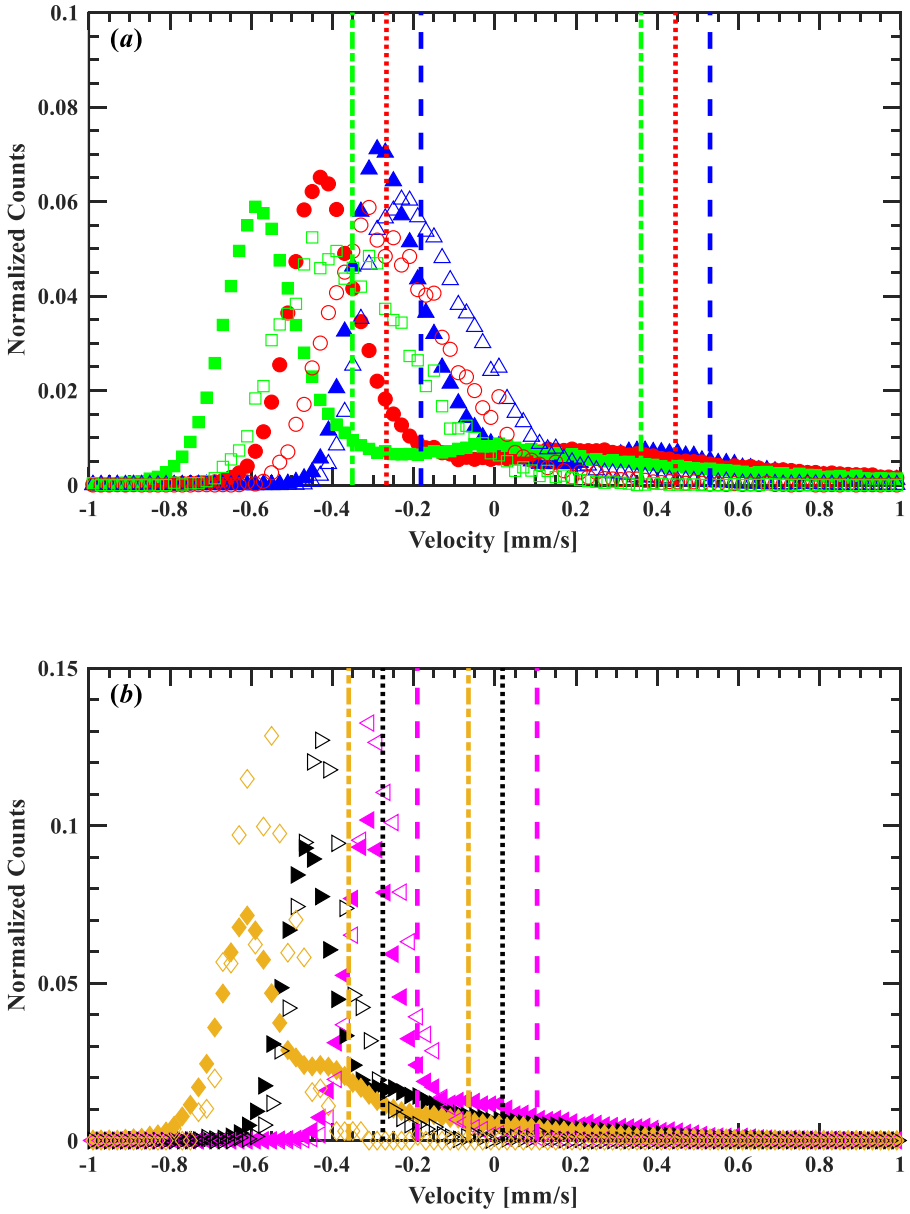

Figure 6.9: Histogram of near-wall particle velocities along the streamwise direction U_p during the steady-state phase at (*a*) $\dot{\gamma}_w$ = 1760 s^{-1} for *E* = 126 V/cm (▲), 150 V/cm (●) and 173 V/cm (■) for particles inside the bands (*filled*) and outside the bands (*open symbols*). The vertical lines represent the range of expected near-wall particle velocities U_p^{XW} for *E* = 126 V/cm (*dashed*), 150 V/cm (*dotted*) and 173 V/cm (*dashed-dotted lines*) and (*b*) $\dot{\gamma}_w$ = 730 s^{-1} for *E* = 84 V/cm (◀), 108 V/cm (▶) and 131 V/cm (♦) for particles inside the bands (*filled*) and outside the bands (*open symbols*). The vertical lines again represent the range of expected particle velocities U_p^{XW} for *E* = 84 V/cm (*dashed*), 108 V/cm (*dotted*) and 131 V/cm (*dashed-dotted lines*).

Fig. 6.9 shows particle velocities inside the bands (*filled symbols*) and outside the bands (*open symbols*) at steady-state (*vs.* accumulation). The U_p histogram for particles inside the bands is bimodal, with a large peak of negative velocities, and a smaller, broader peak of positive velocities. On the other hand, the U_p histogram for particles outside of the bands has a single peak of negative velocities slightly to the right of (*i.e.*, more positive than) the large peak in U_p for particles within the bands. Note that the number of samples for particles outside the bands is typically an order of magnitude less than for particles inside the bands, since the vast majority of the particles are inside the bands during the steady-state phase. As shown by Fig. 6.10, the U_p histograms for particles outside the bands is similar to that for the early accumulation stage (t = 5–6 s), suggesting that particle velocity distributions are consistent when the interparticle spacing exceeds 44a.

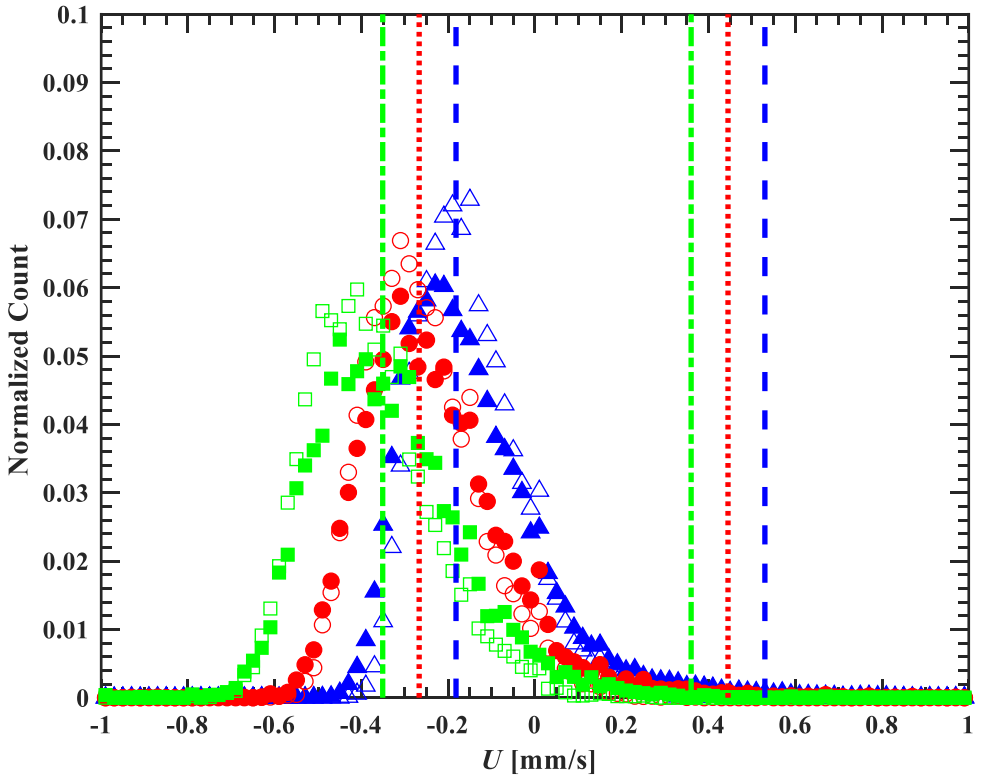

Figure 6.10: Similar to the previous histograms shown in the previous two figures but for particle velocities U_p during the steady-state stage (*filled symbols*) and the early accumulation (t = 5–6 s) stage (*open symbols*) for $\dot{\gamma}_w$ = 1760 s^{-1} for E = 126 V/cm (▲), 150 V/cm (●) and 173 V/cm (■). The vertical lines represent the range of expected particle velocity for E = 126 V/cm (*dashed*), 150 V/cm (*dotted*) and 173 V/cm (*dashed-dotted lines*).

Lastly, U_p histograms during the steady-state phase were compared at different $\dot{\gamma}_w$ and E to investigate how flow parameters affect the particle velocities. Figs. 6.8 and 6.9 shows E affects the velocity histograms at steady-state at a given $\dot{\gamma}_w$. As E increases, the histogram peak becomes more negative (*i.e.*, shifts to the left), qualitatively consistent with what would be expected for U_p^{XW}. Furthermore, both the particle velocity at the peak of the histogram U_p^M and the half-width of the peak in U_p can be estimated from a Gaussian curve-fit to the left half of the peak (only the left half was used because the U_p

distribution appears to be asymmetric). Fig. 6.11 shows U_p^M as a function of E for particles inside and outside the bands. The velocity at the peak of the histogram for both particles inside and outside the bands is a linear function of E, which is qualitatively consistent with Eq. 6.18; $R^2 > 0.99$ for linear curve-fits in all cases except for the velocities of particles outside the bands in Fig. 6.11*b* where $R^2 = 0.975$.

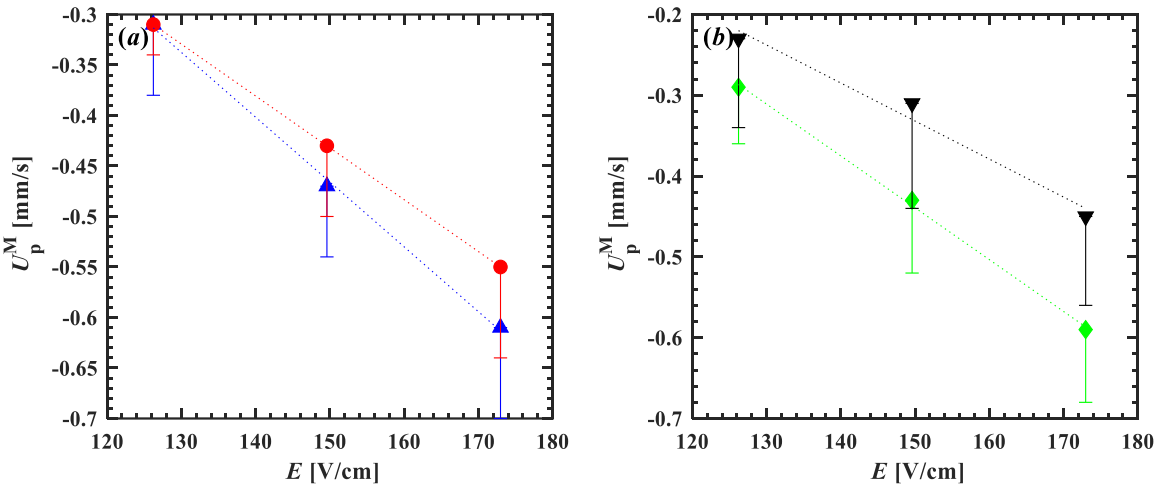

Figure 6.11: The velocities along the streamwise direction at the peak maximum U_p^M as a function of electric field magnitude E during the steady-state stage at (*a*) $\dot{\gamma}_w$ = 730 s^{-1} for particles inside (▲) and outside (●) the bands and at $\dot{\gamma}_w$ = 1760 s^{-1} for particles inside (♦) and (▼) outside the bands. The dotted lines represent linear curve fits while the error bar represents the half-width (obtained from a Gaussian curve-fit to the left half of the peak).

Although this strongly suggests the particle velocities are influenced by electrophoresis and/or electroosmosis, the slopes of these linear curve-fits were on average 0.013 mm^2/(V ·s), *vs.* a slope of $\varepsilon(\zeta_w - \zeta_p)/\mu = 0.031 \pm 0.005$ mm^2/(V ·s) based on Eq. 6.25. Assuming that the fluid properties are constant, this suggests that $(\zeta_w - \zeta_p)$ is less than the measured values for the wall and particle zeta-potentials. Moreover, assuming that the flow velocity, including that for EO flow, is the expected value, this result suggests that

the electrophoretic mobility, which would be $\varepsilon\zeta_p/\mu$ by the Helmholtz-Smoluchowski equation, is significantly reduced.

Fig. 6.12 shows how the histograms of U_p inside the bands changes with $\dot{\gamma}_w$ at a given E. Note that these are the only data, where E is roughly constant for different $\dot{\gamma}_w$.

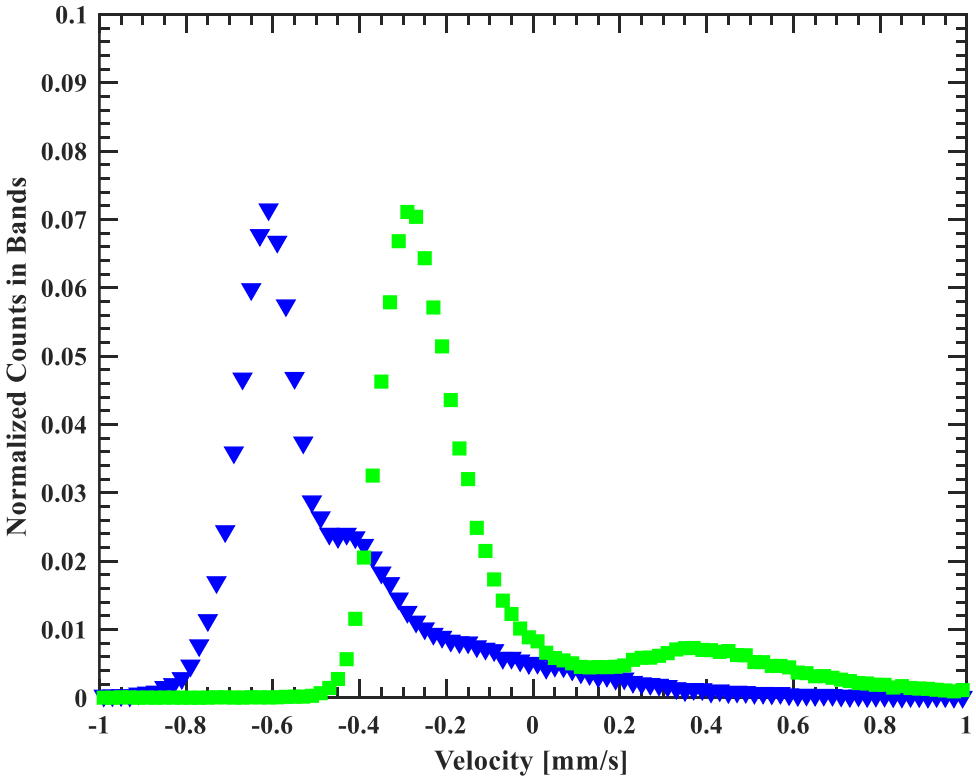

Figure 6.12: Histogram of U_p during the steady-state stage for particles inside the bands at $\dot{\gamma}_w$ = 730 s^{-1} and E = 131 V/cm (▼), and at $\dot{\gamma}_w$ = 1760 s^{-1} and E = 126 V/cm (■).

The range of flow, and hence particle, velocties should increase with shear rate, based on Eq. 6.25. The half-width of the major peak in the histograms was therefore used to estimate of the observed particle velocity range. Assuming that the histograms only show the velocities of particles over the same region, *i.e.*, over the same range of z, a broader peak corresponds to broader range of observed particle velocities, and this range

should increase with $\dot{\gamma}_w$. In Fig. 6.11, the half-width of the peak in the particle velocity histogram increases from 0.16 mm/s to 0.20 mm/s, or by 25%, as $\dot{\gamma}_w$ increases from 730 s^{-1} to 1760 s^{-1}. However, an increase of 140% would be expected from Eq. 6.25, which suggests the range of particle velocities over $a + 10\text{ nm} < z < a + 3z_p$ changes from 0.29 mm/s to 0.70 mm/s as $\dot{\gamma}_w$ increases from 730 s^{-1} to 1760 s^{-1}. This mismatch could be due the model assumpion that all particles have the same a and ζ_p.

Finally, the brightness of the particle image was investigated to see if there was any correlation between U_p and the particle image intensity. While the exact z-position of a particle cannot be easily estimated due to scattering, brighter particles, as estimated by the sum of all pixel grayscales that comprise a particle, should have a smaller z, *i.e.*, be closer to the channel wall, than dimmer particles.

Fig. 6.13 illustrates that brighter particles have larger velocity magnitudes (although the velocities themselves are along the $-x$ direction) for a single case at steady-state within the bands, in agreement with Eq. 6.17. Although results are not shown, this correlation between brighter particles and larger velocity magnitudes was consistent for all experimental cases.

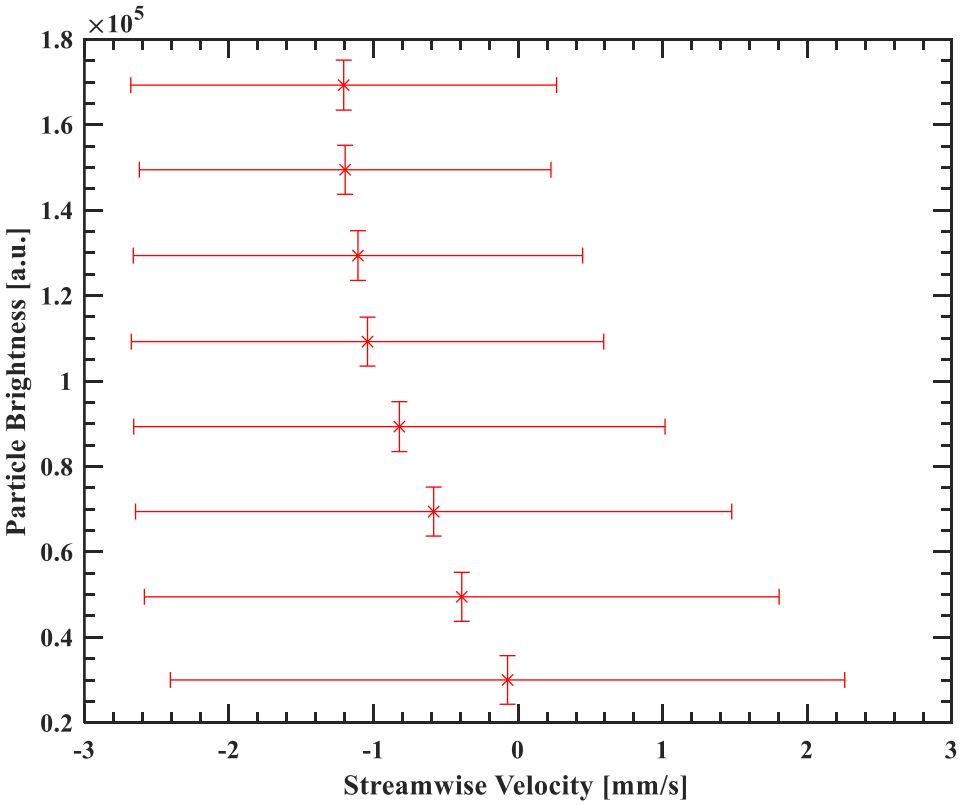

Figure 6.13: Near-wall particle velocities along the streamwise direction during the steady-state phase within the bands against particle brightness for a single trial at $\dot{\gamma}_w$ = 1760 s^{-1} and E = 126 V/cm. These data were taken for φ_∞ = 0.33% over 1 s (499 pairs). The vertical and horizontal error bars denote the standard deviations in particle brightness and streamwise velocity, respectively for each bin; only bins with more than 500 samples are included. The data shown here comprise 96% of the total samples.

Section 6.5: Particle Cross-stream Velocities during Band Formation

Particle velocities along the transverse, or *y*-, direction V_y were also examined just before the end of the accumulation stage to study whether the bands are primarily formed by particles that have been attracted to the channel wall and are then entrained along the transverse direction into bands, as opposed to particles that are entrained along the wall-normal direction into the bands from the bulk. If the bands are formed from near-wall particles, then it is conjectured that there should be a significant transverse velocity on either side of the band towards the band center as it forms.

V_y was estimated over the period $T_o - 5s < t < T_o + 5s$ at a frequency of 1 Hz in the vicinity of a stable (*i.e.*, fairly stationary) band. The "exact" position of the band center is taken to be that at $t = T_o + 3s$; as detailed in Chapter 4, the band center position and width are defined based on a threshold before band formation. The regions on either side of the band are then assumed to be 6 μm, or 19 pixels, below the lower, and above the upper, edges of the band, which were taken to be a half-width below and above, respectively, the center of the band. Fig. 6.14 shows an example of the cross-stream velocities on both sides of a band near the end of the accumulation stage at $t = T_o - 3s$.

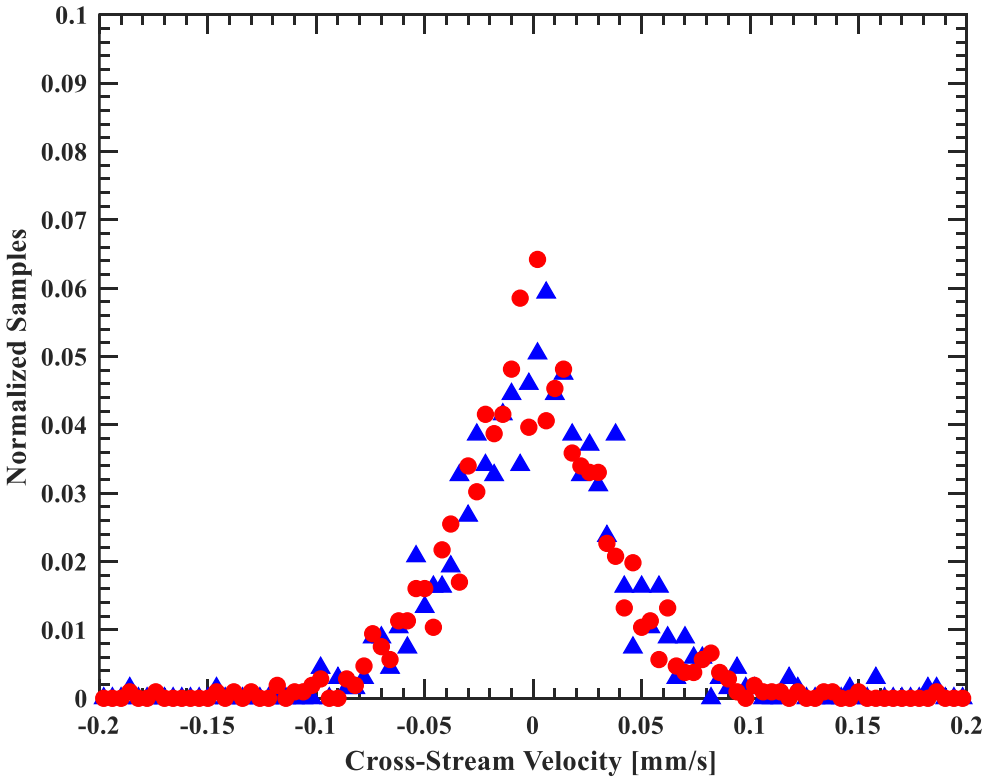

Figure 6.14: Histogram of near-wall particle velocities along the cross-stream direction V_y at $t = T_o - 3s$. (*i.e.*, near the end of the accumulation stage, where $T_o = 24.7$ s) at $\dot{\gamma}_w = 1760\ s^{-1}$ and E = 126 V/cm; T_o = 24.7 s. The figure shows two histograms of V_y over a region with a y-extent of 6 mm above the upper edge (▲), and below the lower edge (●), of a band that forms a few seconds later.

The symmetry of the cross-stream velocities around 0 mm/s in Fig. 6.14 suggests that there is little evidence that the near-wall particles are drawn into the band along the cross-stream (y) direction. This result implies that the particles that make up the band come, for the most part, from the bulk of the channel, or the particles near the channel wall visualized by evanescent-wave illumination migrate into the bands over several seconds, *i.e.*, over an interval significantly greater than the interval shown here.

CHAPTER 7
COUNCLUSIONS AND RECOMMENDATIONS

Section 7.1: Thesis Summary

This thesis details an experimental study of a type of colloidal assembly, called banding, and the resulting structures, called bands where the bands and tracer particles within the bands are visualized using evanescent-wave illumination. As a reminder, the objectives of this thesis are, first, to: 1) to develop a consistent method for determining band characteristics, such as how long they take to form and the spacing between them, and to track particle positions and dynamics 2) to determine how band characteristics and particle velocities change under different flow or particle parameters such as E, $\dot{\gamma}_w$ or a, and 3) study the fundamental phenomena that cause banding using four conjectures explained below.

In addition, the following conjectures have been tested with the results from this thesis:

1. Band formation occurs when the spacing between particles in the near-wall region decreases below a critical value, or, alternatively, the concentration of particles in the near-wall region exceeds a critical value.
2. The wall-normal force predicted by the results of Choudhary *et al*. (2019; 2021) and Khair and Kabarowski (2020), is the major cause for particle migration towards the channel wall during the accumulation stage.
3. The time scales for band formation scale with those for the flow, namely the inverse of the shear rate.

4. The particle velocities are the superposition of the Poiseuille and Smoluchowski electroosmotic flow velocities and the Smoluchowski electrophoretic velocity.

To accomplish these objectives, various combinations of Poiseuille and electroosmotic counterflow were tested over a range of E, $\dot{\gamma}_w$, φ_∞, a and x to determine the conditions under, and locations where, near-wall particles assemble into bands. Particle dynamics during band formation were visualized using evanescent-wave illumination (under conditions where particles assembled into bands) and recorded over time. As detailed in Sec. 1.3, band formation appears to consist of three stages: 1) accumulation; 2) band formation; and 3) steady-state. These image sequences were analyzed in MATLAB R2019b to determine band characteristics such as the time for the first band to form T_o, which is defined to be the end of the accumulation stage, and the number of bands over the field of view in the region of interest, N, in the steady-state phase.

Since the particles are too closely spaced to distinguish individual particles starting near the end of the accumulation stage, individual particle dynamics were also studied by evanescent-wave visualizations of tracer particles, which were 1% of the total particles, during accumulation and inside and outside the bands during steady-state. These visualizations were used to estimate particle velocites along the streamwise (x) and transverse (y) directions, as well as the number of near-wall tracer particles over time. The increase in the number of particles during the accumulation stage was compared with recent model predictions of a wall-normal lift force. The measured streamwise velocities were compared with the expected velocity, namely the superposition of the flow and particle electrophoretic velocities.

Section 7.2: Conclusions

The conclusions that are drawn from this work are that:

1) Bands only form when a minimum electric field E, called E_{min}, is exceeded for a given set of all other properties, including the near-wall shear rate $\dot{\gamma}_w$. It appears in some cases that bands only form above a minimum near-wall shear rate, but experimental difficulties in accessing low shear rates precluded determining this minimum shear rate over much of the parameter space studied here.
2) This E_{min} increases as $\dot{\gamma}_w$ increases under otherwise identical experimental conditions.
3) Banding is observed over a smaller portion of the E– $\dot{\gamma}_w$ parameter space, at least over the range of E and $\dot{\gamma}_w$ studied here, as the bulk particle volume fraction φ_∞ and particle radius a increase under otherwise fixed experimental conditions.
4) Bands form downstream of, or after, a certain streamwise position in the channel, x_o. However, when comparing two locations where bands form under otherwise identical conditions, band formation occurs earlier in upstream positions than downstream positions.
5) The time scale that denotes the end of the accumulation stage, T_o, varies with the electric field offset ΔE, $\dot{\gamma}_w$, φ_∞ and a. T_o appears to decay exponentially with ΔE. The timescale also decreases as φ_∞ and a increase under otherwise identical experimental conditions. In particular, T_o appears to scale with $1/\dot{\gamma}_w$ for a broad range of $\dot{\gamma}_w$ = 730 s^{-1} to 1760 s^{-1}, ΔE < 100 V/cm, a = 245 nm – 355 nm, ζ_p = −44 mV to −53 mV, and φ_∞ = 0.17% to 0.33% as described in Figs. 5.4 to 5.6.

This suggests that convection due to the shear flow plays a major role in band formation.

6) Since bands form above a minimum E and $\dot{\gamma}_w$ and form earlier at higher E and $\dot{\gamma}_w$, this suggests that the wall-normal force that drives accumulation depends upon, and increases with, these two parameters. This is consistent with models of the wall-normal lift force predicted by Choudhary *et al.* (2019; 2021) and Khair and Kabarowski (2020). However when the magnitude of the particle zeta potential increases, bands take longer to form which is the opposite of the expected behavior.
7) Bands also appear to form above a minimum φ_∞ and earlier at higher φ_∞. However, they appear to form later as a increases at a given φ_∞. These observations suggest that bands form above a near-wall particle concentration, *vs.* a near-wall volume fraction.
8) The spatial period of the bands, which is proportional to the inverse of the number of bands observed over a given field of view, or N_s^{-1}, increases linearly with ΔE and also increases with a at a given φ_∞. This period appears to be independent of φ_∞, however. Finally, the steady-state number of bands N_s itself grows linearly with $\dot{\gamma}_w$.
9) The number of near-wall (tracer) particles grow exponentially over time during the accumulation stage, increasing more than 100-fold. This suggests that the near-wall volume fraction exceeds 15 vol% by the end of the accumulation stage.
10) The data for particle counts during the accumulation phase under different E collapses as time is normalized by T_o as shown in Fig. 6.3 which suggests that there is a critical particle concentration required for band formation.

11) The particle velocities differ significantly from the expected velocities, namely the superposition of the shear and EO flow velocities, and the particle electrophoretic velocity. Specifically, the particle velocities estimated in these experiments is more negative than the expected velocity, even after the shear flow has been corrected for near-wall effects. If the flow velocity remains the superposition of the shear and EO flow velocities, this suggests that wall effects suppress particle electrophoresis, which contradicts model predictions.

12) The velocities of (tracer) particles at the peak of the velocity histograms during the accumulation stage and outside the bands at steady-state vary linearly with the change in the applied E. This is consistent with the EO flow and particle electrophoretic velocities being proportional to E, as predicted by the Smoluchowski equation.

13) The length of the accumulation stage, or T_o, appears to be of the same order of magnitude for most of the particles in half the channel to be attracted to the near-wall region if the particles are subject to the wall-normal lift force predicted by Choudhary *et al.* (2019; 2021) and Khair and Kabarowski (2020) and Stokes drag (along the wall-normal direction). However, the near-wall particle growth rate given by this model during accumulation is linear over time; that observed in the experiments appears to be exponential over time.

14) Measurements of the particle velocities along the transverse direction just before the end of the accumulation stage do not suggest that near-wall particles adjacent to the band are entrained, or migrate, into the bands as they form. This suggests that most of the particles that form the bands are from the bulk, although the

temporal resolution of the imaging system may also be insufficient to resolve these particle velocity components.

Section 7.3: Contributions

Although some of the conjectures were contradicted by the data and some conclusions are tentative due to a lack of evidence, there are a group of contributions that are strongly supported in this thesis.

I) The first is that band formation is "robust", *i.e.*, occurs under a wide range of parameters. This is supported since band formation was found to occur over a range of particle concentrations, particle sizes, particle zeta potentials, band formation was found to occur and in all of these cases a minimum electric field was observed. In most, but not all cases, a minimum shear rate was observed

II) In all observed cases, band formation was found to have three stages:

1) Accumulation
2) Band formation
3) Steady state

III) During the accumulation stage:

The duration of the accumulation stage, characterized by the time for first band to form T_o, was found to depend strongly on flow parameters. For example, T_o was inversely proportional to the applied pressure gradient, which was true over a range of φ_∞, a, ζ_p,

although above a minimum φ_∞. In addition, T_o decays exponentially with applied electric field gradient which was verified over a range of φ_∞, a, ζ_p

The particle count increased exponentially by about 100–200. Assuming the particle volume fraction near the wall starts at the bulk value, particle volume fractions were seen to increase as high as 15% to 25%. The exponential growth rate of particle count over time was confirmed to fit an exponential function of the form $a \exp(b N_T) + c$ using RMSE. The growth rate was also compared to but fit worse than a power law function of the form $a N_T{}^b + c$ for b = 1 to 4. This result was verified over a range of E and $\dot{\gamma}_w$.

Particle streamwise velocities were more negative than expected. This was confirmed by looking at histograms in the illuminated region which had a single peak which became more negative as time passes. Due to this behavior, assuming particle velocity in early accumulation stage is not affected by interparticle forces and that fluid velocity is a combination of near-wall shear and Smoluchowski EOF, the difference in experimental peak and middle of expected velocity range implies that electrophoretic mobility was reduced by a factor of 0.4 to 0.7. This behavior was consistent over a range of E and $\dot{\gamma}_w$.

IV) For band formation:

The number of near-wall particles continues to grow over time after T_o, reaching a maximum of about 200 times the initial value. This result was verified over a range of E and $\dot{\gamma}_w$.

V) For steady state:

The number of near-wall particles becomes roughly constant, and comparable to the value at the end of the accumulation stage. Moreover, N_T at the band formation timescale, T_o, was similar to the steady-state value. A constant value of N, Ns was also observed. As for the histograms for the particle streamwise velocities, the histograms for particles within the bands was bimodal with a secondary positive peak. The histogram for the velocities between the bands had a single peak. Similar to the accumulation stage, the observed particle velocity was also more negative than expected.

Section 7.4: Potential Applications

There are two potential applications for banding that are particularly appealing. The first is the ability to drive particles of this size, which are smaller than those typically done with inertial focusing to the channel wall through counterflow which can be used for further analysis or extraction. In an overview paper on inertial focusing in microfluidics, Martel and Toner (2014) described a range of ratios between particle radius to hydraulic diameter, a/D_H, in many microfluidics studies. These values lie within the range 0.01–1, which are larger than those discussed in this thesis, $a/D_H = 0.004$. Attracting particle to the channel wall is also practical since many sensors and/or actuators are bonded to the channel wall.

The other application is the extraction of these bands for a high throughput method to assemble a steady supply of novel nanomaterial with a very high aspect ratio. There is a study on this topic; Prakash and Lochab (2018) discussed "printing" bands onto a porous polycarbonate membrane in a conference presentation using a microchannel nozzle to

deposit the structures. For both of these potential applications, the results on T_o and N_s under different flow and particle solution properties in this thesis can be applied to form bands in the desired number/spacing in a timely fashion.

Section 7.5: Recommendations for Future Work

There remain several unresolved questions about band formation. Based on the confocal microscopy results from Lochab *et al.* (2019) and Rossi *et al*. (2019), the bands exist within the first 6 μm next to the wall, and therefore extend much farther from the channel wall than these evanescent-wave visualizations, which only observe the first 0.5 μm next to the wall. Visualizations of the entire band cross-section would be valuable; although confocal microscopy can provide such visualizations, the (lack of) temporal resolution of this technique may make it impractical to clarify particle dynamics during the accumulation and band formation stages.

There remains little, if any, fundamental understanding of the presumably interparticle forces that drive band assembly and determine the length scales of band assembly, namely the diameter and cross-stream spacing of the bands. Previous literature, discussed in Chapter 2, does explain the mechanisms for pearl chain formation. It is likely that interparticle forces, which are significant above a minimum particle concentration or below a minimum interparticle spacing, are the major mechanisms that drive banding.

Lastly, there are many aspects of the bands that remain uncharacterized. Although there are some observations of the cross-sectional dimension of the bands, it is unclear how this dimension depends upon E, $\dot{\gamma}_w$, φ_∞ and a. Moreover, although this work has characterized the time scale for the accumulation stage, the time scale for the

beginning of the steady-state stage, or the end of the band formation stage, and how it depends upon various experimental parameters, is largely undetermined.

Future work may also be done with heterogeneous assembly using two or even more types of particles with different properties. Studies on this type of assembly is common, such as Liu and Reifsnider (2013) who studied hetereogeneous mixtures of elliptical particles and the effect orientation and anisotropy would have on properties such as local charge distribution, force, and torque. Preliminary experiments of the solutions discussed in in Tbl. 3.1 of this thesis, although not discussed in detail, show the possiblity of assembling bands from a mixture of particles with the same radius, but different zeta potentials. One possiblity for future work is the study of novel printed structures using heterogeneous assembly to determine how physcal properties of the resulting structure depend on particle composition.

Alternatively, there is the possibility of separating particles based on their zeta potentials like in field-flow fractionation such as described in Choi *et al*. (2020). Choi *et al*. identified three different proteins in a mixture through the application of an electric field. For this thesis, some preliminary experiments on a mixture of particle solutions from Tbl. 3.1, which was again not discussed, showed that under certain conditions, a band composed of only one type of particle would form out of a heterogeneous mixture of two types of particles. Determining the circumstances under which this occurs over a range of variables would be valuble for future applications that may slectively extract one type of particle from a heterogeneous mixture.

Aside from polystyrene particles, this research might also be applicable to organic materials *i.e*. platelets or viral particles For example, Song *et al*. (2018) describes an

assembly made up of red blood cells at an air-water interface into colloidal crystals using the effect of both convection and gravity. One of the challenges for applying banding to organic materials would be to carefully balance the force/stress on the particles during banding, as to not to damage or destroy them during band formation or simply attraction to the channel wall.

APPENDIX A
MISCELLANEOUS EXERIMENTAL PROCEDURES

This appendix details procedures referenced in the main body of this thesis that are not performed every experiment but are nevertheless occasionally required for the maintenance and evaluation of the experimental setup.

Appendix A.1: Preparation of Stock Sodium Tetraborate Solution

As discussed in Sec. 3.2, one of the components of an experimental solution is a stock 1 mM sodium tetraborate ($Na_2B_4O_7$) solution. This 1 mM stock solution is prepared from a 20 mM $Na_2B_4O_7$ solution and the procedures to make both of these solutions is described below. Also note that the 20 mM $Na_2B_4O_7$ solution is also used to create the 1.1 mM and 0.9 mM $Na_2B_4O_7$ solutions discussed in Appendix A.4 where the procedure is simply a modification of the procedure used to create the 1 mM $Na_2B_4O_7$ solution. The procedure to generate 250 mL of the 20 mM $Na_2B_4O_7$ solution is as follows:

1) Clean a 250.00 ± 0.12 mL volumetric flask (Kimax 28040-250), a 200 mL beaker, a magnetic stirring bar, and opaque 200 mL storage container for the final 20 mM $Na_2B_4O_7$ solution using detergent (Alconox 1104). Allow these items to dry before usage.
2) Weigh 1.907 ± 0.001 g of the solute, sodium tetraborate decahydrate ($Na_2B_4O_7 \cdot 10H_2O$) (Alfa Aesar 40114, Lot R24C036) using weighing paper with an analytical balance (Sartorius AZ124).
3) Pour the solute into the volumetric flask.

4) Wash any remaining solute on the weighing paper into the volumetric flask with deionized (DI) water.
5) Pour DI water into the volumetric flask until it is nearly full; use the pipette to transfer DI water from the beaker to finish filling the volumetric flask.
6) Place the magnetic stirring rod into the volumetric flask and place it on a hotplate (VWR 370 Hot Plate Stirrer). Have the magnetic stirring rod mix the solution at room temperature until the solute has dissolved, typically within 10 minutes.
7) Filter the 20 mM $Na_2B_4O_7$ solution into the storage container through a conical filter funnel and filter paper (Whatman WH1001-917). Hold the magnetic stirring rod inside the volumetric flask using a magnet.
8) Close the container and store the solution under refrigeration at ~4 °C.

Considering the uncertainty in the volumetric flask volume and the mass measured by the analytical balance, the molarity of this $Na_2B_4O_7$ solution is estimated to be 20.00 ± 0.02 mM.

To dilute this 20 mM solution to the desired stock 1 mM $Na_2B_4O_7$ solution:

1) Clean a 250.00 ± 0.12 mL volumetric flask (Kimax 28040-250), a 200 mL beaker, and a storage container for the final 1 mM $Na_2B_4O_7$ solution using detergent (Alconox 1104). Allow these items to dry before usage.
2) Open a packaged or cleaned graduated pipette (FisherSci 13-676-10J) to transfer 12.5 ± 0.2 mL of the 20.00 ± 0.02 mM $Na_2B_4O_7$ solution into the volumetric flask.

3) Pour deionized water into the volumetric flask until it is nearly full; use the pipette to finish filling the flask.
4) Follow with steps #7 and 8 in the previous procedure.

Considering the measurement uncertainties of the volumetric flask volume and the graduated pipette and the uncertainty in the concentration of the 20 mM $Na_2B_4O_7$ solution, the uncertainty in the molarity of this diluted sodium tetraborate solution should be 1.00 ± 0.02 mM.

Appendix A.2: Detailed Nano-Strip Cleaning

While using the fused silica channels, the inner surface of the channel becomes fouled and must be cleaned, typically about every 50 hours of runtime, more thoroughly than the usual cleaning process performed at the beginning and end of each experiment. This is done by flowing Nano-Strip (KMG), a stabilized version of Piranha etch solution consisting of sulfuric acid and hydrogen peroxide, inside of a fume hood. Although effective at removing the polystyrene particles and other debris from the channel, Nano-Strip also removes the epoxy holding the channel reservoirs.

During the experiments, particles become stuck to the channel walls. Simple methods to remove these particles, which include sonication and flushing with various heated organic solvents and alkali solutions, remove most, but not all, of these particles. In addition, particles also aggregate with other particles and debris to form larger blockages.

To clean the channel with Nano-Strip, the following procedure is followed:

1) Clean two 200 mL beakers using detergent (Alconox 1104). Allow these items to dry before usage. Prepare a syringe pump, 10 mL syringe, glass pipette,

several paper towels, and a length of flexible Nano-Strip resistant (*e.g.* Teflon) tubing to connect the syringe to a channel reservoir.

2) Place Nano-Strip container, along with disposal containers for contaminated solids, diluted Nano-Strip and concentrated Nano-Strip within the fume hood. Since Nano-Strip has an exothermic reaction with water, it is important to keep diluted Nano-Strip waste, mostly water used to flush away Nano-Strip, separate from the more concentrated waste used to dissolve epoxy and/or blockages within the channel.
3) Wear appropriate PPE for Nano-Strip; a MSDS can be found at the following website: https://us.vwr.com/assetsvc/asset/en_US/id/13485998/contents. Recommendations for PPE include a lab coat, goggles, and two layers (*e.g.* thick nitrile gloves (Ansell 117075) over standard nitrile lab gloves (Ansell N192) of gloves.
4) Fill a 200 mL beaker with 100 mL water. The water and paper towels are used to quickly clean any spills that may occur within the fume hood.
5) Set aside a space within the fume hood for the syringe pump and two beakers.
6) Connect an empty syringe to the one of the channel reservoirs using the tubing. Roughly 0.2 mL of Nano-Strip should flow through that channel using an applied pressure difference of < 0.5 atm.
7) Pour a small amount (~20 mL) of Nano-Strip into the remaining 200 mL beaker. Use the glass pipette to fill the other channel reservoir (*i.e.*, the one not connected to syringe) with Nano-Strip.

8) Arrange the tubing and channel so that this reservoir is submerged in the Nano-Strip in the beaker. Loosely cover the beaker to reduce splashing.
9) Turn on the syringe pump and leave it to run for ~8 hours. The epoxy connecting the reservoir not connected to the syringe should be dissolved at this point, and that reservoir should be at the bottom of the beaker. Ideally, the other reservoir should also have detached from the channel and be at the bottom of the beaker. If so, continue to step 12.
10) If the remaining reservoir is still connected to the tubing, disconnect the syringe from the syringe pump and carefully dip the channel into the beaker filled with water to clean the outside. Disconnect the reservoir and channel from the tubing and dry the outside. If Nano-Strip comes into contact with PPE, clean immediately with water and paper towels if minor. If major contact of the Nano-Strip with PPE occurs, carefully remove PPE and dispose.
11) Submerge the dried channel and reservoir in the beaker with Nano-Strip and leave until the reservoir detaches from the channel. Sonication of this beaker may be necessary. Fill the other beaker with fresh (*i.e.*, clean) water.
12) Using tweezers, remove the channel and reservoirs from the Nano-Strip filled beaker and place in the water-filled beaker. Dip the tweezers into the water as well to wash off some of the Nano-Strip.
13) Allow the channel to sit immersed in the water for about an hour. Then flush the inside of the channel with water using a syringe attached to flexible tubing. Since the channel at this point lacks reservoirs, some extra preparation must be done to flush the channel with water one last time. Dispense some water on

one of the channel entrances to provide water that can be drawn through the microchannel. Then, attach flexible tubing to a syringe and press the end of the tubing against the (bare) end of the channel to minimize gaps. Draw through the channel with the syringe until the water has flowed through the entire channel.

14) Dispose of all used solution and contaminated materials. Clean all glassware.

Appendix A.3: Detailed Reservoir Attachment

The epoxy (LocTite E-60 HP) used to attach the reservoirs to the channel is quite strong and should be able to easily withstand applied forces during experiments. However, if the epoxy has failed or has been dissolved during cleaning with Nano-Strip (*cf*. previous section), the reservoirs must be re-epoxied to the channel. After removal of the old epoxy, either by dissolving with Nano-Strip in a fume hood as mentioned in Appendix A.2 or by scraping it off with a knife, which is only recommended if there are merely trace remnants of the epoxy remaining, the reservoirs are attached to the channel as follows:

1) Prepare space in an oven capable of staying at 55 °C for 12 hours.
2) Dispense the epoxy (LocTite E-60 HP) on a disposable surface and mix thoroughly using a standard chemistry spatula.
3) Use spatula to place epoxy on the end of one of the two reservoirs over a circle of 4 to 6 mm in diameter. Gently place reservoir, epoxy side down, above channel inlet/outlet. Make sure the epoxy has not covered the inlet/outlet.
4) Press down on the reservoir to evenly spread the epoxy. Once again, make sure the epoxy has not covered the channel inlet/outlet.

5) If the channel inlet/outlet is covered, quickly clean with acetone. Nano-Strip may be required to dissolve the epoxy for severe blockages.
6) Repeat steps 3-4 for the other reservoir.
7) Place channel and reservoirs in oven and bake at 55° C for 12 hours.

Appendix A.4: Wall Zeta Potential Measurement

The channel wall zeta potential may vary due to fouling of the channel walls with particles, other contaminates, or individual differences between the channels. Therefore, it is useful to directly estimate the channel zeta potential. The procedure to do so is based on the current-monitoring method described by Sze *et al.* (2003) and is as follows:

1) Generate 1.1 mM and 0.9 mM $Na_2B_4O_7$ solutions using 20 mM $Na_2B_4O_7$ solution with DI water as discussed in Appendix A.1.
2) Flush the entire channel using 1.1 mM $Na_2B_4O_7$ using ~0.5 mL of solution. Make sure, by visual inspection for example, that the channel is completely filled with solution.
3) Drain the 1.1 mM sodium tetraborate from one reservoir, but not the microchannel. Fill the drained reservoir with 0.9 mM $Na_2B_4O_7$ solution.
4) Place electrodes into both reservoirs and attach electrodes with a power supply and the oscilloscope.
5) Try to adjust the free surfaces in both reservoirs are at the same altitude.
6) Turn on the oscilloscope, wait 10 s and record ambient voltage for at least 1 minute.

7) Apply a voltage difference (1000 V) using the power supply and wait for the oscilloscope reading to reach a steady-state value.
8) Record this steady-state value for 10 s and save this recording as an image.
9) Turn off power supply and oscilloscope. Remove electrodes and flush channel with more 1.1 mM solution.
10) Start from step 3 and repeat steps 4–9 for two more trials. Average results from these three trials.

APPENDIX B
UNCERTAINTY ANALYSIS

This appendix details how the uncertainties in the various experimental parameters discussed in the main body of the thesis are determined as well as more detailed measurement methods. These uncertainties are based on the accuracy of the experimental data and standard uncertainty propagation methods.

For a sample experimental parameter $N_1 = F(A_1, A_2, A_3, \cdots)$ which is a function F of the experimental measurements $A_1, A_2, A_3, \ldots$, the uncertainty in N_1, or U_{N1}, is determined from the uncertainty of the experimental measurements, U_{A1}, U_{A2}, U_{A3}, … respectively, as follows:

$$U_{N_1} = \sqrt{\left(U_{A_1}\frac{\partial F}{\partial A_1}\right)^2 + \left(U_{A_2}\frac{\partial F}{\partial A_2}\right)^2 + \left(U_{A_3}\frac{\partial F}{\partial A_3}\right)^2 + \cdots} \qquad [B.1]$$

Appendix B.1: Region of Interest Dimensions

To determine the physical dimensions of the region of interest imaged by a magnification M = 40 objective (Leica 506059), a stage micrometer, *i.e.*, a slide with a calibrated scale, was viewed using the objective. A 512 by 512 pixels image of a stage micrometer is shown in Fig. B.1. In this image, the distance between six markings, corresponding to a distance of 0.005 inches on the scale, was about 384 pixels. Assuming that the centers of the markings can be determined within 1 pixel, the conversion factor from μm to pixels, or the magnification, is 0.3969 ± 0.0015 μm/pixel. Using this conversion factor, 512 pixels was determined to have a dimension of 203.20 ± 0.75 μm.

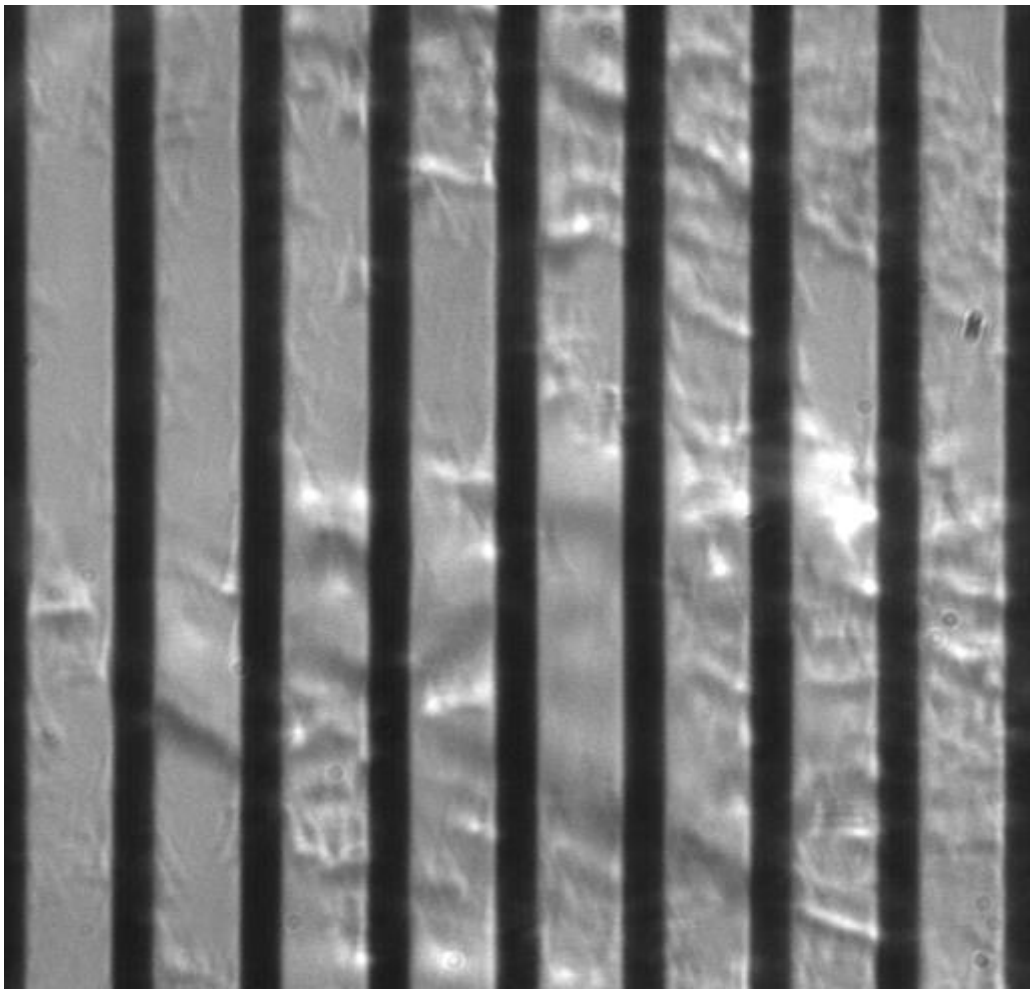

Figure B.1: Image of stage micrometer

Appendix B.2: Channel Length

The overall length, or streamwise dimension, of the microchannel, L, was measured by imaging six separate portions of the channel using the Bertrand lens installed in the microscope with a magnification $M = 1$. These images are then merged into a composite image of the entire channel, as shown in Fig. B.3, by aligning certain features (*e.g.* scratches, irregularities in the channel walls due to the wet-etching process) as fiducial marks between adjacent images. The merger of the individual images into a composite image is shown in Fig. B.2. The path of the microchannel is then modeled as three straight

sections connected by two quarter-circles as sketched in Fig. B.4. Here, the experimental parameters are the lengths of the three straight sections and the radii of the two bends. After determining L in pixels, the conversion factor from μm to pixels, or magnification, for the Bertrand lens, is assumed to be 40 (0.3969 ± 0.0015 μm/pixel) = 15.875 ± 0.058 μm/pixel based on the value determined in the previous section. This is then used to convert L from pixels to mm.

The uncertainty of the length of the microchannel path in pixels is estimated to be four pixels per straight section, four pixels for the radius of each bend, and four pixels for every merger between the five constituent images. Based on Eq. B.1, these individual uncertainties give an overall uncertainty in L of 14 pixels, or 230 μm. For this particular channel, labeled #62, L = 4.22 ± 0.03 cm and the length of the central straight section L_S = 2.78 ± 0.02 cm.

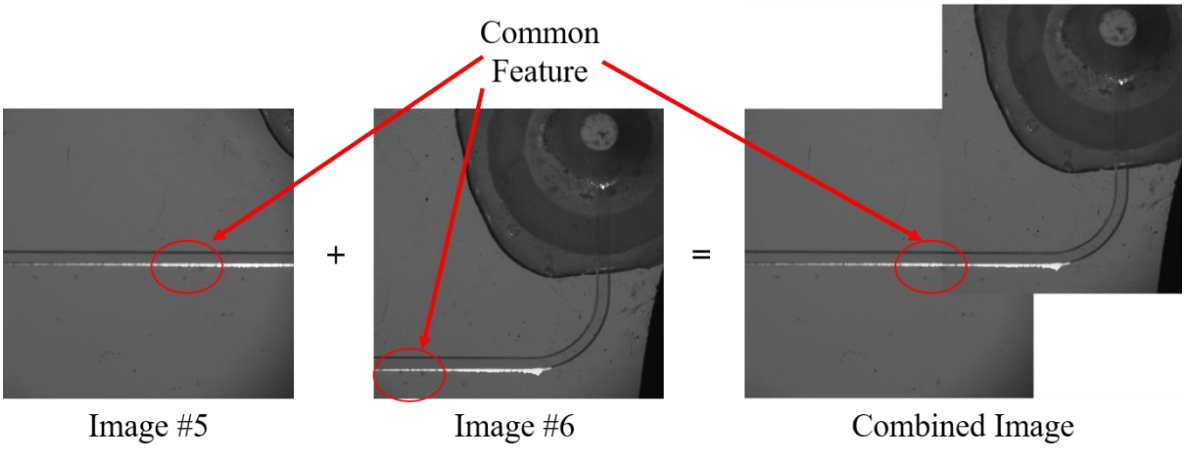

Figure B.2: Combination of individual images into a combined image

Figure B.3: Combined image of channel

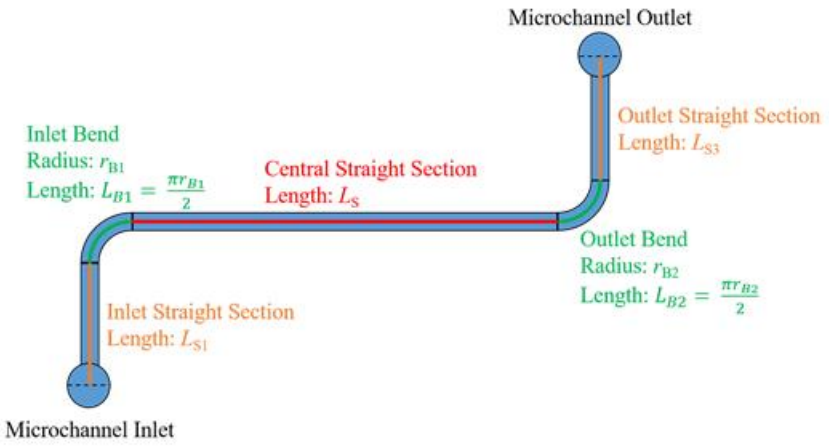

Figure B.4: Sketch of channel path dimensions

Appendix B.3: Penetration Depth

The intensity-based penetration depth of the evanescent wave illumination, z_p, was determined as follows:

$$z_p = \frac{\lambda}{4\pi\sqrt{(n_1 \sin\theta_i)^2 - (n_2)^2}} \qquad [B.2]$$

where λ is the wavelength of the illumination, n_1 = 1.46 is the refractive index of the fused silica lid, θ_i is the angle of incidence, and n_2 = 1.33 is the refractive index of the fluid within the channel, which is assumed to have the properties of water.

To determine the angle of incidence, the beam path as it reflects off the bottom surface of the fused-silica lid, reflects off the channel wall, then reflects again off the bottom surface of the fused silica lid is captured from below using the Bertrand lens. These three reflections are visible as Total Internal Reflection (TIR) spots, as shown in Fig. B.5.

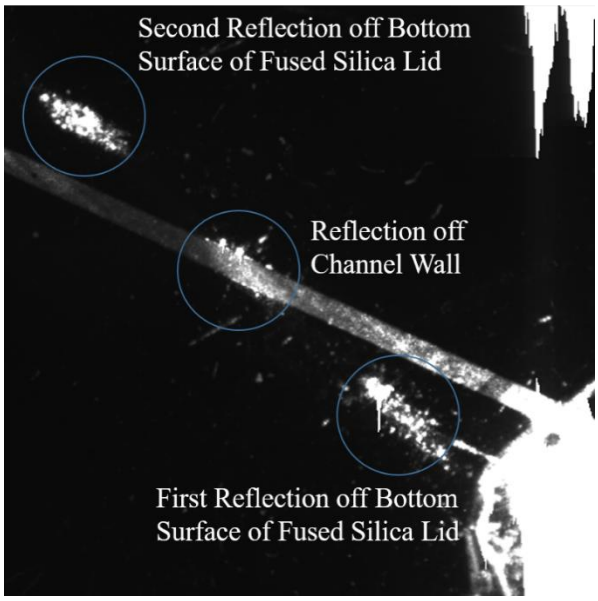

Figure B.5: Bottom view of TIR spots illuminated at λ = 488 nm. This image was taken using the Bertrand lens in the microscope.

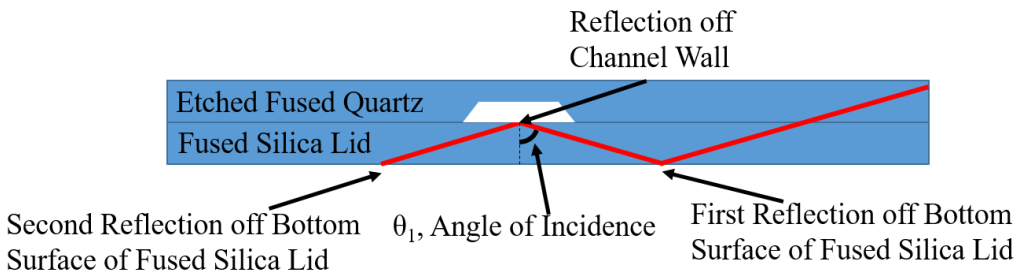

Figure B.6: Side view of reflections. The beam path is shown as red for clarity.

The location of these TIR spots is then used to determine θ_i, as sketched in Fig. B.6. The angle of incidence is therefore

$$\theta_i = \tan^{-1}\left(\frac{D_V}{2D_H}\right) \qquad [B.3]$$

where D_V is the horizontal distance between TIR spots on the bottom of the lid in mm and $D_H = 1 \pm 0.001$ mm is the thickness of the fused silica lid. For a typical experiment, θ_i should be about 1.25 ± 0.01 radians. The uncertainty in θ_i:

$$U_{\theta_i} = \sqrt{\left[\frac{U_{D_V}}{U_{D_H}}\frac{1}{1+\left(\frac{D_V}{4D_H}\right)^2}\right]^2 + \left[-\frac{U_{D_H}D_V}{2(D_H)^2}\frac{1}{1+\left(\frac{D_V}{4D_H}\right)^2}\right]^2} \qquad [B.4]$$

Lastly, the uncertainty in z_p:

$$U_{z_p} = -\frac{\lambda U_{\theta_i}}{4\pi}\left[(n_1)^2(\sin\theta_i)(\cos\theta_i)\right]\left[(n_1\sin\theta_i)^2-(n_2)^2\right]^{-3/2} \qquad [B.5]$$

APPENDIX C
COMPARISON BETWEEN TIMESCALES BASED ON BAND FORMATION OR GRAYSCALE STANDARD DEVIATION

In this appendix, the differences between the timescale based on band formation, T_o, and the timescale based on grayscale standard deviation, T_I, will be discussed to determine if T_I is a viable alternative for T_o. This will be determined by comparing their values over a range of data. If the values are close enough, T_I will be considered an acceptable alternative for T_o. As a reminder, T_o is generated by determining the number of bands N in the illuminated region over time, using the frames in a video, and fitting a sigmoid function to the data. On the other hand, T_I directly takes the overall standard deviation of each frame in a video of time. Details for determining T_o and T_I are Secs. 4.4 and 4.6 respectively.

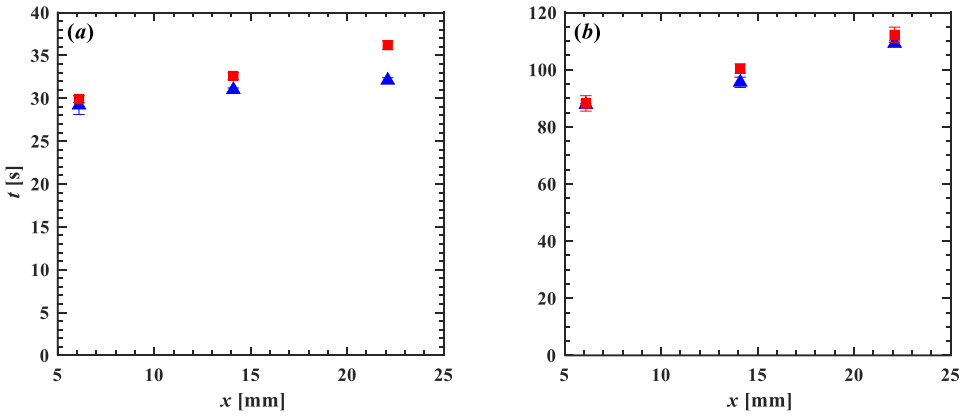

Figure C.1: T_o (▲) vs T_I (■) for *a*) E = 84 V/cm, $\dot{\gamma}_w$ = 1390 s^{-1}, φ_∞ = 0.17% and *b*) E = 94 V/cm, $\dot{\gamma}_w$ = 730 s^{-1}, φ_∞ = 0.08%. Each data point represents the average of 3 trials where the standard deviation is shown as a vertical error bar, many of which are as large as the symbol.

Fig. C.1 shows that there is a small difference between T_o and T_I with the exception of the case where x = 22.1 mm for Fig. C.1*a*. In addition, the value of T_I is always higher

than that of T_o. For all of the data shown, the average difference between T_o and T_I is about 5% of the value of T_o. Therefore, T_I is an acceptable alternative for T_o.

APPENDIX D
ELECTRIC FIELD VS. ELECTRIC FIELD OFFSET

The purpose of this appendix is to better describe the reasoning for why the data provided in Chapter 5 is described in terms of the applied electric field subtracted by the minimum electric field required for bands to form, all other conditions being the same, rather than simply E. This difference, $\Delta E = E - E_{min}$. The major reason for this is that ΔE reduced the difference between several sets of data, as is shown in Fig. D.1 for the case of the inverse of the number of steady-state bands, N_s^{-1} over a range of experimental solution particle volume fractions, φ_∞.

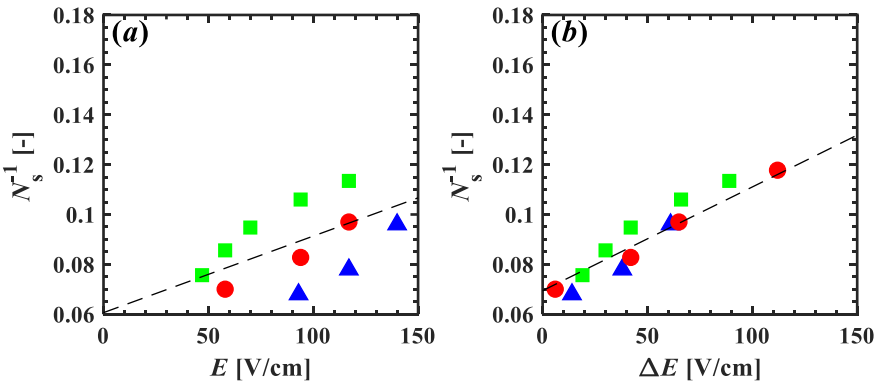

Figure D.1: N_s^{-1} vs. (*a*) E or (*b*) ΔE for $\dot{\gamma}_w = 1390\ s^{-1}$ for $\varphi_\infty = 0.08\%$ (▲), 0.17% (●) and 0.33% V/cm (■). Each data point represents the average of 3–4 trials. The dashed lines are linear fits.

A linear fit to this data was considered since, as mentioned in Sec. 5.4, a linear fit was appropriate to the data of N_s^{-1} vs. offset electric field, ΔE, or alternatively to the normalized offset electric field, $a(\Delta E)/\zeta_p$, while a and ζ_p were held constant. Using a linear fit to the data, $N_s^{-1} = A(E_{var}) + B$, where A and B are variables and E_{var} is either E as in Fig. D.1*a* or ΔE as in Fig. D.1*b*, the difference between the sets of data was considered

using the root mean square error (RMSE) for the fit. For Fig. D.1*a*, the RMSE was 0.0128 and for Fig. D.1*b*, the RMSE was 0.0062 which was significantly smaller. Therefore, ΔE was used for the data provided in Chapter 5 rather than E.

APPENDIX E
HETEROGENEOUS RESULTS

In this appendix, some preliminary results on a heterogeneous solution containing two types of particles of different zeta potentials, ζ_p, but similar size, a, are discussed. The heterogeneous solution was a combination of the two particles in Tbl. E.1, mixed in a ratio of 10% green ThermoFisher F8813 particles and 90% red Polysciences 19507-5 particles for a total particle volume fraction, φ_∞, of 0.33%. Data on the timescale for band formation, T_o, and the steady-state number of bands, N_s, was compared between the solutions described in Tbl. E.2.

Table E.1: List of Vendor Solutions

#	Particles	Background Electrolyte	Maximum Emission /Excitation λ [nm]	a [nm]	ζ_p [mV]
1	ThermoFisher F8813	1 mM Sodium Tetraborate	505/515	245	–42
2	Polysciences 19507-5	1 mM Sodium Tetraborate	525/565	250	–77

Table E.2: List of Experimental Solutions

#	Solution Composition
1	φ_∞ = 0.297% red particles, φ_∞ = 0.033% green particles
2	φ_∞ = 0.33% green particles
3	φ_∞ = 0.33% red particles
4	φ_∞ = 0.033% green particles
5	φ_∞ = 0.297% red particles

E_{min} for experimental solutions #1–5 are described in Fig. E.1. Each data point for experimental solutions #2–5 represents the average of two trials while the data for experimental solution #1 represents three data points.

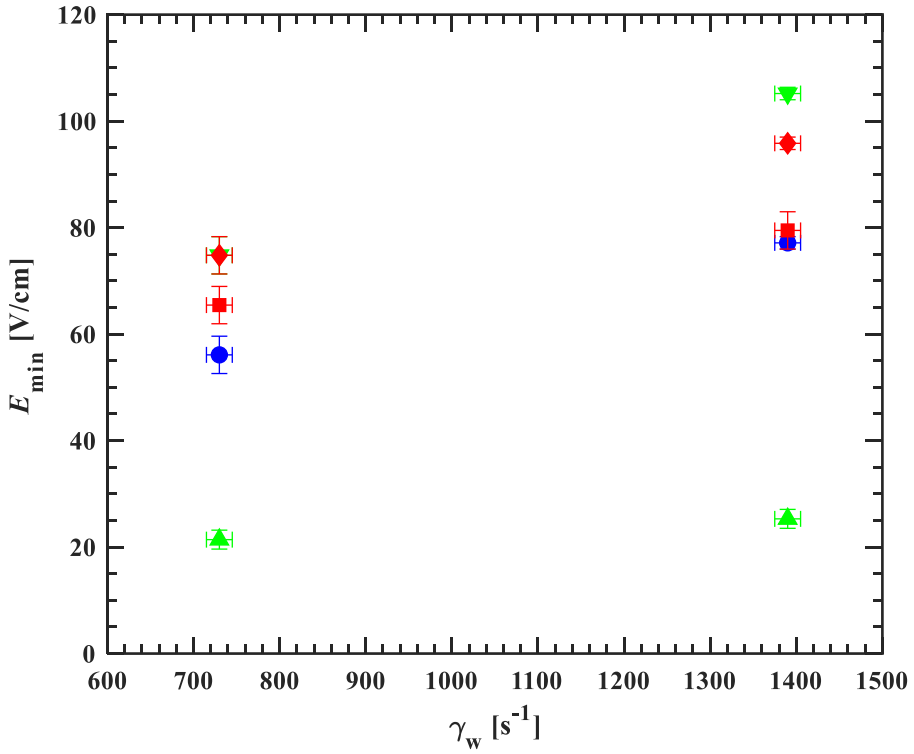

Figure E.1: Heterogeneous results for E_{min} for the solutions mentioned in Tbl. E.2: φ_∞ = 0.297% red particles, φ_∞ = 0.033% green particles (●), φ_∞ = 0.33% green particles (▲), φ_∞ = 0.33% red particles (■), φ_∞ = 0.033% green particles (▼), φ_∞ = 0.297% red particles (♦).

The results show that the value of E_{min} for the heterogeneous solution is closer to the solution that composes a majority (90%) of it, experimental solution 3 or φ_∞ = 0.33% red particles, more than the solution that only comprises a smaller portion (10%) of it, experimental solution 2 or φ_∞ = 0.33% green particles. However, the value for the heterogeneous solution is between the values for both solutions 2 and 3, showing that both influence the properties of the heterogeneous solution. Lastly, the value of E_{min} for the heterogeneous solution is lower than either of its component solutions, experimental

solutions 4 and 5 or φ_∞ = 0.033% green particles and φ_∞ = 0.297% red particles respectively, showing that the addition of particles to either component solution causes bands to form at a lower E_{min} which is expected from the results in Chapter 5.

T_o for experimental solutions #1–5 are described in Fig. E.2. Each data point for experimental solutions #2–5 represent the average of two trials while the data for experimental solution #1 represents three data points. An exception is at the heterogeneous solution at the 730 s^{-1} near-wall shear rate for ΔE = 70 V/cm where only 1 trial could be collected.

The results have some differences from those found for Tbl. E.1. The value of T_o for the heterogeneous solution are lower than those for experimental solutions 4 and 5, showing that an increase in particle volume fraction will still reduce the banding time as expected from the results in Chapter 5. In addition, the value of T_o is closer to the value for the solution that makes up a majority of it, experimental solution 3, rather than that for the solution that makes up much smaller portion of it, experimental solution 2. However, one major difference is that the value of T_o for the heterogeneous solution does not lie between that for experimental solutions 2 and 3.

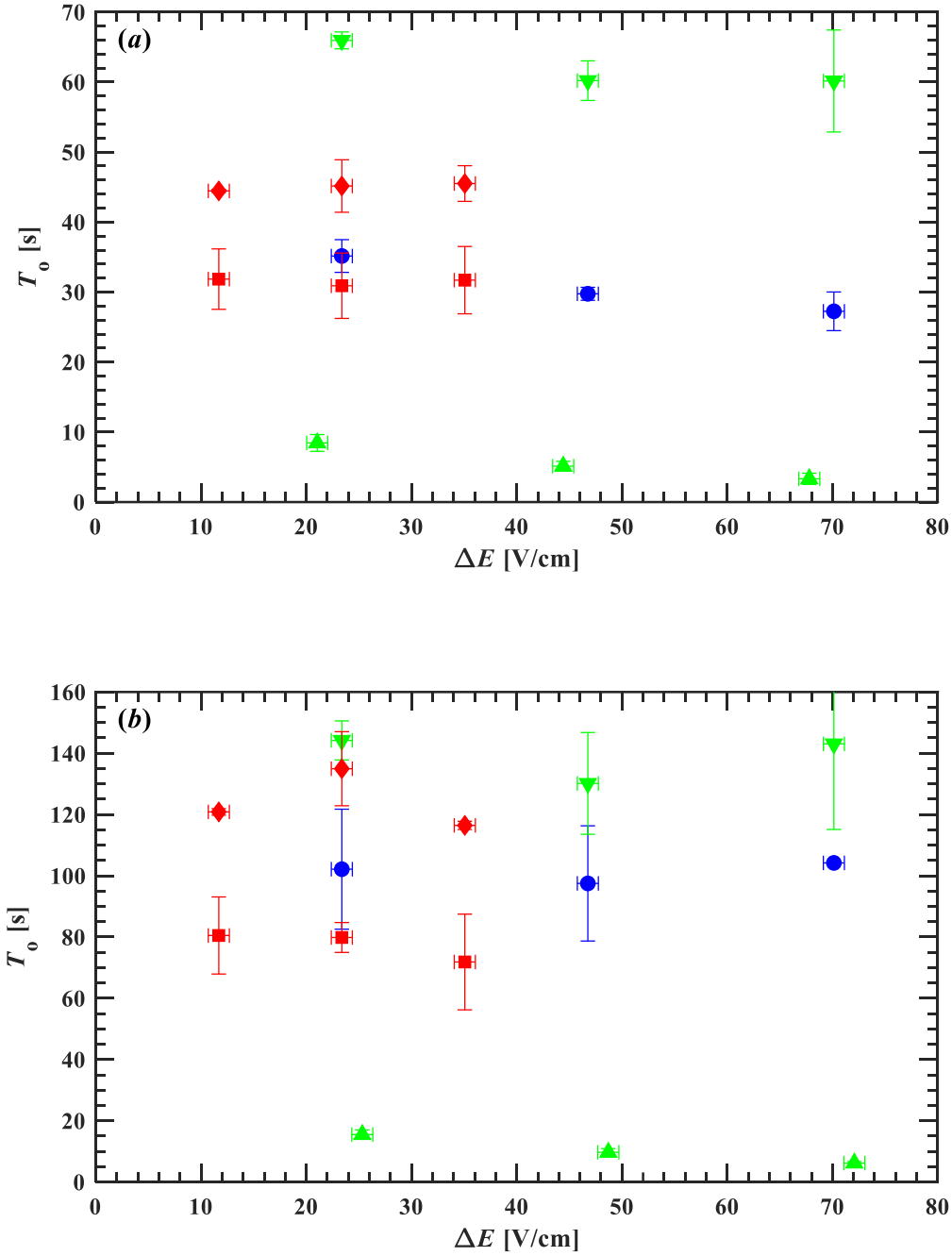

Figure E.2: Heterogeneous results for T_o for the solutions mentioned in Tbl. E.2: φ_∞ = 0.297% red particles, φ_∞ = 0.033% green particles (●), φ_∞ = 0.33% green particles (▲), φ_∞ = 0.33% red particles (■), φ_∞ = 0.033% green particles (▼), φ_∞ = 0.297% red particles (♦) for (*a*) $\dot{\gamma}_w$ = 1390 s^{-1} and (*b*) $\dot{\gamma}_w$ = 730 s^{-1}.

APPENDIX F
PARTICLE COUNTS AT DIFFERENT CHANNEL LOCATIONS

In the steady-state stage, there are variations in particle parameters depending on their streamwise, x, and wall-normal, z, positions. In this appendix, changes in the near-wall particle count, N_p, or number concentration c_p, and near-wall streamwise velocity (U_p) will be reviewed at different channel locations.

Appendix F.1: Particle Counts along Streamwise Direction during Steady-State

The suspended particles should in theory enter the channel with a uniform distribution, but must then assemble into concentrated bands at some streamwise position. This has been shown in Sec. 5.2 where a minimum x for bands to form, x_o, was observed. In Fig. F.1, c_p which is determined by dividing N_p by the area of the region of interest, was observed at steady-state at different x-positions in the channel where c_p increases with x until x = 14.1 mm, then remains consistent farther downstream. Since bands consistently form downstream after x_o and c_p becomes consistent after some position x, Fig. F.1 suggests that the steady-state c_p may be an indication for when the bands are fully formed. Fig. F.1 also suggests that the bands are also stable as they flow in the streamwise the channel.

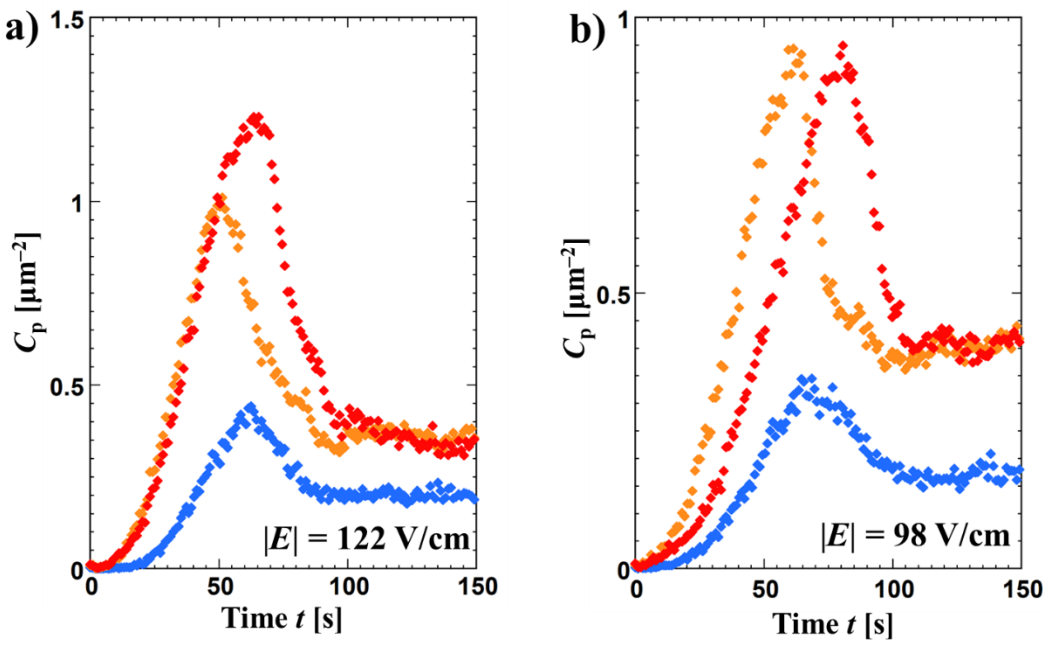

Figure F.1: Near-wall particle number concentration over different positions under the parameters: $\dot{\gamma}_w$ = 730 s^{-1}, a) E = 122 V/cm or b) E = 122 V/cm, φ_∞ = 0.33%, with 1% tracer particles at x = 6.1 mm (♦), 14.1 mm (♦), and 22.1 mm (♦). These values represent the average over four trials.

Particle velocities at different locations were also examined. Fig. F.2 suggests that streamwise velocities reach a steady-state value aside from the extreme downstream case where x = 22 cm. Since the overall flow in the illuminated region is in the upstream direction, this result may imply that particle velocities have not stabilized at x = 22 mm.

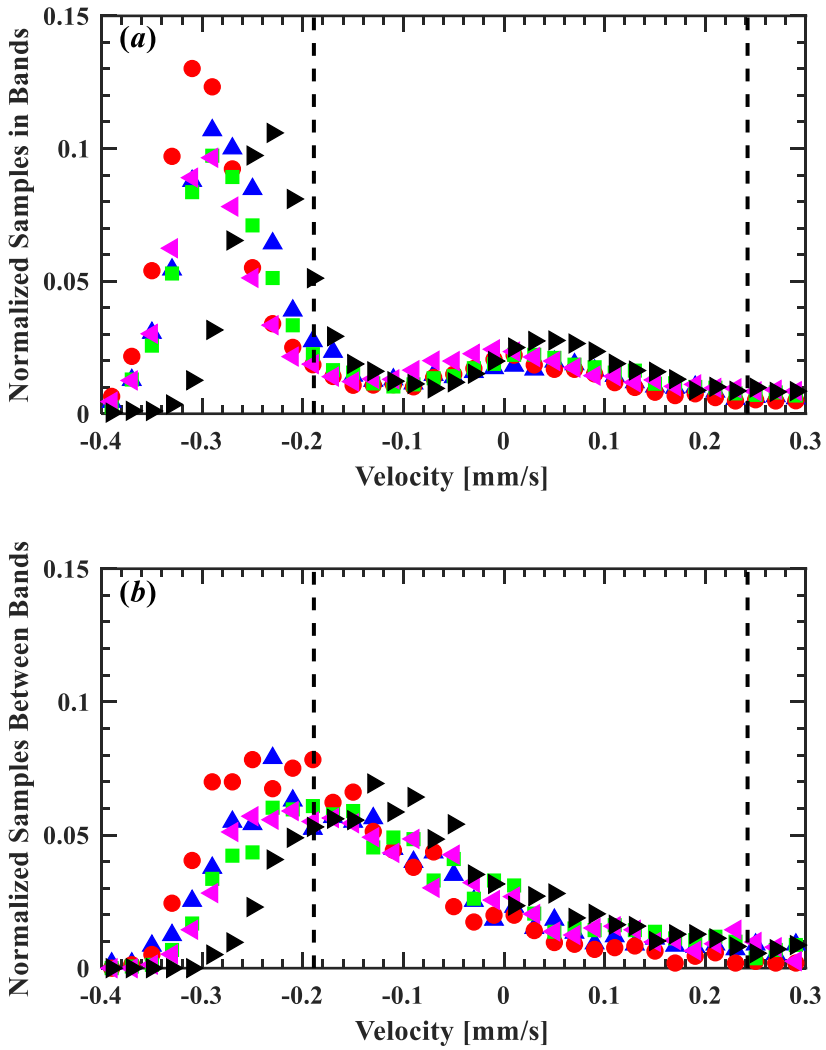

Figure F.2: Near-wall particle velocities along the streamwise direction during the steady-state phase at $\dot{\gamma}_w$ = 1070 s^{-1} and E = 98 V/cm for x = 6 mm (▲), x = 10 mm (●), x = 14 mm (■), x = 18 mm (◀) and x = 22 mm (▶) for particle velocities (*a*) within the bands or (*b*) between the bands. The dashed lines represent the range of expected particle velocity. For this data, the tracer particle concentration was 0.2%.

Section F.2: Estimation of Band Cross-Section during Steady-State Stage

While determining band properties as a function of streamwise (x) position can show how bands develop within the channel, band properties using different z_p can be used instead to estimate band cross-sections and determine if the whole band can be observed

or not in the experiments. Fig. F.3 demonstates how near wall particle area concentrations C_p, or N_p divided by the area of the region of interest, changes with z_p. Although the exact depth of the illuminated region cannot be exactly determined using z_p, it is a reasonable assumption to estimate that the depth of the illuminated region increases as z_p increases.

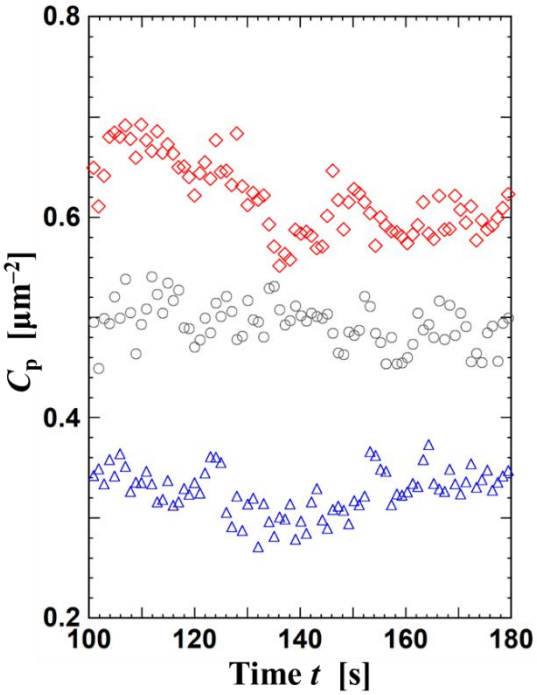

Figure F.3: Near-wall particle concentration over different positions at steady-state under the parameters: $\dot{\gamma}_w$ = 730 s^{-1}, E = 120 V/cm, φ_∞ = 0.33%, with 1% tracer particles at z_p = 100 nm (△), 120 nm (○), and 140 nm (◇). These values represent the mean of 4 trials.

Since the maximum particle concentration increases with z_p and does not seem to reach a maximum value at the furthest limit of z_p, which was a value that taxed the limits of the experimental apparatus, this result implies the experimental setup, which usually uses z_p = 110 nm, only illuminates the "edge" of the band. Furthermore, by assuming that z_p is proportional to the wall-normal extent of illumination, an estimate of how the near-wall particle volume concentration changes with z_p can be derived which is shown in Fig. F.4.

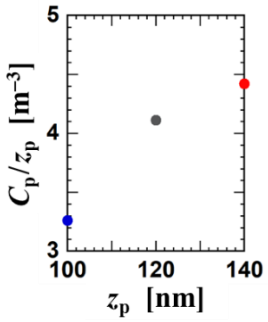

Figure F.4: Averaged particle area concentrations divided by penetration depth to estimate particle volume concentrations under the parameters: $\dot{\gamma}_w$ = 730 s^{-1}, E = 122 V/cm, φ_∞ = 0.33, x = 14.1 mm, a ratio of tracer to bulk particles of 1%, at z_p = 100 nm, 120 nm, and 140 nm.

Fig. F.4 implies that the cross-sectional width of the bands increases with z, which agrees with the observations by Rossi *et al.* (2019) and Lochab *et al.* (2020), where bands were observed to be >5 μm in cross-stream dimension and depth.

APPENDIX G
ESTIMATE OF THE EFFECT OF JOULE HEATING

One potential complication in these experiments is that the temperature of the particle solution inside the channel may vary significantly due to Joule heating. Since certain properties of the solution, which are assumed to be those of water, change significantly with temperature such as the kinematic viscosity ν, temperature variations may affect the magnitude of the expected particle velocity. Measuring the temperature of the near-wall region of the channel is, however, impractical with the experimental setup. Therefore, this section uses experimental observations to determine if Joule heating is a significant concern.

Experimental observations suggest that Joule heating is negligible. During measurements of the channel zeta potential, the temperature of the solution appears to be constant since the change in the voltage across the channel is linear as shown in Fig. G.1. This implies that the fluid velocity, which is inversely proportional to the viscosity, is constant; if the fluid temperature were to vary significantly, the fluid velocity would vary in a non-linear fashion during the measurement.

Additionally, the temperature of the solution in the channel inlet and exit reservoirs was measured using a thermocouple for an applied voltage of 1000 V over 20 minutes, *i.e.*, at a much higher E and over a much longer time than the actual experiments. This temperature, with a measurement accuracy of 0.1 °C did not increase over this 20 minute interval, suggesting that overall Joule heating over the channel is negligible.

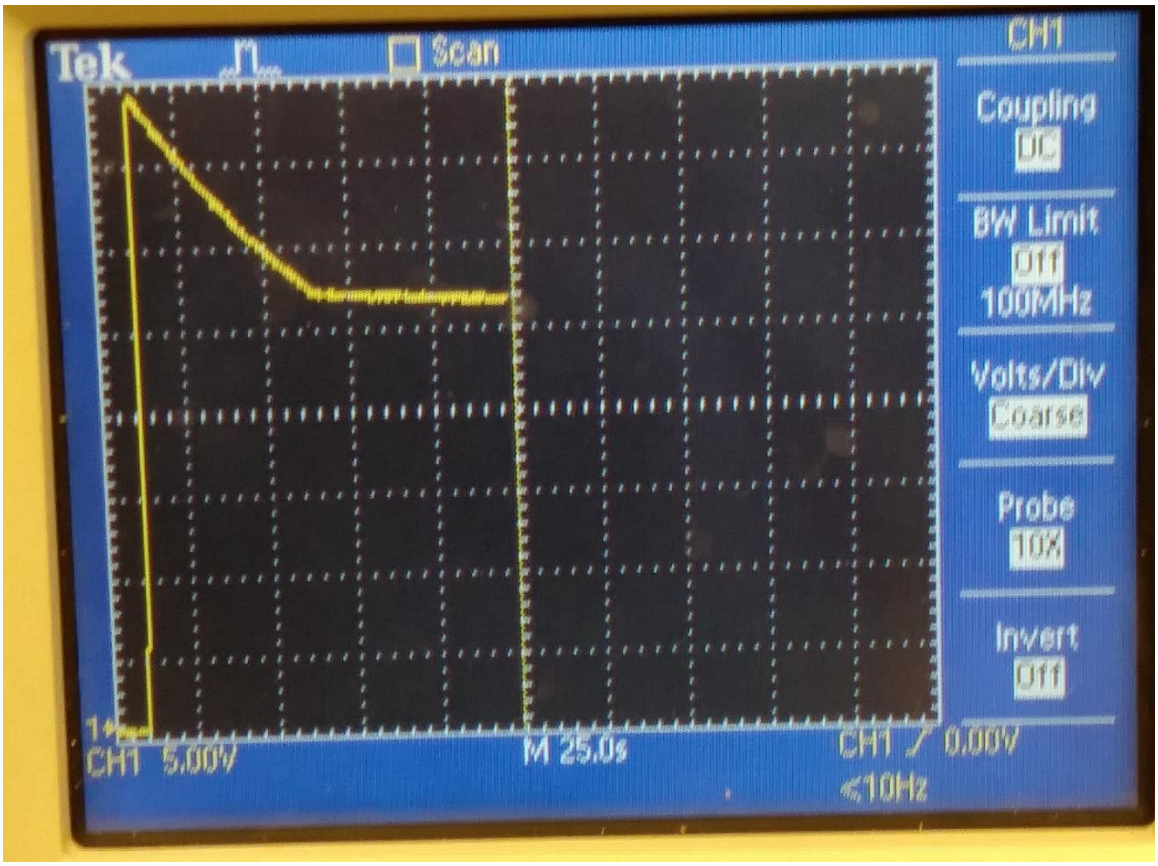

Figure G.1: Linear relationship during wall zeta potential measurement

REFERENCES

S. Acharya, I. Patla, J. Kost, S. Efrima, Y. Golan, "Switchable assembly of ultra narrow CdS nanowires and nanorods," *J. Am. Chem. Soc.*, vol. 128, no. 29, pp. 9294-9295, 2006. doi: 10.1021/ja062404i

J. J. Adler, Y. I. Rabinovich, B. M. Moudgil, "Origins of the non-DLVO force between glass surfaces in aqueous solution," *J. Colloid Interface Sci.*, vol. 237, no. 2, pp. 249-258, 2001. doi: 10.1006/jcis.2001.7466

H. B. Awbi, "Calculation of convective heat transfer coefficients of room surfaces for natural convection," *Energy Build.*, vol. 28, no. 2, pp. 219-227, 1998. doi: 10.1016/S0378-7788(98)00022-X

B. M. Alexander, D. C. Prieve, "A hydrodynamic technique for measurement of colloidal forces," *Langmuir*, vol.3, no. 5, pp. 788-795, 1987. doi: 10.1021/la00077a038

E. S. Asmolov, "The inertial lift on a spherical particle in a plane Poiseuille flow at large channel Reynolds number," *J. Fluid Mech.*, vol. 381, pp. 63-87, 1999. doi: 10.1017/S0022112098003474

E. S. Asmolov, A. L. Dubov, T. V. Nizkaya, J. Harting, O. I. Vinogradova, "Inertial focusing of finite-size particles in microchannels," *J. Fluid Mech.*, vol. 840, pp. 613-630, 2018. doi: 10.1017/jfm.2018.95

S. H. Behrens, D. G. Grier, "The charge of glass and silica surfaces," *J. Chem. Phys.*, vol. 115, no. 14, pp. 6716-6721, 2001. doi: 10.1063/1.1404988

S. G. Bike, D. C. Prieve, "Electrohydrodynamic lubrication with thin double layers," *J. Colloid Interface Sci.*, vol. 136, no. 1, pp. 95-112, 1990. doi: 10.1016/0021-9797(90)90081-X

S. G. Bike, D. C. Prieve, "Electrohydrodynamics of thin double layers: a model for the streaming potential profile," *J. Colloid Interface Sci.*, vol. 154, no. 1, pp. 87-96, 1992. doi: 10.1016/0021-9797(92)90080-6

V. Bjerknes, J. Bjerknes, H. Solberg, T. Bergenson, *Physikalische Hydrodynamik*, Berlin, 1933. doi: 10.1007/978-3-642-52616-9

F. Carrique, F. J. Arroyo, "Effect of stagnant-layer conductivity on the electric permittivity of concentrated colloidal suspensions," *J. Chem. Phys.*, vol. 126, 104903 (9p), 2007. doi: 10.1063/1.2538679c

N. Cevheri, M. Yoda, "Electrokinetically driven reversible banding of colloidal particles near the wall," *Lab Chip*, vol. 14, no. 8, pp. 1391-1394, 2014a. doi: 10.1039/C3LC51341F

N. Cevheri, M. Yoda, "Using shear and direct current electric fields to manipulate and self-assemble dielectric particles on microchannel walls," *J. Nanosci. Nanotechnol.*, vol. 5, issue 3, 031009 (8p), 2014b. doi: 10.1115/1.4029628

N. Cevheri, M. Yoda, "Lift forces on colloidal particles in combined electroosmotic and Poiseuille flow," *Langmuir*, vol. 30, no. 46, pp. 13771-13780, 2014c. doi: 10.1021/la502290y

M. K. Cheezum, W. F. Walker, W. H. Guilford, "Quantitative comparison of algorithms for tracking single fluorescent particles," *Biophys. J.*, vol. 81, no. 4, pp. 2378-2388, 2001. doi: 10.1016/S0006-3495(01)75884-5

S. Chen, E. Olson, S. Jiang, X. Yong, "Nanoparticle assembly modulated by polymer chain conformation in composite materials," *Nanoscale*, vol. 12, pp. 14560-14572, 2020. doi: 10.1039/D0NR01740J

J. Choi, C. Fuentes, J. Fransson, M. Wahlgren, L. Nilsson, "Separation and zeta-potential determination of proteins and their oligomers using electrical asymmetrical flow field-flow fractionation (EAF4)," *J. Chromatogr. A*, vol. 1633, pp. 461625 (8 p), 2020. doi: 10.1016/j.chroma.2020.461625

A. Choudhary, T. Renganathan, S. Pushpavanam, "Inertial migration of an electrophoretic rigid sphere in a two-dimensional Poiseuille flow," *J. Fluid Mech.*, vol. 874, pp. 856-890, 2019. doi: 10.1017/jfm.2019.479

A. Choudhary, T. Renganathan, S. Pushpavanam, "Comment on 'Migration of an electrophoretic particle in a weakly inertial of viscoelastic flow'," *Phys. Rev. Fluid*, vol. 6, no. 3, 036701 (4p), 2021. doi: 10.1103/PhysRevFluids.6.036701

P. Cherukat, J. B. McLaughlin, "The inertial lift on a rigid sphere in a linear shear flow field near a flat wall," *J. Fluid Mech.*, vol. 263, pp. 1-18, 1994. doi: 10.1017/S0022112094004015

R. G. Cox, H. Brenner, "The lateral migration of solid particles in Poiseuille flow—I Theory," *Chem. Eng. Sci.*, vol. 23, no. 2, pp. 147-173, 1968. doi: 10.1016/0009-2509(68)87059-9

A. V. Delgado, F. González-Caballero, R. J. Hunter, L. K. Koopal, J. Lyklema, "Measurement and interpretation of electrokinetic phenomena," *J Colloid Interface Sci.*, vol. 309, pp. 194-224, 2007. doi: 10.1016/j.jcis.2006.12.075

D. Dendukuri, P. S. Doyle, “The synthesis and assembly of polymeric microparticles using microfluidics,” *Adv. Mater.*, vol. 21, no. 41, pp. 4071-4086, 2009. doi: 10.1002/adma.200803386

B. Derjaguin, L. Landau, “Theory of the stability of strongly charged lyophobic sols and of the adhesion of strongly charged particles in solutions of electrolytes,” *Prog. Surf. Sci.*, vol. 43, pp. 30-59, original 1941 reprinted 1993. doi: 10.1016/0079-6816(93)90013-L

D. Di Carlo, “Inertial microfluidics,” *Lab Chip*, vol. 9, no. 21, pp. 3038-3046, 2009. doi: 10.1039/B912547G

P. Dutta, A. Beskok. “Analytical solution of combined electroosmotic/pressure driven flows in two-dimensional straight channels: finite Debye layer effects.,” *Anal. Chem.*, vol. 73, no. 9, pp. 1979-1986, 2001. doi: 10.1021/ac001182i

A. P. Gast, C. F. Zukoski, “Electrorheological fluids as colloidal suspensions,” *Adv. Colloid Interface Sci.*, vol. 30, pp. 153-202, 1989. doi: 10.1016/0001-8686(89)80006-5

A. J. Goldman, R. G. Cox, H. Brenner, “Slow viscous motion of a sphere parallel to a plane wall—I Motion through a quiescent fluid,” *Chem. Eng. Sci.*, vol. 22, no. 4, pp. 637-651, 1967a. doi: 10.1016/0009-2509(67)80047-2

A. J. Goldman, R. G. Cox, H. Brenner, “Slow viscous motion of a sphere parallel to a plane wall—II Couette Flow,” *Chem. Eng. Sci.*, vol. 22, no. 4, pp. 653-660, 1967b. doi: 10.1016/0009-2509(67)80048-4

H. J. Keh, S. B. Chen, “Electrophoresis of a colloidal sphere particle to a dielectric plane,” *J. Fluid Mech.*, vol 194, pp.377-390, 1988. doi: 10.1017/S0022112088003039

M. Grzelczak, J. Vermant, E. M. Furst, L. M. Liz-Marzán, “Directed self-assembly of nanoparticles,” *ACS Nano*, vol. 4, no. 7, pp. 3591-3605, 2010. doi: 10.1021/nn100869j

H. C. Hamaker, “The London–van der Waals attraction between spherical particles.” *Physica*, vol. 4, no. 10, pp. 1058-1072, 1937. doi: 10.1016/S0031-8914(37)80203-7

M. Han, C. Kim, S. Lee, “Particle migration in tube flow of suspensions,” *J. Rheol.*, vol. 43, no. 5, pp. 1157-1174, 1999. doi: 10.1122/1.551019

Heraeus Quarzglas GmbH & Co. KG, *Standard Optics Information*, accessed August 2021. https://cdn.shopify.com/s/files/1/1090/0622/files/Heraeus-HOQ-310-Fused-Quartz.pdf?5509191820080193540.

B. P. Ho, L. G. Leal, “Inertial migration of rigid spheres in two-dimensional unidirectional flows,” *J. Fluid Mech.*, vol. 65, no. 2, pp. 365-400, 1974. doi: 10.1017/S0022112074001431

J. N. Israelachvili, *Intermolecular and Surface Forces (Third Edition)*. Academic Press, 2011. doi: 10.1016/C2009-0-21560-1

B. R. Jennings, M. Stankiewicz, “Electro-optic observations of electrodynamic bands formation in colloidal suspensions,” *Proc. R. Soc. Lond. A*, vol. 427, pp. 321-330, 1990. doi: 10.1098/rspa.1990.0015

M. L. Jiménez, F. J. Arroyo, F. Carrique, U. Kaatze, A. V. Delgado, “Determination of stagnant layer conductivity in polystyrene suspensions: temperature effects,” *J. Colloid Interface Sci.*, vol. 281, no. 2, pp. 503-509, 2005. doi: 10.1016/j.jcis.2004.08.093

Y. Kazoe, M. Yoda, “Experimental study of the effect of external electric fields on interfacial dynamics of colloidal particles,” *Langmuir* vol. 27, no. 18, pp. 11481-11488, 2011. doi: 10.1021/la202056b

A. S. Khair, B. Balu, “The lift force on a charged sphere that translates and rotate in an electrolyte,” *Electrophoresis*, vol. 40, no. 18-19, pp. 2407-2414, 2019. doi: 10.1002/elps.201900029

A. S. Khair, J. K. Kabarowski, “Migration of an electrophoretic particle in a weakly inertial of viscoelastic flow,” *Phys. Rev. Fluid*, vol. 5, 033702 (14p), 2020. doi: 10.1103/PhysRevFluids.5.033702

B. J. Kirby, E. F. Hasselbrink Jr., “Zeta potential of microfluidic substrates: 1. Theory, experimental techniques, and effects on separations,” *Electrophoresis*, vol. 25, pp. 187-202, 2004a. doi: 10.1002/elps.200305754

B. J. Kirby, E. F. Hasselbrink Jr., “Zeta potential of microfluidic substrates: 2. Data for polymers,” *Electrophoresis*, vol. 25, pp. 203-213, 2004b. doi: 10.1002/elps.200305755

W. Krasny-Ergen, “Untersuchungen über die Viskosität von Suspensionen und Lösungen. 2. Zur Theorie der Elektroviskosität,” *Kolloid*-Zeitschrift, vol. 74, pp. 172-178, 1936. doi: 10.1007/BF01429631

R. Kretschmer, W. Fritzsche, “Manipulation of metal nanoparticles in micrometer electrode gaps by dielectrophloresis,” *AIP Conf. Proc.*, vol. 725, pp. 85-88, 2004. doi: 10.1063/1.1805382

G. Le, J. Zhang, “A general Poisson-Boltzmann model with position dependent dielectric permettivity for electric double layer analysis,” *Langmuir*, vol. 27, no. 9, pp. 5366-5370, 2011. doi: 10.1021/la200596c

D. Leighton, A. Acrivos, “The lift on a small sphere touching a plane in the presence of a simple shear flow,” *Z. Angew. Math. Phys.*, vol. 36, pp. 174-178, 1985. doi: 10.1007/BF00949042

F. L. Leite, C. C. Bueno, A. L. Da Róz, E. C. Ziemath, O. N. Oliveira Jr., “Theoretical models for surface forces and adhesion and their measurement using atomic force microscopy,” *Int. J. Mol. Sci.*, vol. 13, no. 10, pp. 12773-12856, 2012. doi: 10.3390/ijms131012773

H. F. Li, M. Yoda, “Multilayer nano-particle image velocimetry (MnPIV) in microscale Poiseuille flows,” *Meas. Sci. Technol.*, vol. 19, no. 7, 075402 (9p), 2008. doi: 10.1088/0957-0233/19/7/075402

Q. Liu, K. L. Reifsnider, “Heterogeneous mixtures of elliptical particles: Directly resolving local and global properties and responses,” *J. Comput. Phys.*, vol. 235, pp. 161-181, 2013. doi: 10.1016/j.jcp.2012.09.039

L. Liang, Y. Ai, J. Zhu, S. Qian, X. Xuan, “Wall-induced lateral migration in particle electrophoresis through a rectangular microchannel,” *J. Colloid Interface Sci.*, vol. 347, no. 1, pp. 142-146, 2010a. doi: 10.1016/j.jcis.2010.03.039

L. Liang, S. Qian, X. Xuan, “Three-dimensional electrokinetic particle focusing in a rectangular microchannel,” *J. Colloid Interface Sci.*, vol. 350, no. 1, pp. 377-379, 2010b. doi: 10.1016/j.jcis.2010.06.067

Q. Liang, C. Zhao, C. Yang, “Enhancement of electrophoretic mobility of microparticles near a solid wall—Experimental verification,” *Electrophoresis*, vol. 36, no. 5, pp. 731-736, 2015. doi: 10.1002/elps.201400405

V. Lochab, A. Yee, M. Yoda, A. T. Conlisk, S. Prakash, “Dynamics of colloidal particles in microchannels under combined pressure and electric potential gradients,” *Microfluid Nanofluidics*, vol. 23, no. 134, 2019. doi: 10.1007/s10404-019-2304-0

X. Lu, J. P. Hsu, X. Xuan. (2014). “Exploiting the wall-induced non-inertial lift in electrokinetic flow for a continuous particle separation by size.” *Langmuir*, vol. 31, no. 1, pp. 620-627, 2014. doi: 10.1021/la5045464

J. Lyklema, *Fundamentals of Interface and Colloid Science* , Academic Press, 2000. doi: 10.1016/S1874-5679(05)80005-4

J. M. Martel, M. Toner, “Inertial focusing in microfluidics,” *Annu. Rev. Biomed. Eng.*, vol. 16, pp. 371-396, 2014. doi: 10.1146/annurev-bioeng-121813-120704

J. P. Matas, J. F. Morris, É. Guazzelli, "Inertial migration of rigid spherical particles in Poiseuille flow," *J. Fluid Mech.*, vol. 515, pp. 171-195, 2004. doi: 10.1017/S0022112004000254

J. P. Matas, J. F. Morris, E. Guazzelli, "Lateral forces on a sphere," *Oil Gas Sci. Technol.*, vol. 59, no. 1, pp. 59-70, 2004. doi: 10.2516/ogst:2004006

MATLAB, *Lowess Smoothing*, accessed 8/27/2021. https://www.mathworks.com/help/curvefit/lowess-smoothing.html

J. B. McLaughlin, "Inertial migration of a small sphere in linear shear flows," *J. Fluid Mech.*, vol. 224, pp. 261-274, 1991. doi: 10.1017/S0022112091001751

J. B. McLaughlin, "The lift on a small sphere in wall-bounded linear shear flows," *J. Fluid Mech.*, vol. 246, pp. 249-265, 1993. doi: 10.1017/S0022112093000114

R. Monazami, M. T. Manzari, "Analysis of combined pressure-driven electroosmotic flow through square microchannels," vol. 3, pp. 123-126, 2007. doi: 0.1007/s10404-005-0065-4

J. K. Park, K. J. Lee, "Diffusion coefficients for aqueous boric acid," *J. Chem. Eng. Data*, vol. 39, pp. 891-894, 1994. doi: 10.1021/je00016a057

S. Prakash, V. Lochab, "Electrohydrodynamic printing of pre-assembled colloidal particle structures," 71st Annual Meeting of the American Physical Society Division of Fluid Dynamics, Atlanta, Georgia, Nov. 19, 2018.

D. C. Prieve, P. J. Sides, C. L. Wirth, "2-D assembly of colloidal particles on a planar electrode," *Curr. Opin. Colloid Interface Sci.*, vol. 15, no. 3, pp. 160-174, 2010. doi: 10.1016/j.cocis.2010.01.005

QuickField, *Natural convection coefficient calculator*, accessed August 2021. https://quickfield.com/natural_convection.htm.

A. Ramos, H. Morgan, N. G. Green, A. Castellanos, "Ac elecrokinetics: a review of forces in microelectrode structures," *J. Phys. D*, vol. 31, no. 18, pp. 2338-2353, 1998. doi: 10.1088/0022-3727/31/18/021

H. Ranchon, V. Picot, A. Bancaud, "Metrology of confined flows using wide field nanoparticle velocimetry," *Sci. Rep.*, vol. 5, pp. 10128 (11p), 2015. doi: 10.1038/srep10128

M. Rossi, M. Alvaro, N. Cevheri, C. J. Kähler, M. Yoda, "Particle distribution and velocity in electrokinetically induced banding," *Microfluid Nanofluidics*, vol. 23, no. 67, 2019. doi: 10.1007/s10404-019-2227-9

S. I. Rubinow, J. B. Keller, “The transverse force on a spinning sphere moving in a viscous fluid,” *J. Fluid Mech.*, vol. 11, no. 3, pp. 447-459, 1961. doi: 10.1017/S0022112061000640

P. G. Saffman, “The lift on a small sphere in a slow shear flow,” *J. Fluid Mech.*, vol. 22, no. 2, pp. 385-400, 1965. doi: 10.1017/S0022112065000824

P. G. Saffman, “The lift on a small sphere in a slow shear flow - Corrigendum,” *J. Fluid Mech.*, vol. 31, no. 3, pp. 628, 1965. doi: 10.1017/S0022112068999990

K. Saiki, Y. Sato, “Nanoscale structure of electrokinetically driven flow obtained from large-area evanescent wave excitation,” *Microtas 2004*, vol. 1, pp. 255-257, 2004.

O. Schnitzer, E. Yariv, “Streaming-potential phenomena in the thin-Debye-layer limit. Part 3. Shear-induced electroviscous repulsion,” *J. Fluid Mech.*, vol. 786, pp. 84-109, 2016. doi: 10.1017/jfm.2015.647

O. Schnitzer, I. Frankel, E. Yariv, “Streaming-potential phenomena in the thin-Debye-layer limit. Part 2. Moderate Péclet numbers,” *J. Fluid Mech.*, vol. 704, pp. 109-136, 2012. doi: 10.1017/jfm.2012.221

R. Scirocco, J. Vermant, J. Mewis, “Effect of the viscoelasticity of the suspending fluid on structure formation in suspensions,” *J. Non-Newtonian Fluid Mech.*, vol. 117, pp. 183-192, 2004. doi: 10.1016/j.jnnfm.2004.01.010

G. Segré, A. Silberberg, “Behaviour of macroscopic rigid spheres in Poiseuille flow, Part 1," *J. Fluid Mech.***,** vol. 14, no. 1, pp. 115-135, 1962. doi: 10.1017/S002211206200110X

M. Serhatlioglu, Z. Isiksacan, M. Özkan, D. Tuncel, C. Elbuken, “Electro-Viscoelastic Migration under Simultaneously Applied Microfluidic Pressure-Driven Flow and Electric Field,” *Anal. Chem.*, vol. 92, no. 10, pp. 6932-6940, 2020. doi: 10.1021/acs.analchem.9b05620

F. Smallenburg, H. R. Vutukuri, A. Imhof, A. van Blaaderen, M. Dijkstra, “Self-assembly of colloidal particles into strings in a homogeneous external electric or magnetic field,” *J. Phys. Condens. Matter*, vol. 24, 464113 (10p), 2012. doi: 10.1088/0953-8984/24/46/464113

D. R. E. Snoswell, P. Creaton, C. E. Finlayson, B. Vincent, “Electrically induced colloidal clusters for generating shear mixing and visualizing flow in microchannels,” *Langmuir*, vol. 27, no. 21, pp. 12815-12821, 2011. doi: 10.1021/la202279a

L. Song, D. Xiaolin, L. Zhong, X. Zhang, Z. Cheng, "Self-assembly of anisotropic red blood cell (RBC)-like colloidal particles," *Soft Matter*, vol. 14, no. 39, pp. 7954-7957, 2018. doi: 10.1039/C8SM01652F

J. Stauff, "Perlschnurbildung von Emulsionen im elecktrischen Wechselfeld als Relaxationseffekt, English translation: Pearl string formation of emulsions in alternating electric field as relaxation effect," *Colloid Polym. Sci*., vol. 143, pp. 162-171, 1955. doi: 10.1007/BF01519887

A. Sze, D. Erickson, L. Ren, D. Li, "Zeta-potential measurement using the Smoluchowski equation and the slope of the current-time relationship in electro-osmotic flow," *J. Colloid Interface Sci*., vol. 261, no. 2, pp. 402-410, 2003. doi: 10.1016/S0021-9797(03)00142-5

F. Takemura, J. Magnaudet, "Lateral migration of a small spherical buoyant particle in a wall-bounded linear shear flow," *Phys. Fluids*, vol. 21, no.8, 083303 (7p), 2009. doi: 10.1063/1.3206729

C. Thomas, X. Lu, A. Todd, Y. Raval, T. R. Tzeng, Y. Song, J. Wang, D. Li, X. Xuan, "Charge-based separation of particles and cells with similar sizes via the wall-induced electrical lift," *Electrophoresis*, vol. 38, no. 2, pp. 320-326, 2017. doi: 10.1002/elps.201600284

M. Trau, D. A. Saville, I. A. Aksay, "Field-induced layering of colloidal crystals," *Science*, vol. 272, no. 5262, pp. 706-709, 1996. doi: 10.1126/science.272.5262.706

H. N. Unni, H. J. Keh, C. Yang, "Analysis of electrokinetic transport of a spherical particle in a microchannel," *Electrophoresis*, vol. 28, pp. 658-664, 2006. doi: 10.1002/elps.200600576

P. Vasseur, R. G. Cox, "The lateral migration of a spherical particle in two-dimensional shear flows," *J. Fluid Mech*., vol. 78, no. 2, pp. 385-413, 1976. doi: 10.1017/S0022112076002498

O. D. Velev, K. H. Bhatt, "On-chip micromanipulation and assembly of colloidal particles by electric fields," *Soft Matter*, vol. 2, no. 9, pp. 738-750, 2006. doi: 10.1039/B605052B

E. J. W. Verwey, "Theory of the stability of lyophobic colloids," *J. Phys. Chem*., vol. 51, no. 3, pp. 631-636, 1947. doi: 10.1021/j150453a001

V. Vitagliano, P. A. Lyons, "Diffusion coefficients for aqueous solutions of sodium chloride and barium chloride," *J. Am. Chem. Soc*., vol. 78, no. 8, pp.1549-1552, 1956. doi: 10.1021/ja01589a011

VWR, *Safety Data Sheet*, accessed August 2021. https://us.vwr.com/assetsvc/asset/en_US/id/13485998/contents

P. Warszyński, X. Wu, T. G. M. van de Ven, "Electrokinetic lift force for a charged particle moving near a charged wall - a modified theory and experiment," *Colloids Surf. A*: *Physicochem. Eng. Asp.*, vol. 140, pp. 183-198, 1998. doi: 10.1016/S0927-7757(97)00277-X

P. Warszyński, T. G. M. van de Ven (2000), "Electroviscous forces on a charged cylinder moving near a charged wall," *J. Colloid Interface Sci.*, vol. 223, no.1, pp. 1-15, 2000. doi: 10.1006/jcis.1999.6605

P.S. Williams, M. H. Moon, J. C. Giddings, "Influence of accumulation wall and carrier solution composition on lift force in sedimentation/steric field-flow fractionation," *Colloids Surf. A*: *Physicochem. Eng. Asp.*, vol. 113, pp. 215-228, 1996. doi: 10.1016/0927-7757(96)03669-2

P. S. Williams, M. H. Moon, Y. Xu, J. C. Giddings, "Effect of viscosity on retention time and hydrodynamic lift forces in sedimentation/steric field-flow fractionation," *Chem. Eng. Sci.*, vol. 51, no. 19, pp. 4477-4488, 1996. doi: 10.1016/0009-2509(96)00291-6

A. Winkleman, B. D. Gates, L. S. McCarty, G. M. Whitesides, "Directed self-assembly of spherical particles on patterned electrodes by an applied electric field," *J. Adv. Mater.*, vol. 17, no. 12, pp. 1507-1511, 2005. doi: 10.1002/adma.200401958

E. Yariv, H. Brenner, "Near-contact electrophoretic motion of a sphere parallel to a planar wall," *J. Fluid Mech.*, vol. 484, pp. 85-111, 2003. doi: 10.1017/S002211200300418X

E. Yariv, "Force-free electrophoresis?," *Phys. Fluids*, vol. 18, no. 3, 031702 (4p), 2006. doi: 10.1063/1.2185690

E. Yariv, "Dielectrophoretic sphere–wall repulsion due to a uniform electric field," *Soft Matter*, vol. 12, no. 29, pp. 6277-6284, 2016. doi: 10.1039/C6SM00462H

A. Yee, M. Yoda, "Experimental observations of bands of suspended colloidal particles subject to shear flow and steady electric field," *Microfluid Nanofluidics*, vol. 22, 113 (12 p), 2018. doi: 10.1007/s10404-018-2136-3

A. Yee, H. Onuki, Y. Tagawa, M. Yoda, "Determining timescales for directed assembly of particles into bands by shear flow and electric fields," *Exp. Fluids*, vol.61, 133 (10 p), 2020. doi: 10.1007/s00348-020-02969-9

E. W. K. Young, D. Li, "Dielectrophoretic force on a sphere near a planar boundary," *Langmuir*, vol. 21, no. 25, pp. 12037-12046, 2005. doi: 10.1021/la0518546

L. Zeng, S. Balachandar, P. Fischer, “Wall-induced forces on a rigid sphere at finite Reynolds number,” *J. Fluid Mech*., vol 536, pp. 1-25, 2005. doi: 10.1017/S0022112005004738